

**Phase-Space Structure of the Dark
Matter Halo of Milky Way from Rotation
Curve Data and Implications for
Neutrino Signal from WIMP
Annihilation in Sun.**

By
SUSMITA KUNDU

Enrolment No. : PHYS05200704013

Saha Institute Of Nuclear Physics, Kolkata

*A thesis submitted to the
Board of Studies in Physical Sciences
In partial fulfillment of requirements
for the Degree of
DOCTOR OF PHILOSOPHY
of
HOMI BHABHA NATIONAL INSTITUTE*



August, 2014

STATEMENT BY AUTHOR

This dissertation has been submitted in partial fulfillment of requirements for an advanced degree at Homi Bhabha National Institute (HBNI) and is deposited in the Library to be made available to borrowers under rules of the HBNI.

Brief quotations from this dissertation are allowable without special permission, provided that accurate acknowledgement of source is made. Requests for permission for extended quotation from or reproduction of this manuscript in whole or in part may be granted by the Competent Authority of HBNI when in his or her judgment the proposed use of the material is in the interests of scholarship. In all other instances, however, permission must be obtained from the author.

SUSMITA KUNDU

DECLARATION

I, hereby declare that the investigation presented in the thesis has been carried out by me. The work is original and has not been submitted earlier as a whole or in part for a degree / diploma at this or any other Institution / University.

SUSMITA KUNDU

*To every single moment and memory breathed
with my loved ones*

ACKNOWLEDGEMENTS

The journey on this road could never have been completed without the help of many persons who deserve a sincere acknowledgment at the very beginning of my thesis.

I would like to take the opportunity to thank my advisor Prof. Pijushpani Bhattacharjee for his encouragement and proper guidance throughout my tenure. He has always motivated me and has given me the liberty to pursue my own way of thinking. I am grateful to him for his positive influence over my thinking that will be a valuable experience for the rest of my life.

Next, I would like to thank my colleague and dearest friend Soumini Chaudhury for her constant support in all aspects. We made a great team to work on academic front as well as to explore on various ventures together. The whole tenure of my Ph.D would not have been so enjoyable and memorable without those good moments we shared.

I offer my sincere thanks to the Director of our Institute for providing the necessary funding for the national and international travels. I would also like to thank the professors of my doctoral committee for going sincerely through my work reports and providing a proper evaluation of those. I also thank all the members of the Theory division and Astroparticle Physics and Cosmology division of Saha Institute of Nuclear Physics for providing me with a comfortable working environment.

My friends Susnata, Santanu, Abhishek with whom I have shared my office at various stages and enjoyed a very warm and enjoyable ambiance deserve my sincere thanks as well. I would like to thank my friend Lab for his all time help whenever I had a computer related trouble. I also thank all my batch mates and other fellow scholars whom I could not mention here.

I would like to take this opportunity to thank Prof. Rupak Mahapatra (Texas A &

M university, USA) for giving me an opportunity to work as summer internship with the prestigious CDMS collaboration. I also express my sincere gratitude to Prof. Subir Sarkar (Oxford University) and Prof. Subhabrata Majumdar (TIFR, India) for allowing me visits to have invaluable experiences on various fields. I would like to thank the coordinators of International Centre for Theoretical Physics, Trieste, Italy and Gran Sasso Underground facility in Italy for their invitations for workshops and laboratory visits.

Going back down the memory lane I would like express my gratitude to my teachers at SINP, University and College who have inspired me to pursue a research career. I would like to thank Prof. Amit Ghosh for giving me the opportunity to work on a project with him. I would like to thank Prof. Palash B. Pal for his lessons on latex. I would also like to thank Prof. Parthasarathi Majumdar, Prof. Debades Bandyopadhyaya, Prof. Debasish Majumdar, Prof. Probir Roy, Prof. Gautam Bhattacharya, Prof. Pratik Majumdar for various discussions with them on different occasions. I would also like to thank Prof. Parthasarathi Mitra, the Dean, HBNI at SINP for his help regarding the completion of this thesis.

Now it is time to thank those people in my life I am blessed with, who had always been there whenever I needed moral support. I would like to thank my parents in law who had the patience to support and encourage me throughout the tenure of my Ph.D.

I would like to express my special love to all my pet birds Ani, Bhutum and specially my pet nightingale Puku who had been a source of immense energy and who washed away all my negative thoughts with her chirping and innocence.

Finally the list of acknowledgment would be complete by expressing my heartfelt gratitude to the most important persons in my life who deserve all the credit. My father Mr. Subodh Kundu, my mother Mrs. Krishna Kundu and my husband

Sukanta. My parents have always been enthusiastic and encouraging about pursuing a career in academics. I could remain strong during the time of crisis as I knew that my parents were there to provide me with their care and inspiration. The words are not enough to thank them.

If there was anybody who had kept his entire belief and patience on my ability that would be my husband. It was a tough job for him playing various roles in my life. He had been my technical help, computer mechanic, mathematics teacher, cook, psychiatrist, caretaker, domestic help, financial help to mention a few only. This journey was never a lone one as he was there by my side all the eternity.

I am truly blessed with all these people in my personal and academic life and no thanks would be enough to express my gratitude towards them.

*“The layer that is above the sky and below the earth,
which is described as being situated between the earth and
the sky and which is indicated as the symbol of the past,
present and future, where is that situated?”*

.... Gargi (circa 800 BC)

LIST OF PUBLICATIONS

1. Neutrinos from Dark Matter annihilation in Sun : Implication of Self-consistent model of Milky Way Dark Halo.*

Susmita Kundu (SINP, India) , Pijushpani Bhattacharjee (SINP, India).

PHYSICAL REVIEW D **85** 123533 (2012); arXiv:1106.5711.

2. Deriving the velocity distribution of Galactic dark matter particles from the rotation curve data.*

Pijushpani Bhattacharjee (SINP, India and Washington University, USA) Soumini Chaudhury (SINP, India), Susmita Kundu (SINP, India) and Subhabrata Majumdar (TIFR, India).

PHYSICAL REVIEW D **87** 083525 (2013); arXiv:1210.2328.

3. Rotation Curve of the Milky Way out to ~ 200 kpc.[†]

Pijushpani Bhattacharjee (SINP, India and Washington University, USA), Soumini Chaudhury (SINP, India) and Susmita Kundu (SINP, India).

ApJ **785** (2014) 63; arXiv:1310.2659.

4. Local Dark Matter Density in the Light of Rotation Curve Data of Our Galaxy. [‡]

Pijushpani Bhattacharjee (SINP, India), Soumini Chaudhury (SINP, India) and Susmita Kundu (SINP, India).

Draft Under Preparation.

5. Velocity Anisotropy of Dark Matter Distribution of our Galaxy in the Context of Michie Model. *

Susmita Kundu (SINP, India) and Pijushpani Bhattacharjee (SINP, India).

Draft Under Preparation.

* : **Included in this thesis.**

† : **Partially included in this thesis.**

‡ : **Not included in this thesis.**

SYNOPSIS

A variety of astronomical observations indicate that more than 80% of the gravitating mass in the Universe exists in a form that emits no electromagnetic radiation of any kind. The presence of this “Dark Matter” (DM) is revealed only through its gravitational interaction with other matter on scales varying from dwarf galaxies up to the largest scale structures seen in the Universe today. On galactic scales the “flat” rotation curves of spiral galaxies including our Galaxy, the Milky Way, for example, out to galactocentric distances of several tens of kiloparsec can be naturally explained if the Visible Matter (VM) component of the Galaxy is embedded within a roughly spherical DM halo whose extent and the phase space structure are, however, not well quantified till date. The very nature and composition of this DM are presently unknown. Currently, the most promising candidates for the DM are the so-called Weakly Interacting Massive Particles (WIMPs) naturally arising in many theories beyond the Standard Model of particle physics such as those involving Supersymmetry and theories with large extra dimensions.

Several experiments world-wide are currently engaged in efforts to detect the DM particles by direct or indirect means [1]. Direct Detection (DD) experiments attempt to observe nuclear recoils due to scattering of WIMPs with nuclei in suitably chosen detector materials in underground laboratories. Such DD experiments for WIMP search have so far produced diverse results without any firm conclusion. A complementary approach to detect the WIMPs is via their annihilation products. Elastic or inelastic scattering of WIMPs with nuclei can lead to capture of the WIMPs by massive astrophysical bodies such as the Sun or the Earth, if, after scattering off a nucleus inside the body, the velocity of the WIMP becomes less than the escape velocity of the body. The WIMPs so captured over the lifetime of the capturing body would gradually settle down to the core where they would accumulate in sufficient amount to annihilate and produce standard model particles,

e.g., W^+W^- , Z^0Z^0 , $\tau^+\tau^-$, $t\bar{t}$, $b\bar{b}$, $c\bar{c}$, etc. Decays of these particles would then produce neutrinos, gamma rays, electron-positron, proton-antiproton pairs etc. For astrophysical objects like the Sun or the Earth, only the neutrinos would be able to escape from their interiors. Detection of these neutrinos by large neutrino detectors can provide a signature of WIMPs. In addition, γ -rays from WIMP annihilation in the Galactic centre or in dwarf spheroidal galaxies also may provide indication of Dark Matter, although no conclusive evidence has emerged from currently operating Indirect Detection (ID) experiments so far.

To analyze the results of both DD and ID experiments a proper understanding of the phase space structure of the DM halo is required. DM local density and the Velocity Distribution Function (VDF) of the DM particles constituting the DM halo of the Galaxy are two crucial inputs for determining the expected flux of the WIMPs and their expected event rates in a DD experiment. Similarly, the density and VDF of DM in the halo determine the capture rate of the WIMPs by an astrophysical body in the Galaxy. This thesis deals with some studies of phase space structure of the DM halo of the Milky Way and their implication for indirect detection of WIMPs through neutrino signal from WIMP annihilation in Sun. In doing this, I have used the observed Rotation Curve (RC) of our Galaxy as the primary observational input. I have discussed two approaches to the problem of studying the Phase Space Distribution Function (PSDF) of the Galactic DM halo. In one approach [2], a given density profile of the DM, the parameters of which are fixed by fit to the RC data, is inverted to obtain the isotropic PSDF by using the ‘‘Eddington’’ formalism [3]. In the second approach, I make a suitable ansatz for the PSDF of a finite DM halo allowing for possible anisotropic VDF of the DM particles and determine the parameters of the PSDF by fitting the resulting theoretically predicted RC to the observed RC data. I also present some new results on the derivation of the RC of the Galaxy to large Galactic distance. Finally the implications of using

a self-consistently determined PSDF for the case of neutrino signal from WIMP annihilation in Sun in terms of limits on WIMP parameter space are discussed.

In the following paragraphs I present a brief description and chapter wise outline of my proposed thesis.

In **Chapter I**, I present a broad overview of the subject of DM including a brief summary of the current experimental efforts towards both direct and indirect detection of the WIMP candidates of the DM. The importance of a proper study of the phase space structure of the DM halo of our Galaxy is highlighted. As already mentioned, the local DM density and VDF are two key astrophysical inputs for analysis of the DM detection experimental results. It is customary to use the so called “Standard Halo Model” (SHM) in analyzing the results from DM detection experiments. In this model the DM halo of the Galaxy is described by a single-component isothermal sphere with a Maxwellian VDF in the Galactic rest frame. The VDF is isotropic and is usually truncated at a chosen value of the escape speed of the Galaxy. The density of DM in the solar neighborhood is typically taken to be in the range 0.3 ± 0.1 GeV/cc . The velocity dispersion, the parameter characterizing the Maxwellian VDF of the SHM, is taken to be 270 km/sec. This follows from the relation between the velocity dispersion ($\langle v^2 \rangle^{1/2}$) of the particles constituting a single-component self-gravitating isothermal sphere and the asymptotic value of the circular rotation speed ($v_{c,\infty}$) of a test particle in the gravitational field of the isothermal sphere, namely, $\langle v^2 \rangle^{1/2} = \sqrt{3/2} v_{c,\infty}$ and assuming $v_{c,\infty} \approx v_{c,\odot} \approx 220$ km/sec where $v_{c,\odot}$ is the measured value of the circular velocity of the Galaxy in the solar neighborhood.

Though the SHM serves as a useful benchmark model, there are a number of reasons why the SHM does not provide a satisfactory description of the dynamics of the Galaxy. First, it does not take into account the modification of the phase space

structure of the DM halo due to the significant gravitational effect of the observed visible matter on the DM particles inside and up to the solar circle. Second, the isothermal sphere model of the halo is infinite in extent and has a density profile inversely proportional to the square of the Galactocentric distance, which yield a divergent total mass of the Galaxy thus making it unsuitable for representing a halo of finite size. Third, the procedure of truncating the Maxwellian speed distribution at a chosen value of the local (solar neighborhood) escape speed is not a self-consistent one because the resulting speed distribution is not, in general, a self-consistent solution of the steady-state Collisionless Boltzmann Equation (CBE) describing a finite system of collisionless DM particles. In addition to all these, various recent numerical simulations also find that the VDF of the DM particles deviates significantly from the usual Maxwellian form.

In order to obtain a more physically acceptable PSDF of the DM halo of the Galaxy I have taken two different approaches. In **Chapter II**, I describe the first methodology [2]. The VDF of the DM particles at any location in the Galaxy is self-consistently related to their spatial density as well as to the total gravitational potential, at that location. For a spherical system of collisionless particles (WIMPs, for example) with isotropic VDF satisfying the CBE, the Jeans theorem ensures that the PSDF depends on the phase space co-ordinates only through the total energy. For such a system, given a isotropic spatial density distribution one can get a unique PSDF by employing the ‘‘Eddington formula’’ [3]. It implies that, given a spherical density distribution, we can recover an ergodic distribution function that generates a model with the given density. Thus, given a isotropic density profile of a set of collisionless particles, we can calculate the VDF, provided the total gravitational potential in which the particles move is known. The demand of positivity of the PSDF itself with positive energy implies that at any location r , the VDF has a natural truncation at a maximum value of velocity. I have modeled both the DM

and VM density distributions and by solving Poisson’s equation the total gravitational potential of the system is obtained. The VM is modeled as spherical bulge and double exponential disk and the DM density profile as the universal Navarro-Frenk-White (NFW) form. The density models used here have a total of seven free parameters, namely the scale densities and scale radii. The most-likely (ML) values and the 68% C.L. upper and lower ranges of these parameters are determined by performing a Markov Chain Monte Carlo (MCMC) analysis, which is well suited for multi-parameter determination, using the observed RC data of the Galaxy. Here I have used the RC data compiled by Sofue et.al. [4] which extends upto a large distance and is standardised at the following set of values of Galactic Constants (GC) $[R_{\odot}, V_{c,\odot}] = [8.0 \text{ kpc}, 200 \text{ km/sec}]$, with R_{\odot} and $V_{c,\odot}$ being the distance and rotation speed of Sun from Galactic centre.

Once the model parameters are fixed by the MCMC analysis using above mentioned RC data the value of the local DM density as well as the entire DM density profile in the Galaxy are determined. With the parameters of the DM density profile thus fixed, I then use the “Eddington” formalism to obtain the PSDF as a function of total energy of the system. Once the PSDF is obtained the VDF at solar location with its uncertainty band corresponding to the uncertainties in the RC data is also derived. The resulting VDF at all location in the Galaxy is found to be significantly non-Maxwellian in nature as suggested by recent numerical simulations also. A normalised non -Maxwellian parametrised fit to this VDF is also provided which can be readily used for the calculation of expected event rates for both DD and ID experiments [2].

It is clear that the RC of the Galaxy is a crucial astrophysical input in deriving the PSDF of the DM in the Galaxy. On the other hand, the RC is not a directly measured object, rather, it is constructed from kinematical data on tracer objects moving in the total gravitational potential of the Galaxy. Apart from various other

uncertainties, the RC is sensitive to the Galactic constants (GCs), namely, the distance and rotation speed of Sun from the Galactic centre, whose current measurements are uncertain. Thus the PSDF derived using the RC data is sensitive to the uncertainties in the RC data including that due to the choice of the GCs. In **Chapter III**, I describe the details of constructing a RC data set from direct observational data on different samples of tracers without referring to any specific mass model of the DM halo or the VM bulge or disk of the Galaxy. I have specifically worked on extending the RC data beyond the Galactic disk region [5]. In doing this one has to rely on distant tracers like Blue Horizontal Branch (BHB) stars, K Giant (KG) stars and relatively rare tracer objects like Globular Clusters (GCl), dwarf spheroidal (dSph) galaxies and so forth which populate the Milky Way’s extended DM halo out to Galactocentric distances of several hundreds of kpc. Unlike the disk tracers, these non-disk tracers do not exhibit any systematic motion, and move about in the Galaxy along various random orbits. Following the standard approach, I assume that the tracer population under consideration is isotropically distributed in the halo of the Galaxy and use the Jeans equation [6] for spherical systems relating the circular velocity at a given radius to the number density and radial as well as transverse velocity dispersions of the tracers at that radius. Of course, in absence of full 3-D velocity information and with only the observed radial velocity dispersion available, the RC constructed using Jeans equation depends on the unknown velocity anisotropy (β) parameter of the non-disk tracers. Since currently not much reliable observational information on tracer β is available, I have calculated the circular velocities using Jeans equation for three separate cases with (a) β taken as a constant free parameter with values in the range from ‘0’ (corresponding to complete isotropy of the tracers’ orbits) to ‘1’ (corresponding to completely radial orbits of the tracers), (b) a radially varying β of the Osipkov-Merritt (OM) form [3] and (c) a radial profile of β obtained from a recent large high resolution hydrodynamical simulations of formation of late-type spirals like our Galaxy [7].

It is observed that while the RC in the disk region is significantly influenced by the choice of the GCs, the dominant uncertainty in the RC at large distances beyond the stellar disk comes from the uncertainty in the value of anisotropy parameter (β). It is also noticed that irrespective of the value of β , the mean RC steadily declines with radius beyond ~ 60 kpc. The circular speed at a given radius decreases as tracer anisotropy parameter is increased (i.e., as the tracers' orbits are made more radially biased). Thus, the lowest value of the rotation speed at any radius is attained for the case of complete radial anisotropy ($\beta=1$) of the non-disk tracers. This fact allows us to set a lower limit on the total mass of the Galaxy within a radius r , giving $M(r = 200 \text{ kpc}) \leq (6.8 \pm 4.1) \times 10^{11} M_{\odot}$ [5].

In **Chapter IV** I discuss and illustrate the second approach to obtain the PSDF of the DM particles and hence their local DM density and VDF. In this approach I start with an ansatz for the PSDF which is a solution of CBE that describes a finite sized dark halo of the Galaxy. In particular, I have adopted the ‘‘Michie’’ model of the PSDF of a finite system of collisionless particles having anisotropic VDF [3]. In this model the PSDF depends on both the total energy and total angular momentum of the system. There are three important features of this model: First, at every location within the system, a DM particle can have speeds up to a maximum speed which is self-consistently determined by the model itself. A particle of maximum velocity at any location within the system can just reach its outer boundary, fixed by the truncation radius, a parameter of the model, where the DM density by construction vanishes. Second, the speed distribution of the particles constituting the system is non-Maxwellian. Finally, the model has an additional parameter called the anisotropy radius (r_a) which sets the length scale for the radial profile of the velocity anisotropy of the particles in the system. To include the gravitational effect of the observed visible matter on the DM particles, we modify the ‘‘pure’’ Michie model PSDF by replacing the gravitational potential appearing

in the Michie model PSDF by the total gravitational potential consisting of the sum of the potentials due to DM and the observed VM. This interaction with the VM changes the density profile, velocity dispersion profile and the VDF of the DM particles compared to those for a “pure” Michie model. Furthermore, the core radius of the DM halo gets shortened and the core density becomes higher and the DM density in disk region is enhanced as compared to the vertical direction. In order to find the DM model parameters I have used the RC data [5] as mentioned above extending upto large Galactocentric distance ~ 200 kpc and scaled to GC : $[R_{\odot}, V_{c,\odot}] = [8.3 \text{ kpc}, 244 \text{ km/sec}]$. I have studied the dependence of the local DM density on the set of values of the GC used in obtaining the RC data. In general I have found that higher value of $V_{c,\odot}$ supports higher local DM density. The total VDF at all locations in the Galaxy is also found to be non-Maxwellian.

In **Chapter V** and **Chapter VI** I discuss the expected neutrino signal from WIMP annihilation in the Sun within the context of a self-consistent PSDF, the parameters of which are determined by fit to RC data. Specifically, In **Chapter V** the calculations of the expected capture rate of WIMPs within Sun is described [8]. The capture rate depends on the local DM density as well as the VDF of the WIMPs in the solar neighborhood as the Sun goes around the Galaxy. I present the results of my calculation of the WIMP capture rate in the Sun which is done within the context of the “King” model [9] which is the isotropic version (obtained in the limit $r_a \rightarrow \infty$) of the “Michie” model discussed in Chapter IV above.

Then in **Chapter VI** the calculations of the neutrino fluxes originating from DM annihilation into different channels and decay of those annihilation products are described [8]. These neutrinos can travel to Earth and can be detected by different neutrino telescopes. I have derived the 90% C.L. upper limits on the WIMP-proton Spin-Independent (SI) and Spin-Dependent (SD) elastic scattering cross sections as a function of the WIMP mass for various WIMP annihilation channels using the

Super-Kamiokande search results [10, 11] for possible neutrino signal from WIMP annihilation in the Sun and examined the consistency of those limits with the 90% C.L. compatible regions on the WIMP parameter space given by the DAMA experiment [9, 12]. It is found that the requirement of consistency of the Super-Kamiokande [10] implied upper limits on the WIMP-proton elastic cross section as a function of WIMP mass with the results of DAMA, imposes stringent restrictions on the branching fractions of the various WIMP annihilation channels. In the case of SI WIMP-proton interaction, the Super-Kamiokande upper limits do not place additional restrictions on the DAMA compatible region of the WIMP parameter space if the WIMPs annihilate dominantly to $b\bar{b}$ and $c\bar{c}$. On the other hand, if direct annihilation to $\tau^+\tau^-$ and $\nu\bar{\nu}$ -s occurs, then the branching fractions to these channels are restricted to below (35–45)% and (0.4–0.8)% respectively. In the case of SD interactions, the restrictions on the branching fractions of various annihilation channels are much more stringent, essentially ruling out the DAMA-compatible region of the WIMP parameter space if the relatively low-mass WIMPs under consideration (2 GeV – 20 GeV) annihilate predominantly to any mixture of $b\bar{b}$, $c\bar{c}$, $\tau^+\tau^-$ and $\nu\bar{\nu}$ final states [8]. The very latest results from the Super-Kamiokande Collaboration [11] put the above conclusions on an even firmer footing by making the above constraints on the branching fractions of various WIMP annihilation channels more stringent by roughly a factor of 3 – 4.

Finally, in **Chapter VII**, I summarize the new results presented in this thesis and conclude by indicating the unresolved issues and possible future research in this context.

Bibliography

- [1] Bertone, G. (Ed.), Particle Dark Matter: Observations, Models and Searches, (Cambridge University Press, U. K., 2010).
- [2] Bhattacharjee, P., Chaudhury, S., Kundu, S., & Majumdar, S., Phys. Rev. **D 87** (2013) 083525.
- [3] Binney, J. & Tremaine, S., Galactic Dynamics, 2nd Edition, (Princeton University Press, Princeton, 2008).
- [4] Y. Sofue, PASJ **64** (2012) 75; [arXiv:1110.4431].
- [5] Bhattacharjee, P., Chaudhury, S. & Kundu, S., ApJ **785** (2014) 63; [arXiv:1310.2659v3].
- [6] Binney, J., & Merrifield, M., Galactic Astronomy, (Princeton University Press, Princeton, 1998).
- [7] Rashkov, V., Pillepich, A., Deason, A. J., et al., ApJL **773** (2013) L32.
- [8] Kundu, S. & Bhattacharjee, P., Phys. Rev. **D 85** (2012) 123533.
- [9] Chaudhury, S., Bhattacharjee, P., & Cowsik, R., JCAP **09** (2010) 020.
- [10] Super-Kamiokande collaboration: S. Desai et al, Phys. Rev. **D 70** (2004) 083523.
- [11] Super-Kamiokande collaboration: T. Tanaka et al, Astrophys. J. **742** (2011) 78; [arXiv:1108.3384].

- [12] DAMA/LIBRA collaboration: R. Bernabei et al., Eur. Phys. J. **C 56** (2008) 333; [arXiv:0804.2741], *ibid* **C 67** (2010) 39; [arXiv:1002.1028].

List of Figures

2.1	The 2D posterior probability density function for Dark Matter parameters ($r_s - \rho_{\text{DM},\odot}$), marginalized over the visible matter parameters.	28
2.2	Rotation curve of the Galaxy with the most-likely set of values of the Galactic model parameters listed in Table 2.1. The data with error bars are from Ref. [161].	28
2.3	The local VDF for the approximated Visible Matter potential $\Phi_{\text{VM}}(r)$ and the local VDFs for the VM potentials in $z=0$ $\Phi_{\text{VM}}(r, \theta = \pi/2)$ plane and along z -axis $\Phi_{\text{VM}}(r, \theta = 0)$ respectively are presented. The plot shows that the local VDF for the approximated Visible matter potential is kind of an average between the local VDFs obtained with $\Phi_{\text{VM}}(r, \theta = \pi/2)$ and $\Phi_{\text{VM}}(r, \theta = 0)$.	30
2.4	Normalized local speed distribution, $f_{\odot}(v)$, corresponding to the most-likely (ML) set of values of the Galactic model parameters given in Table 2.1 (black curve) and its uncertainty band (cyan band) corresponding to the 68% C.L. upper and lower ranges of the Galactic model parameters. The best parametrized non-Maxwellian (orange curve) fit (equation 2.10 — almost indistinguishable from the ML curve) as well as the closest Maxwellian fit (pink curve), the latter with the form $f_{\odot}^{\text{Maxwell}}(v) \propto v^2 \exp(-v^2/v_0^2)$ truncated at $v_{\text{max},\odot} = 516 \text{ km s}^{-1}$ (see Table 2.2) and with the free parameter v_0 determined to be 206 km s^{-1} , are also shown.	32

- 2.5 Same as Figure 2.4 along with comparison with results obtained from various numerical simulations [168]. 33
- 2.6 Normalized speed distribution of the DM particles at various Galactocentric radii (solid curves), corresponding to the most-likely set of values of the Galactic model parameters given in Table 2.1. The curves (dotted) for the corresponding best Maxwellian fit are also shown for comparison. The inset shows the pseudo-phase space density of DM, $Q \equiv \rho/\langle v^2 \rangle^{3/2}$, as a function of r 34
- 3.1 Schematic diagram showing the coordinate system, velocity and distance notations used in this chapter. 41
- 3.2 x - z , y - z and x - y scatter plots (after removing objects with $r < 25$ kpc; see text) for the three samples of non-disk tracer objects considered in this chapter, namely, (1) the “BHB” sample, a set of 1457 blue horizontal branch stars from the compilation of [183], (2) the “KG” sample, a set of 2227 K-Giant stars from the compilation of [184], and (3) the “Hg” sample, a heterogeneous set of 65 objects comprising of 16 Globular Clusters (GC) from [185], 28 field blue horizontal branch (FHB) stars from [187], and 21 dwarf spheroidals (dSph) from [189], for $R_0 = 8.3$ kpc with the sun located at $(x = 0, y = R_0, z = 0)$ 44
- 3.3 The tracer number density, n_{tr} , for the three non-disk tracer samples considered in this chapter (see text and Figure 3.2 for details and source references for the samples). The top left panel shows, for comparison, the tracer densities obtained in some earlier studies [179, 175, 180] which used different tracer samples. The other three panels show the best power law fits to the radial profiles of n_{tr} for the three non-disk samples. The GC set used is $\left[\frac{R_0}{\text{kpc}}, \frac{V_0}{\text{km s}^{-1}} \right] = [8.3, 244]$ 45

3.4 The GSR frame los velocity dispersion of the tracers, σ_{GSR} , for the three non-disk tracer samples considered in this chapter (see text and Figure 3.2 for details and source references for the samples). The top left panel also shows, for comparison, the σ_{GSR} obtained in some earlier studies [179, 180, 181] which used different tracer samples. The other three panels show the best power-law fits to the radial profiles of σ_{GSR} for the three non-disk samples. The GC set used is $\left[\frac{R_0}{\text{kpc}}, \frac{V_0}{\text{km s}^{-1}} \right] = [8.3, 244]$ 47

3.5 Circular velocities with their 1σ error bars for the three different non-disk tracer samples used here in Figure 3.2. The left panels are for tracer velocity anisotropy $\beta = 0$ and three different sets of values of the Galactic constants, $\left[\frac{R_0}{\text{kpc}}, \frac{V_0}{\text{km s}^{-1}} \right]$, as indicated, whereas the right panels show the results for three different constant (r -independent) values of $\beta = 0, 0.5$ and 1 , with $\left[\frac{R_0}{\text{kpc}}, \frac{V_0}{\text{km s}^{-1}} \right] = [8.3, 244]$ 51

3.6 Left: Rotation curve of the Galaxy for three different sets of values of the Galactic constants $\left[\frac{R_0}{\text{kpc}}, \frac{V_0}{\text{km s}^{-1}} \right]$ as indicated and non-disk tracers' velocity anisotropy parameter $\beta = 0$. The data points and their 1σ error bars shown here are obtained by weighted averaging over the combined v_c data obtained from different disk and non-disk tracer samples. Right: Rotation curve of the Galaxy for $\left[\frac{R_0}{\text{kpc}}, \frac{V_0}{\text{km s}^{-1}} \right] = [8.0, 200]$ and non-disk tracers' velocity anisotropy parameter $\beta = 0$ compared with that obtained by [140] (S12). 52

- 3.7 Rotation Curve for $\left[\frac{R_0}{\text{kpc}}, \frac{V_0}{\text{km s}^{-1}}\right] = [8.3, 244]$ and various values of β . The shaded bands marked D12a and G10 in the left and right panels, respectively, represent the RCs and their uncertainty bands obtained earlier by [177] (D12a) (up to $r \sim 50$ kpc) and [176] (G10) (up to $r \sim 80$ kpc), respectively. In addition, estimates of circular velocities at certain specific values of r obtained from various independent considerations by [178] (K12), [195] (M11), [196] (MB10), [197] (VERA), [173] (S09), [198] (WE99), [175] (X08), [199] (S11), [200] (W10), and [181] (D12b) are shown for comparison. 53
- 3.8 The mass, $M(r) = rv_c^2(r)/G$, within r , as a function of r , obtained from the RCs shown in Figure 3.7 for $\left[\frac{R_0}{\text{kpc}}, \frac{V_0}{\text{km s}^{-1}}\right] = [8.3, 244]$ and various values of the tracers' velocity anisotropy parameter β . Estimates of $M(r)$ at certain specific values of r obtained from various independent considerations in some earlier works, namely, [178] (K12), [198] (WE99), [177] (D12a), [175] (X08), [195] (M11), [176] (G10), [199] (S11), [201] (CU10), [202] (DB98), [179] (B05-06), [181] (D12b), and [135] (BCKM 2013), are shown for comparison. 54
- 3.9 Rotation curve of the Milky Way to ~ 200 kpc for $\left[\frac{R_0}{\text{kpc}}, \frac{V_0}{\text{km s}^{-1}}\right] = [8.3, 244]$ and for a radial profile of the non-disk tracers' velocity anisotropy parameter β of the Osipkov-Merritt (OM) form, $\beta(r) = (1 + r_a^2/r^2)^{-1}$, with two values of the "anisotropy radius" $r_a = 15$ kpc (OM-15) and 70 kpc (OM-70). The RC data generated with a radial profile of β derived from Figure 2 of [182] (R13) (data points marked $\beta(r)$:R13) are also shown for comparison. The inset shows the OM β profile for various values of r_a together with the β profile from Figure 2 of R13. 55

3.10 Rotation curve of the Milky Way to ~ 200 kpc for $\left[\frac{R_0}{\text{kpc}}, \frac{V_0}{\text{km s}^{-1}} \right] =$
 $[8.3, 244]$ and for β derived from Figure 2 of [182] (R13) in log scale
and compared with the circular velocity data from terminal veloci-
ties (NS13-Fig8) and rotation curve fits for Burkert (NS13-Burkert)
and NFW (NS13-NFW) models from [141]. The numerical data for
 $\beta(r)$:R13 are given in Table 3.2. 57

4.1 Fit to the rotation curve data standardized at two sets of GCs $\left[\frac{R_0}{\text{kpc}}, \frac{V_0}{\text{km s}^{-1}} \right]$
: $[8.3, 244]$ and $[8.5, 220]$ left and right panel respectively. Plots are
also demonstrated for three values of Σ_{VM} from top panel to bottom
panel, $(39, 48, 57) M_{\odot} \text{pc}^{-2}$ respectively. 71

4.2 Density profile for best-fit model parameter values. The plots shown
are for the $\Sigma_{\text{VM}} = 48 M_{\odot} \text{pc}^{-2}$ value and for the two RC data profiles
standardized at two sets of GCs $\left[\frac{R_0}{\text{kpc}}, \frac{V_0}{\text{km s}^{-1}} \right]$: $[8.3, 244]$ and $[8.5, 220]$
in left and right panel respectively. The plots further demonstrate the
effect of inclusion of VM in a self consistent manner. The core density
is increased and the core radius is shortened. The DM density around
the disk is also significantly enhanced. 75

4.3 The mass profiles are shown for the $\Sigma_{\text{VM}} = 48 M_{\odot} \text{pc}^{-2}$ value and for
the two RC data profiles standardized at two sets of GCs $\left[\frac{R_0}{\text{kpc}}, \frac{V_0}{\text{km s}^{-1}} \right]$
: $[8.3, 244]$ and $[8.5, 220]$ in left and right panel respectively. 75

4.4 The Maximum velocity v_{max} profiles are shown for the $\Sigma_{\text{VM}} = 48 M_{\odot} \text{pc}^{-2}$
value and for the two RC data profiles standardised at two sets of GCs
 $\left[\frac{R_0}{\text{kpc}}, \frac{V_0}{\text{km s}^{-1}} \right]$: $[8.3, 244]$ and $[8.5, 220]$ in left and right panel respec-
tively. 76

4.5 The velocity dispersion profiles (radial, tangential and total) are shown
for the $\Sigma_{\text{VM}} = 48 M_{\odot} \text{pc}^{-2}$ value and for the two RC data profiles stan-
dardized at two sets of GCs $\left[\frac{R_0}{\text{kpc}}, \frac{V_0}{\text{km s}^{-1}} \right]$: $[8.3, 244]$ and $[8.5, 220]$ in
left and right panel respectively. 76

- 4.6 The local velocity distribution functions (radial, tangential and total) are shown for the $\Sigma_{\text{VM}} = 48M_{\odot}\text{pc}^{-2}$ value and for the two RC data profiles standardized at two sets of GCs $\left[\frac{R_0}{\text{kpc}}, \frac{V_0}{\text{km s}^{-1}}\right]$: [8.3, 244] and [8.5, 220] in left and right panel respectively. 77
- 4.7 The velocity distribution functions (radial, tangential and total) at various Galactic radii are shown for the $\Sigma_{\text{VM}} = 48M_{\odot}\text{pc}^{-2}$ value and for the two RC data profiles standardized at two sets of GCs $\left[\frac{R_0}{\text{kpc}}, \frac{V_0}{\text{km s}^{-1}}\right]$: [8.3, 244] and [8.5, 220] in left and right panel respectively. 78
- 4.8 The anisotropy parameter profile for the $\Sigma_{\text{VM}} = 48M_{\odot}\text{pc}^{-2}$ value and for the two RC data profiles standardized at two sets of GCs $\left[\frac{R_0}{\text{kpc}}, \frac{V_0}{\text{km s}^{-1}}\right]$: [8.3, 244] and [8.5, 220] in left and right panel respectively. 79
- 4.9 Effect of different Σ_{VM} on Mass profiles (top panel) and local velocity profiles (bottom panel) for the two RC data profiles standardized at two sets of GCs $\left[\frac{R_0}{\text{kpc}}, \frac{V_0}{\text{km s}^{-1}}\right]$: [8.3, 244] and [8.5, 220] in left and right panel respectively. 80
- 5.1 Left: Rotation curve data and fit for three models, namely M1, M2, M3, as described in Table 5.1. Right: Rotation curve fit for the model M1 only. Contributions from visible and dark matter are shown separately here. 96
- 5.2 Left: Density distribution for the visible matter and the dark matter (model M1 only). The plots are given for both couple and uncoupled case as discussed in the text. In the coupled case it is evident that the core density is increased and the core radius is shortened. There is enhancement in the disk region as well. Right: Mass distribution for the M1 model separately shown for visible and dark matter. . . . 96

- 5.3 Left: Maximum velocity v_{\max} distribution for all the three models, namely M1, M2 and M3. Right: Velocity distributions at solar location for the three models along with the Maxwellian distribution of SHM. The plot shows that the distributions arising from the King model are sharply truncated at higher velocity end whereas the Maxwellian distribution has a long high velocity tail. 97
- 5.4 The capture rate as a function of the WIMP mass for the three halo models specified in Table 5.1, and for spin-independent (SI: left panel) and spin-dependent (SD: right panel) WIMP- proton interactions. All the curves are for a reference value of the WIMP-proton elastic SI or SD cross section of 10^{-4} pb. 98
- 6.1 Neutrino spectra for a few representative WIMP masses for $\tau^+\tau^-$ annihilation channel. 105
- 6.2 Neutrino spectra for a few representative WIMP masses for $\bar{b}b$ annihilation channel. 107
- 6.3 Neutrino spectra for a few representative WIMP masses for $\bar{c}c$ annihilation channel. 108
- 6.4 Neutrino spectra for a few representative WIMP masses for $\nu\bar{\nu}$ annihilation channel. 109
- 6.5 The upward going muon event rates in the Super-Kamiokande detector due to neutrinos from WIMP annihilation in the Sun as a function of the WIMP mass for the four annihilation channels as indicated, assuming 100% branching ratios for each channel by itself, and for spin-independent (SI: left panel) and spin-dependent (SD: right panel) WIMP-proton interactions. The three curves for each annihilation channel correspond, as indicated, to the three halo models specified in Table 5.1 in Chapter V. All the curves are for a reference value of the WIMP-proton elastic SI or SD cross section of 10^{-4} pb. 111

- 6.6 The 90% C.L. upper limits on the WIMP-proton spin-independent (SI: left panel) and spin-dependent (SD: right panel) elastic cross section as a function of WIMP mass derived from the Super-Kamiokande measurements of the up-going muon events from the direction of the Sun [147, 148], for the three relevant event types, namely, Fully Contained (FC), Stopping (S) and Through Going (TG), as discussed in the text. The thick portions of the curves serve to demarcate the approximate m_χ ranges where the different event types make dominant contributions to the upper limits. The curves shown are for the four annihilation channels, assuming 100% branching ratio for each channel by itself. The 90% C.L. allowed regions in the WIMP mass vs. WIMP-proton elastic cross section plane implied by the DAMA/LIBRA experiment’s claimed annual modulation signal [280] as well as the 90% C.L. upper limits on the cross section as a function of the WIMP mass implied by the null results from the CRESST-1 [281], CDMS-II-Si [282], CDMS-II-Ge [283] and XENON10 [284] experiments (solid curves) are also shown. All the curves shown are for our halo model M1 ($\rho_{\text{DM},\odot} = 0.2 \text{ GeV}/\text{cm}^3$) specified in Table 5.1 in Chapter V. 113
- 6.7 Same as Fig. 6.6, but for the halo model M2 ($\rho_{\text{DM},\odot} = 0.3 \text{ GeV}/\text{cm}^3$) specified in Table 5.1 in Chapter V. 113
- 6.8 Same as Fig. 6.6, but for the halo model M3 ($\rho_{\text{DM},\odot} = 0.4 \text{ GeV}/\text{cm}^3$) specified in Table 5.1 in Chapter V. 114
- 6.9 Same as Fig. 6.6, but using the new S-K data from Ref. [285] and considering their “Stopping” upmu events only. 118

List of Tables

2.1	The most-likely values of the Galactic model parameters, as well as their 68% C.L. lower and upper ranges, means and standard deviations (SD), obtained from our MCMC analysis using the observed rotation curve data.	27
2.2	The most-likely values of various relevant physical parameters of the Milky Way and their upper and lower ranges derived from the most-likely- and 68% C.L. upper and lower ranges of values of the Galactic model parameters listed in Table 2.1.	29
3.1	Best-fit parameter values for power-law fits to the radial profiles of the number density, n_{tr} , and the Galactic Standard of Rest (GSR) frame <i>los</i> velocity dispersion, σ_{GSR} , of the tracers for the three non-disk tracer samples considered in this chapter (see text and Figure 3.2 for details and source references for the samples). The parameter values are given for three different sets of values of the GCs, $\left[\frac{R_0}{\text{kpc}}, \frac{V_0}{\text{km s}^{-1}} \right]$	50
3.2	The circular velocity, V_c , and its 1- σ error, Δv_c , for various values of the Galactocentric distance, r , for a radial profile of the non-disk tracers' velocity anisotropy parameter β derived from Figure 2 of [182], with $\left[\frac{R_0}{\text{kpc}}, \frac{V_0}{\text{km s}^{-1}} \right] = [8.3, 244]$	56

4.1	Best Fit Michie model (DM) parameters for two different sets of Galactic Constants (GCs) : $\left[\frac{R_0}{\text{kpc}}, \frac{V_0}{\text{km s}^{-1}} \right]$, namely [8.3,244] and [8.5,220] (I.A.U. standard) with the visible matter model and the parameter values as described in previous section. The visible matter disk surface density at solar location is fixed at three values ($\Sigma_{\text{VM}} = 48 \pm 9 M_{\odot} \text{pc}^{-2}$) covering the range as allowed by observations [237].	70
4.2	Physically relevant derived quantities calculated for Michie model for three different Σ_{VM} values and for two sets of GCs.	72
5.1	Parameters of our self-consistent model of the Milky Way’s Dark Matter halo that give good fits to the Galaxy’s rotation curve data, for the three chosen values of the DM density at the solar neighborhood.	95
6.1	Upper limits — derived from Figures 6.6, 6.7 and 6.8 — on the branching fractions for the four annihilation channels, from the requirement of consistency of the S-K implied upper limits on the WIMP-proton elastic cross sections with the “DAMA-compatible” region of the WIMP mass versus cross section parameter space (within which the annual modulation signal observed by the DAMA/LIBRA experiment [280] is compatible with the null results of other DD experiments determined within the context of our halo model [155]), for both spin-independent (SI) and spin-dependent (SD) interactions and the three halo models specified in Table 5.1 in Chapter V. The limits are calculated using the three different upward-going muon event types, namely, Fully Contained (FC), Stopping (S) and Through Going (TG). The three consecutive numbers for each annihilation channel and muon event type refer to the three different halo models M1, M2, M3, as indicated.	114

6.2 Upper limits on the branching fractions of the four annihilation channels, derived from the requirement of consistency of the new S-K-
implied upper limits on the WIMP-proton elastic cross sections shown
in Figure 6.9 with the “DAMA-compatible” regions, for both spin-
independent (SI) and spin-dependent (SD) interactions 118

Contents

Synopsis	xvii
List of Figures	xxxvi
List of Tables	xxxix
1 Introduction	3
2 Dynamics of Dark Matter in our Galaxy	19
2.1 Introduction	19
2.2 Standard Halo Model (SHM) :	22
2.3 Eddington Formalism	24
2.4 Results	26
2.5 Summary	34
3 Rotation Curve of Milky Way out to 200 kpc	37
3.1 Introduction	37
3.2 The Jeans equation approach	39
3.3 Non-Disk tracer samples	42
3.4 Rotation Curves	49
3.5 Summary	57
4 Michie Model	61
4.1 Introduction	61

<i>CONTENTS</i>	1
4.2 Visible Matter Model	64
4.3 Michie Model	64
4.4 Results	68
4.5 Summary	74
5 Indirect Detection of WIMPs	81
5.1 Introduction	81
5.2 Calculation of Capture Rate	84
5.3 Calculation of Annihilation Rate	88
5.4 The self-consistent King Model	90
5.5 Results Using King Model	94
5.6 Summary	97
6 Neutrino flux and exclusion plots	101
6.1 Introduction	101
6.2 Neutrino flux	102
6.2.1 tau decay	104
6.2.2 b decay	106
6.2.3 c decay	107
6.2.4 prompt nu	108
6.3 Event rates at S-K	109
6.4 Exclusion Plots	112
6.5 Exclusion Plots from another larger dataset	116
6.6 Summary	119
7 Summary, Conclusion and Outlook	121
References	147

Chapter 1

Introduction

Most of the Universe, in form of matter or energy, that we can perceive with the naked eyes or through immensely sophisticated present day instruments constitutes only a tiny fraction, specifically 4.9% [1]. The rest is “Dark”, of which 26.8% is in form of some strange matter that does not have any electromagnetic and strong interactions thus making it experimentally opaque or “Dark”. The remaining 68.3% undetected Universe is the so called “Dark Energy” (DE) which is an unknown form of energy that seems to be the source of a repulsive force causing the expansion of the universe to accelerate. This thesis deals with the dynamics of “Dark Matter” (DM) in our Galaxy and its detection via indirect means.

There are large numbers of astronomical observations that indicate strongly about the presence of Dark Matter via their gravitational interactions on scales varying from dwarf galaxies up to the largest scale structures seen in the Universe today. However, the particle nature of the dark matter is yet to be unraveled by various experiments presently going on worldwide. The experimental discovery of Dark Matter is one of the major still unsolved problems of contemporary cosmology, astrophysics and particle physics. For reviews, see, e.g., Refs. [2, 3, 4, 5, 6].

The existence of dark matter is well established via various phenomena mediated through gravitational interaction of these particles. The evidence for dark matter dates back to as early as almost a century sans one or two decades in the works of many physicists and astronomers like J. H. Oort [7], F. Zwicky [8, 9], H. W. Babcock [10], V. C. Rubin [11, 12] to mention only a few. These works mainly involve the observation on galaxies and clusters and speculation of the “missing mass” or “Dark Matter” as inferred from the rotation curve profiles and velocity dispersion calculations. Till present date the rotation curves of various galaxies are the most concrete proof of the existence of DM.

There are many more evidences for these DM particles, for example, gravitational lensing [13, 14]. Because of the gravitational field of the massive galaxy cluster the space time gets curved and hence the light traveling from a distant source from behind the cluster bends its path near the cluster on the way to the telescopes [15] and this results in multiple images and images are distorted into arcs. For instance, HST observations of Abell 2218 show arcs and multiple images [16]. Then there are measurements of the cosmic microwave background (CMB) radiation and large-scale structure (LSS) of the Universe which provide perhaps the most compelling evidence that the dark matter is non-baryonic and the most precise measurements of the abundance of dark matter. Angular fluctuations in the CMB spectrum provide evidence for dark matter. There are further evidences of Dark Matter coming from observations of Large Scale Structure formations. Structure formation occurred hierarchically and the model of structure formation needs inclusion of dark matter or rather specifically cold dark matter (i.e. dark matter particles moving at non-relativistic speed) to succeed. Then there are many more evidences of the presence and/or requirement of dark matter in various phenomena like Sky surveys, baryon acoustic oscillations, Type Ia supernovae distance measurements, Lyman-alpha forest etc.

One special evidence that requires particular attention is the phenomenon of Bullet Cluster because so far other Dark Matter less theories like Modified Newtonian Gravity or MOND [17] have not been very successful in explaining this one amongst other evidences of dark matter. It is a system of two colliding clusters. During the collision the baryonic part interacts via electromagnetic interaction and hence slows down whereas the dark matter part pass through without suffering any lag. Therefore when observed through X-ray emission and gravitational lensing both the separation of the dark and the baryonic part becomes evident.

The absence of electromagnetic and strong interactions makes it experimentally “dark”, however, interactions at the weak scale might be possible. Many theories beyond the standard model predict particles which are neutral, cold (i.e. non-relativistic), and stable (or have half-lives longer than the age of the Universe) and serves the purpose. There are a lot of postulations about new particles that could be potential candidate for dark matter, arising in theories beyond the Standard Model of particle physics. Multiple lines of evidence from cosmic microwave background probes, measurements of cluster and galaxy rotations, strong and weak lensing and big bang nucleosynthesis all point toward a model containing cold dark matter particles as the best explanation for the universe we see.

Initially some astronomical massive bodies formed of baryons which emit no or very small amount of radiation for example black holes, faint old white dwarfs, brown dwarfs, neutron stars, stellar remnants etc. were thought to constitute the Dark Matter. These were named to be Massive Compact Halo Objects (MACHOs). Various astronomical surveys such as EROS, MACHO and OGLE projects actually intended to look for gravitational microlensing, along with Hubble telescope did not find enough amount of MACHOs to account for the total dark matter content of the universe [18, 19, 20, 21, 22, 23].

Dark matter can be broadly classified in three categories depending upon their speed. Hot, the one moving with ultra relativistic speed; Cold, the one moving with a non-relativistic speed and finally Warm dark matter with properties intermediate between those of hot dark matter and cold dark matter. Hot dark matter (HDM) is dark matter that is born highly relativistic. Because of its high speed, HDM can escape and thus wash out density perturbations in the early Universe. HDM is constrained to make up a tiny percentage of the mass-energy density of the Universe [24, 25]. Neutrinos are the most favored for candidates for the hot dark matter [6]. Currently the Warm Dark Matter sector is showing potential promises to solve the Dark Matter problem. The most common WDM candidates are *sterile neutrinos* [26, 27, 28] and *gravitinos* [29].

In this thesis we mainly deal with the WIMPs (weakly interacting massive particles) which are cold dark matter particles (CDM). There are some noteworthy success stories for CDM. First and foremost is its success in predicting the initial candidates for structure formation, which culminated in the discovery of the temperature fluctuations in the cosmic microwave background (CMB) [2, 6]. Weakly Interacting Massive Particles (WIMPs) are considered to be the most viable candidate for the dark matter. WIMPs are a generic class of particles which have masses typically in the range from a few GeV to a few TeV. They are characterized by having an interaction cross section that is of a similar order in magnitude as a weak interaction cross section. Examples of WIMPs are the neutralino or sneutrino in supersymmetric theories, or a Kaluza-Klein (KK) excitation of the photon in theories of extra dimensions. This thesis mainly concentrates on this class of dark matter particle. We'll discuss about these in detail later on. Axions are another class of cold dark matter particles finding their origin from strong CP problem [30, 31, 32, 33].

WIMPs as Thermal Relics : WIMPs in principle might be produced in a simple and predictive manner as a thermal relic of the Big Bang [34, 35, 36, 37]. If a

WIMP exists and is stable, it is naturally produced with a relic density consistent with that required of dark matter, the phenomenon being referred to as the “WIMP miracle”. The relic abundance of WIMPs is determined from the “freeze-out” mechanism [35, 38, 39, 40]. Initially the early Universe was very dense and hot, and all particles were believed to be in thermal equilibrium. A WIMP was in chemical and thermal equilibrium with the other constituents of the Universe at early times to start with. If the interaction rate per particle, responsible for keeping the particles in thermal equilibrium bath, stays above the expansion rate of the Universe which is guided by the Hubble constant, the particle will remain in thermal equilibrium with an exponentially suppressed (Boltzmann suppressed) number density [41]. At late times i.e when temperature is small the relic abundance is exponentially lowered. If these particles were to remain in thermal equilibrium indefinitely, their number density would quickly become increasingly suppressed as the universe is cooled. The exponential suppression of the number density of a particle species through self-annihilation can be paused by the competing effect of Hubble expansion. Once the universe expands to large enough size, the particle density becomes so dilute that they can no longer locate one another to annihilate and thus survive to the present day. However, if interaction rate falls below the expansion rate, the particles will decouple, or ‘freeze-out’ from the thermal bath with their number asymptotically approaching a constant, their thermal relic density. If the decoupled particle is stable, this mechanism can give rise to a sizable relic cosmological abundance. The current value as per Planck is $\Omega_\chi h^2 = 0.1196 \pm 0.0031$ (68% C.L) [1].

The identification of dark matter is one of the highest priority goals in cosmology and particle physics and therefore has prompted an enormous proliferation of dark matter candidates, which are currently being sought in an impressive array of accelerators, direct and indirect detection experiments. However, as our understanding of particle physics and astrophysics improves, we are accumulating information that progressively reduces the allowed regions in the parameter space of DM particles. A

compelling solution to the dark matter problem requires synergistic progress along many lines of inquiry. Our primary conclusion is that the diversity of possible dark matter candidates requires a balanced program based on four pillars: direct detection experiments that look for dark matter interacting in the laboratory, indirect detection experiments that connect laboratory signals to dark matter in our own and other galaxies, collider experiments that elucidate the particle properties of dark matter, and astrophysical probes sensitive to non-gravitational interactions of dark matter such as dark matter densities in the centers of galaxies and cooling of stars.

Direct detection experiments aim at detecting the WIMPs, constantly flowing through the Earth that might in principle elastically scatter off the nuclei in underground detectors. By the measurement of nuclear recoils one can find the event rate, energies of nuclear recoils etc. which then can be used to extract various information about the properties of the DM particle.

Scattering of WIMP particles leads to nuclear recoils that can be measured by three different techniques, namely via scintillation, phonons and ionization. There are several experiments DAMA-Libra [42]; CoGeNT [43]; CRESST [44]; CDMS [45, 46, 47]; XENON [48, 49]; ZEPLIN [50, 51]; KIMS [52]; LUX [53, 54]; etc. going on world wide that employ these techniques or a combinations of these to detect the dark matter particles.

The DAMA/LIBRA experiment [55] looks for an annually modulating recoil spectrum as a consequence of the Earth's movement around the Sun during the year. It employs NaI (Tl) (i.e. sodium iodide doped with thallium) as the detector material. This experiment has claimed the detection of a modulation signal with a high significance since many years [56, 57]. However, it appears to be incompatible with other results when it is interpreted as being due to WIMP interactions [58]. The

CoGeNT experiment based on a low mass Ge-detector reaches a very low energy threshold. An initial analysis reported an unexpected excess of events at very low energies [59] but was recently updated using a new analysis that decreased the size of the possible signal, shifting the previously larger signal region to lower cross-sections [60]. In addition to this, CoGeNT also reported an annually modulating signal [61], although this appears to be in conflict with the non-observation of a modulation signal in an analysis by the CDMS-II collaboration, which also uses Ge detectors [62].

Another excess of events was observed by the CRESST experiment [63] that detects both light and heat signals while DAMA and CoGeNT only measure one observable (light or ionization, respectively). A total of 67 events was observed in a WIMP search region, where the excess above the background expectation of around 40 events could be explained by a WIMP signal.

Early in 2013, the CDMS collaboration, that works at cryogenic temperatures at Soudan laboratory, USA to measure the ionization and heat signal from particle interactions [64], reported a new result from the Si detectors. Three events were observed, close to the threshold as expected from WIMP dark matter, while only 0.41 events were expected from the background model. This excess can be interpreted as due to low mass WIMP interactions, with the point of highest likelihood being at a mass of 8.6 GeV and a cross section of $1.9 \times 10^{-41} \text{cm}^2$. The CDMSlite experiment could reach a very low threshold of 0.17 keV and excluded the upper part of the CDMS-Si results [65].

Practically almost all the claims of positive signals are in conflict with the null result of the XENON100 collaboration. This experiment employs a dual-phase time projection chamber (TPC) at LNGS, Italy. The TPC is filled with ultra-pure liquid xenon (LXe) at a low temperature and detects light and charge induced by particle

interactions [66, 67, 68, 69].

There are other experiments that are also looking for direct dark matter signals like EDELWEISS-II, EDELWEISS-III [70, 71] (cryogenic Ge detectors) running in the LSM laboratory in France, a Japanese experimental effort XMASS (LXe single phase detector that tracks light signal) [72], TEXONO [73] (Ge detector), CDEX [74] (Ge detector), DAMIC, DAMIC100 (uses low threshold CCD chips as WIMP targets) [75], PICASSO [76] (superheated droplet detectors), SIMPLE[77] and COUPP [78], DarkSide [79], DEAP[80], CLEAN[81], PandaX [82], XENON1T at LNGS [83]. etc. and many more.

Complementary information on the nature of DM may come from indirect searches, based on the search for secondary products (photons, neutrinos or antimatter) produced in the annihilation or decay of DM particles. In contrast to direct detection experiments, indirect detection efforts do not intend to detect dark matter particles themselves rather they attempt to detect the standard model particles that are produced via their annihilations or decays. Signals for indirect detection experiments include photons (gamma rays, X-rays, radio), neutrinos and cosmic rays (including positrons, electrons, antiprotons, and antideuterons).

Various classes of detectors and telescopes have been designed which range from space and ground based gamma ray telescopes and cosmic ray detectors, to large underground, under ice, and underwater neutrino telescopes [84]. While direct detection experiments require the presence of dark matter in the Earth's neighborhood, this is in general not necessary for indirect detection approaches. In this scenario, one looks for dark matter capture and subsequent annihilation in Solar core as well as one can search for products of dark matter annihilation/decay from regions in the surrounding universe with a high dark matter density like the galactic centre, dwarf spheroidal galaxies, or galaxy clusters. Knowing the halo density distribution and

DM velocity distribution, one can also estimate the probability that dark matter particles encounter each other and annihilate, creating a new source of Standard Model particles.

Super-Kamiokande is a 50,000 ton water Cherenkov detector, located in the Kamioka-Mozumi mine in Japan with 1000 m rock over-burden. For its WIMP search agenda the detector consisted of an inner detector with 11,146 inward-facing 50 cm photomultiplier tubes (PMTs) and an outer detector equipped with 1885 outward-facing 20 cm PMTs, serving as a cosmic ray veto counter. Data was taken from April 1996 to July 2001, corresponding to 1679.6 days of detector livetime. Although no detection has yet been reported, the Super-Kamiokande (S-K) detector has provided upper limits on the possible neutrino flux from WIMP annihilation in the Sun as a function of the WIMP mass [85].

The current large neutrino telescopes like IceCube, a gigantic 1 km^3 neutrino detector corresponding to an instrumented volume of 1 gt installed in the antarctic ice at the South Pole, [86, 87] and ANTARES [88], another neutrino search experiment, located in the Mediterranean Sea in the northern hemisphere searching for dark matter annihilation signals from the Galactic Center, have dark matter search in their scientific programmes. Both experiments have not yet seen any signal.

Among the secondary products from annihilation and/or decay gamma-rays travel in straight lines and are practically unabsorbed in the local Universe. The observational strategies are different for the cases of annihilation and decay. In fact, while in the first case the galactic centre (central source, or surrounding diffuse emission) and possibly a few bright substructures represent the optimal targets, in case of the latter it is best to focus on the diffuse emission at high galactic latitudes, where the astrophysical backgrounds are less intense. The great success of the new generation of air Cherenkov telescopes, and the excitement about the upcoming data from the

Fermi satellite, make this field very lively.

Presently, indirect gamma-ray dark matter detection is evolving very rapidly. Imaging air Cherenkov telescopes, such as HESS [89], MAGIC [90], VERITAS [91], CTA [92], [93] etc. are looking for Dark Matter signals as well. The Fermi collaboration has started to probe the interesting WIMP region by stacking data from several dwarf galaxies [94, 95]. An early possible indication of a dark matter signal in indirect detection was the EGRET excess of GeV photons [96, 97]. However, this was not confirmed by the recent much superior data from Fermi, more exactly the large area gamma-ray telescope part of Fermi, Fermi-LAT, and was probably due to instrument error [98]. Another possible indication of a dark matter signal was the discovery of by INTEGRAL of a 511 keV gamma-line from the galactic centre region [99] however there exist other explanations as well [100]. A rather strong gamma-ray source, consistent with a point source, was detected from the direction of the galactic centre by the HESS experiment [101]. Although many dark matter models were tested, it turned out that the shape of the spectrum (and also the inferred mass, which would exceed some 10 - 20 TeV) made quite poor fits to the distribution of dark matter-induced photons.

Among indirect searches, the antimatter searches provide another avenue along with the photon and neutrino searches. A feature in the positron fraction has been detected above 10 GeV, initially by balloon experiments and then by the PAMELA satellite [102], that cannot easily be attributed to cosmic-ray secondary production of positron. The ATIC experiment [103] also reported a rise in the positron flux, followed by a sharp drop just below 1 TeV. The possibility of dark matter detection was extensively discussed in literature a few years ago [104, 105] as the Fermi -LAT collaboration along with the PAMELA collaborations discovered an anomalously high ratio of positrons over electrons up to 100 GeV [102], and sum of positrons and electrons up to 1 TeV [106]. During the last years, this anomaly, although

possible to explain by dark matter annihilation, was shown to need very large boost factors (e.g., from Sommerfeld enhancement), and specific particle physics models such as leptophilic models. On the other hand, certain astrophysical explanations of these observations are possible with quite standard assumptions. Though the dark matter explanation is not yet ruled out, but it sees tension from other measurements, especially from gamma-ray data [107]. It may thus in principle be due to DM [108, 109], with rather unusual properties, or a more mundane source such as creation of electron positron pairs from pulsars and other supernova remnants [110, 111]. Recently the AMS02 instrument on the International Space Station (ISS) confirmed the excess observed by PAMELA [102], which keeps increasing up to energies of 300 GeV [112], the current high energy limit of the instrument.

By analyzing public Fermi-LAT data, an excess in the few GeV gamma-ray energy region has recently been proposed to be caused by dark matter annihilation. This is an extended emission corresponding to a gamma-ray source in the region of the galactic centre [113, 114, 115]. Again, this possible dark matter effect (with a mass around 10 GeV) is unexplained at the moment, but astrophysical explanations are of course possible in this crowded part of the galaxy [116, 117]. More recently, a gamma-ray excess from galaxy clusters ascribed to dark matter has also been claimed again using public Fermi data [118]. Another excess, again a discovery that has been made using public Fermi data, the WMAP radio “haze” found by Ref. [119] has recently been seen to have a correspondence in the GeV range in the so-called “Fermi bubbles” [120]. These are sharply defined regions, several tens of degrees across, on both sides of the galactic disk that seem to originate from the galactic center [121, 122]. An intriguing feature has been found in Ref. [123], again by using public Fermi-LAT data [124, 125] which is a structure similar to what is expected for internal bremsstrahlung, or alternatively a narrow gamma-ray line, is visible in the energy range between 130 and 150 GeV. At energies, say, below 150 GeV, the Fermi-LAT instrument will be difficult to surpass by using imaging

air Cherenkov telescopes like the CTA, which have their greatest sensitivity in the TeV region. However, an interesting Russian-Italian project GAMMA-400 [126] is underway, which has a planned launch around 2018 approved and is planned with a slightly smaller effective area than Fermi-LAT, but with better angular resolution and in particular better energy resolution than that of Fermi-LAT by an order of magnitude. This would take the search for dark matter to another level of sensitivity. If the present indication of a line signal would persist, it should be seen in GAMMA-400 with a significance of the order of 10σ .

Accelerator measurements will be invaluable to establish the existence of dark matter particles. Particle colliders, such as the Large Hadron Collider (LHC) and proposed future lepton colliders [127, 128, 129, 130, 131] might produce dark matter particles, which escape the detector, but are discovered as an excess of events with missing energy or momentum. Astrophysical uncertainties are completely absent in collider results, however, the very limited time a particle spends in the detector will make it almost impossible to prove from collider data alone, that a detected candidate is the dark matter particle.

Non-gravitational interactions of dark matter affect a variety of astrophysical observables, including the number density and internal structure of galaxies. The particle properties of dark matter are constrained through its impact on astrophysical observables. Examples include self-interaction of dark matter particles affecting central dark matter densities in galaxies (inferred from rotation velocity or velocity dispersion measures), mass of dark matter particle affecting dark matter substructure in galaxies (inferred from strong lensing data) and annihilation of dark matter in the early Universe affecting the Cosmic Microwave Background fluctuations. In addition to structure formation, non-gravitational interactions of dark matter could impact a variety of other astrophysical phenomena. Coupling of axions and light sterile neutrinos (or generally any light hidden sector particles) to standard model parti-

cles may affect the cooling of compact objects (stars, neutron stars, white dwarfs, supernovae) or the transparency of extra galactic background light to high-energy photons, which leads to stringent constraints on models [132].

Having discussed all the detection scenario above it is very important to point out that one needs two crucial inputs to analyze all the data gathered by the large number of detectors. These are specifically the astrophysical inputs, namely, local dark matter density and velocity distribution. The DM particles in our Galaxy constitute a spherical halo within which the visible matter structure consisting of a spherical bulge and double exponential disk is embedded.

The motion of the dark matter particles in the halo is described by their phase space distribution function (PSDF) [133]. This PSDF is a priori unknown. One possible way to find out the PSDF is by making an assumption that dark matter particles are collisionless system of particles which is a quite valid assumption as the DM particles hardly interact. As the collisionless system of particles satisfy the collisionless Boltzmann equation (CBE) therefore one possible ansatz for phase space distribution of the dark matter particles can be the solutions of CBE. The mostly adopted solution in the literature of the CBE is the isothermal PSDF. The velocity distribution resulting from the isothermal PSDF is Maxwellian distribution. The so called “Standard Halo Model” (SHM) is the isothermal PSDF with Maxwellian velocity distribution and the solar location density value 0.3 GeV cm^{-3} . Since the isothermal distribution is not finite in both configuration space and velocity space, the velocity distribution is truncated by hand at a given value of velocity. There have been many earlier works in literature on this that can be found in the following references [56, 57, 58, 134].

Whereas the SHM serves as a useful benchmark model, there are a number of reasons why the SHM does not provide a satisfactory description of the dynamics of the

Galaxy. The non-finite extent of the SHM makes the mass of the system a divergent one and hence can not represent a physical galaxy. Further to this, truncation of the velocity space no longer lets the system remain a solution of the CBE. These problems can be overcome by adopting other solutions of the CBE which do not suffer from such non finiteness problem, for example one can consider King model, Michie model etc. These solutions have truncation in both configuration and velocity space that is self-consistently determined by the system itself. In addition to this Michie model has another important feature which is the velocity anisotropy as predicted by recent numerical simulations as well. These will be discussed in more detail in coming chapters.

Another alternative approach to find the phase space distribution function is by starting from a density distribution, that is motivated from numerical simulations, then reverting it using Eddington's methodology [133, 135]. This approach is discussed in detail in Chapter II where we show that starting from the NFW distribution [136] we have obtained the phase space distribution as a function of the total energy and then we have also calculated the local velocity distribution function. The model parameters are obtained by performing fit to observational data using Markov Chain Monte Carlo technique.

In order to determine the values of the parameters of the models of the phase space distributions adopted or derived by any method one first needs to consider some observational data as mentioned above. For our purpose we have used here the rotation curve data, which is basically the rotation velocity of a test particle with respect to the Galactic centre. There are several works in literature on the construction of the RC data [137, 138, 139, 140, 141, 142]. Most of them provide rotation curve data upto a distance not large enough to probe the DM structure of the Galaxy beyond the visible edge. Therefore, we have constructed the rotation curve data extending to large galactocentric distance in a model independent way

starting from the observations on various class of tracers [143]. We have studied its dependence on various parameters such as the Galactic constants, namely the distance of Sun from Galactic centre and its local circular speed and also the tracer velocity anisotropy in Chapter III.

The first part of this thesis concentrates on extracting information about the phase space distribution of dark matter particles. First in Chapter II we have adopted the Eddington's inversion method then in Chapter IV we present another approach, similar to that of the Standard Halo model discussed above, to find the phase space distribution of the dark matter starting from the solution of collisionless Boltzmann equation, namely Michie model [133, 144]. This model has several advantages over SHM as it has finite cut in both configuration space and the velocity space self-consistently determined by the model itself. Further the Michie model takes into account the velocity anisotropy of the distribution as also suggested by recent numerical simulations. The effect of the visible matter distribution on the dark matter distribution is self-consistently included in the system and the system converges in an iterative manner. We present the method and the results in Chapter IV.

Local dark matter density and the velocity distribution are the two crucial inputs for the analysis of the experimental results of both direct and indirect detection of dark matter particles. In the second part of the thesis we focus on the indirect detection of WIMPs [2, 3, 4, 6, 145, 146] through neutrino signal due to WIMP annihilation in the Sun. In Chapter V we specifically discuss indirect detection of WIMPs through neutrino signal due to capture and annihilation of the WIMPs inside the Sun within the context of a self-consistent model of the phase space structure of the finite sized DM halo of the Galaxy. The model is based on the so called "King model", the PSDF of which is a solution of collisionless Boltzmann equation (CBE). The model is properly modified to include the effect of the gravitational influence of the observed visible matter (VM) in a self consistent manner, with the parameters of

the model determined by fit to the observed RC data for the Galaxy extending upto large Galactic radii. We have derived the capture rate and the annihilation rate of WIMPs in the Sun within the context of above mentioned King model [146].

In Chapter VI we calculate the expected neutrino flux from the Sun due to annihilation of WIMPs captured and accumulated inside the Sun, and derive constraints on the WIMP-nucleon elastic scattering cross section from the upper limits on the flux of such neutrinos given by the Super-Kamiokande experiment [147]. We further present the upper limits on the branching fractions of various possible WIMP annihilation channels from the requirement of compatibility with DAMA results [146]. At a qualitative level the general conclusion reached earlier [148, 149] within the context of the SHM, that S-K upper limits on neutrinos from the Sun severely restrict the DAMA-compatible region of the WIMP parameter space, remains true in the present model too, thus adding robustness to this conclusion.

Finally in Chapter VII we highlight the main findings of the thesis in a nutshell and conclude by mentioning the possible future directions in this area of dark matter dynamics and detection by indirect means.

Chapter 2

Phase Space Distribution of the Dark Matter in our Galaxy

2.1 Introduction

The local dark matter (DM) density and velocity distribution are two crucial astrophysical inputs for analyzing the results of the dark matter detection experiments being operated worldwide. There have been many studies on estimating the local dark matter density from a variety of observational constraints [150]. However not much knowledge directly based on observational data is available on the likely form of the velocity distribution function (VDF) of the WIMPs in the Galaxy.

In this chapter we attempt to extract information about the local density and the VDF of the DM particles using the observed rotation curve data of the Galaxy. The motion of the dark matter particles in the halo is described by their Phase Space Distribution Function (PSDF) $f(\mathbf{x}, \mathbf{v})$ [133] where $f(\mathbf{x}, \mathbf{v}) d^3\mathbf{x}d^3\mathbf{v}$ is the number of DM particles within the volume $d^3\mathbf{x}$ centered on \mathbf{x} and within velocity range $d^3\mathbf{v}$ centered on \mathbf{v} at a particular time t . Clearly $f \geq 0$. As the PSDF is a priori

unknown one has to start from an ansatz. The WIMPs being weakly interacting, their PSDF can be assumed to satisfy the collisionless Boltzmann equation (CBE) given by,

$$\frac{df}{dt} \equiv \frac{\partial f}{\partial t} + \sum_{\alpha=1}^6 \dot{w}_{\alpha} \frac{\partial f}{\partial w_{\alpha}} = 0, \quad (2.1)$$

with $\mathbf{w} \equiv (\mathbf{x}, \mathbf{v})$ and $\dot{\mathbf{w}} \equiv (\dot{\mathbf{x}}, \dot{\mathbf{v}}) \equiv (\mathbf{v}, -\nabla\Phi(\mathbf{x}))$.

Here $\Phi(\mathbf{x})$ is the smooth gravitational potential under the influence of which particles move. The collisionless system is considered to behave like an ordinary fluid that obeys continuity equation. We shall be interested in PSDFs that are steady state solutions of the CBE. Solving CBE is not straight forward because it involves many independent variables. However one can choose some plausible forms of the PSDF guided by the “*Jeans Theorem*” [133], which states that,

Any steady state solution of the collisionless Boltzmann equation depends on the phase space coordinates only through integrals of motion in the given potential and any function of the integrals yields a steady state solution of the collisionless Boltzmann equation.

If $I[\mathbf{x}(t), \mathbf{v}(t)]$ is an *integral of motion* then it satisfies

$$\begin{aligned} \frac{d}{dt} I[\mathbf{x}(t), \mathbf{v}(t)] &= 0, \\ \text{and } \mathbf{v} \cdot \nabla I - \nabla\Phi(\mathbf{x}) \cdot \frac{\partial I}{\partial \mathbf{v}} &= 0. \end{aligned} \quad (2.2)$$

So, I , by its definition satisfies the condition to be a solution of steady state CBE.

For a particle moving in a trajectory under the influence of a spherical potential, only four isolating integrals of motion, namely *energy* and three components of *angular momentum* are allowed. If the system has spherical symmetry then f depends only

on the energy and magnitude of angular momentum of the system $f = f(E, L)$.

It is convenient to define the *relative potential* (Ψ) and *relative energy* (\mathcal{E}) as [133]

$$\Psi(\mathbf{x}) = -\Phi(\mathbf{x}) + \Phi_0 ; \mathcal{E} = -E + \Phi_0 = -\Phi(\mathbf{x}) - \frac{1}{2}v^2 + \Phi_0 = \Psi(\mathbf{x}) - \frac{1}{2}v^2 ,$$

where the constant Φ_0 can be chosen in such a way that $f > 0$ for $\mathcal{E} > 0$ and $f = 0$ for $\mathcal{E} \leq 0$.

The potential of an isolated system satisfies the Poisson's equation given below,

$$\nabla^2\Phi(\mathbf{x}) = 4\pi G\rho(\mathbf{x}),$$

$$\Rightarrow \nabla^2\Psi(\mathbf{x}) = -4\pi G\rho(\mathbf{x}) = -4\pi G \int f(\mathbf{x}, \mathbf{v})d^3\mathbf{v} = -4\pi G \int f[\Psi(\mathbf{x}), \mathbf{v}]d^3\mathbf{v}, \quad (2.3)$$

where $\rho(\mathbf{x}) = \int f(\mathbf{x}, \mathbf{v})d^3\mathbf{v}$ is the density distribution. This non linear equation for $\Psi(\mathbf{x})$ can be solved by assuming physical yet simple forms of $f(\mathbf{x}, \mathbf{v})$.

In this chapter our goal is to derive the local dark matter density and velocity distribution which are two crucial inputs for the analysis of the dark matter detection results. In Section 2.2 we discuss the pros and cons of the widely used so called standard halo model (SHM) of the phase space distribution function of the DM halo of our Galaxy. Then in Section 2.3 we discuss another method to derive the local DM density and the velocity distribution of DM particles. Starting from a given density distribution, that could be one motivated by cold dark matter numerical simulations, we “invert” it to obtain the phase space distribution function of the system and hence derive the velocity distribution function in Section 2.3. Next in Section 2.4 we present the results obtained by fitting the observational data, namely the rotation curve data of the Galaxy, using the Markov Chain Monte Carlo (MCMC) technique, to find the values of the parameters of the Dark matter and visible matter models adopted.

2.2 Standard Halo Model (SHM) :

For a spherical system, the Jeans theorem allows the steady state PSDF, $f(\mathbf{x}, \mathbf{v})$, to be a function of only the total energy \mathcal{E} . Of particular interest is the ‘‘Isothermal model’’ defined in the following way [133],

$$f(\mathbf{x}, \mathbf{v}) = f(\mathcal{E}) = \frac{\rho_1}{(2\pi\sigma^2)^{3/2}} e^{\mathcal{E}/\sigma^2} = \frac{\rho_1}{(2\pi\sigma^2)^{3/2}} \exp\left(\frac{\Psi(\mathbf{x}) - \frac{1}{2}v^2}{\sigma^2}\right), \quad (2.4)$$

where ρ_1 is a density parameter and σ is a velocity parameter of the system. Integrating equation (2.4) over all velocities, one can get the density distribution,

$$\rho(\mathbf{x}) = \rho_1 e^{\Psi(\mathbf{x})/\sigma^2}. \quad (2.5)$$

The velocity distribution at location \mathbf{x} comes out to be a Maxwellian as given below

$$f(\mathbf{v}) = \frac{1}{(2\pi\sigma)^3} \exp\left(-\frac{v^2}{2\sigma^2}\right). \quad (2.6)$$

This ‘‘Isothermal’’ model is the mostly adopted model for PSDF of DM in literature. The density parameter ρ_1 can be related to the density of DM in the solar neighborhood (ρ_\odot) which is typically taken to be in the range $0.3 \pm 0.1 \text{ GeV cm}^{-3}$ [151, 152, 153, 154].

The velocity parameter σ is related to the velocity dispersion of the Isothermal model ($\langle v^2 \rangle = 3\sigma^2$) and the value of the velocity dispersion at solar location is taken as $\sim 270 \text{ km s}^{-1}$. This follows from the relation [133] $\langle v^2 \rangle^{1/2} = \sqrt{\frac{3}{2}} v_{c,\infty}$ between the velocity dispersion of the particles constituting a single-component self-gravitating isothermal sphere and the asymptotic value of the circular rotation speed, $v_{c,\infty}$, of a test particle in the gravitational field of the isothermal sphere and assuming $v_{c,\infty} \approx v_{c,\odot} \approx 220 \text{ km s}^{-1}$, where $v_{c,\odot}$ is the measured value of the circular rotation speed of the Galaxy in the solar neighborhood. The isothermal model as described

above together with the above mentioned values of the parameter is customarily referred to as the Standard Halo Model (SHM). In this model the infinite velocity tail of the Maxwellian velocity distribution is truncated at a chosen value of escape speed as obtained from various surveys.

Whereas the SHM serves as a useful benchmark model, there are a number of reasons why the SHM does not provide a satisfactory description of the dynamics of the Galaxy. First, it does not take into account the modification of the phase space structure of the DM halo due to the significant gravitational effect of the observed visible matter on the DM particles inside and up to the solar circle. Second, the isothermal sphere model of the halo is infinite in extent and has a formally divergent mass, with mass inside a radius r , $M(r) \propto r$, as $r \rightarrow \infty$, and is thus unsuitable for representing a halo of finite size. Third, the procedure of truncating the Maxwellian speed distribution at a chosen value of the local (solar neighborhood) escape speed is not a self-consistent one because the resulting speed distribution is not in general a self-consistent solution of the steady-state collisionless Boltzmann equation (CBE) describing a finite system of collisionless DM particles. In addition, since the rotation curve for such a truncated Maxwellian is, in general, not asymptotically flat, the relation $\langle v^2 \rangle^{1/2} = \sqrt{\frac{3}{2}} v_{c,\infty}$ used to determine the value of $\langle v^2 \rangle^{1/2}$ in the Maxwellian speed distribution of the isothermal sphere, as done in the SHM, is not valid in general. Finally, recent numerical simulations [154] have also found that the velocity distribution of the Dark Matter particles deviates significantly from the usual Maxwellian form.

There are various ways to overcome the shortcomings of the SHM described above by considering other solutions of the CBE such as the “King model” which takes into account the truncation of configuration space and velocity space in a self-consistent manner [155, 156]. Though the King model or Lowered Isothermal model serves its purpose nicely still it generates a velocity distribution profile which is isotropic

in nature in contradiction with observations from various simulations that find the VDF to be anisotropic in nature. To overcome this one can consider the anisotropic version of the King model namely Michie model which is described in later chapters.

2.3 Deriving the velocity distribution function from a given density profile : Eddington formalism

The VDF of the DM particles at any location in the Galaxy is self-consistently related to their spatial density as well as to the *total* gravitational potential, $\Phi(\mathbf{x})$, at that location. For a spherical system of collisionless particles (WIMPs, for example) with isotropic VDF satisfying the collisionless Boltzmann equation, the Jeans theorem [133] ensures that the phase space distribution function (PSDF), $f(\mathbf{x}, \mathbf{v})$, depends on the phase space coordinates (\mathbf{x}, \mathbf{v}) only through the total energy (per unit mass), $E = \frac{1}{2}v^2 + \Phi(r)$, where $v = |\mathbf{v}|$, $r = |\mathbf{x}|$. For such a system, given a isotropic spatial density distribution $\rho(r) \equiv \int d^3\mathbf{v} f(\mathcal{E})$, one can get a unique $f(\mathbf{x}, \mathbf{v})$ by the Eddington formula [157, 133] given by,

$$f(\mathcal{E}) = \frac{1}{\sqrt{8\pi^2}} \left[\int_0^{\mathcal{E}} \frac{d\Psi}{\sqrt{\mathcal{E} - \Psi}} \frac{d^2\rho}{d\Psi^2} + \frac{1}{\sqrt{\mathcal{E}}} \left(\frac{d\rho}{d\Psi} \right)_{\Psi=0} \right], \quad (2.7)$$

where $\Psi(r) \equiv -\Phi(r) + \Phi(r = \infty)$ is the relative potential and $\mathcal{E} \equiv -E + \Phi(r = \infty) = \Psi(r) - \frac{1}{2}v^2$ is the relative energy, with $f(\mathcal{E}) > 0$ for $\mathcal{E} > 0$, and $f(\mathcal{E}) = 0$ for $\mathcal{E} \leq 0$, as described in previous section. The latter condition implies that at any location r , the VDF, $f(\mathbf{v}) = f(\mathcal{E})/\rho(r)$, has a natural truncation at a maximum value of v , namely, $v_{\max}(r) = \sqrt{2\Psi(r)}$.

Thus, given a isotropic density profile of a set of collisionless particles, we can calculate the VDF, $f(\mathbf{v})$, using equation (2.7) provided the total gravitational potential $\Phi(r)$ in which the particles move is known. A direct observational probe of $\Phi(r)$ is

provided by the rotation curve (RC) of the Galaxy, the circular velocity of a test particle as a function of the Galactocentric distance. In this section we reconstruct the total gravitational potential $\Phi(r)$ in the Galaxy directly from the Galactic RC data and then use equation (2.7) to obtain the VDF, $f(\mathbf{v})$, of the WIMPs at any location in the Galaxy.

We shall assume that the DM density profile to be used on the right hand side of equation (2.7) is of the universal Navarro-Frenk-White (NFW) [158] form, which, when normalized to DM density at solar location, $\rho_{\text{DM},\odot}$, can be written as

$$\rho_{\text{DM}}(r) = \rho_{\text{DM},\odot} \left(\frac{R_{\odot}}{r} \right) \left(\frac{r_s + R_{\odot}}{r_s + r} \right)^2, \quad (2.8)$$

where R_{\odot} is the distance of Sun from the Galactic centre. The NFW model is considered the universal profile that can very nicely describe the the cold DM halos produced in numerical N-body simulations. At long distance it reproduces the actual results but near the centre it has a cuspy nature. The central region is mostly dominated by the visible matter therefore we can proceed with NFW profile here as a reasonably good density model to describe the DM distribution. The profile given by equation (2.8) has two free parameters, namely, the density $\rho_{\text{DM},\odot}$ and the scale radius r_s .

The *total* gravitational potential seen by the DM particle, Φ , is given by $\Phi = \Phi_{\text{DM}} + \Phi_{\text{VM}}$, where Φ_{DM} is the DM potential corresponding to the density distribution given by equation (2.8) and Φ_{VM} is the total potential due to the visible matter (VM) component of the Galaxy. The VM can be effectively modeled [159] in terms of a spheroidal bulge superposed on an axisymmetric disk, with density distributions given, respectively, by,

$$\text{Bulge : } \rho_b = \rho_{b0} (1 + (r/r_b)^2)^{-3/2},$$

where ρ_{b0} and r_b are the central density and scale radius of the bulge, respectively, and

$$\text{Disk : } \rho_d(R, z) = \frac{\Sigma_\odot}{2z_d} e^{-(R-R_\odot)/R_d} e^{-|z|/z_d},$$

where R and z are the axisymmetric cylindrical coordinates with $r = (R^2 + z^2)^{1/2}$, R_d and z_d are the scale length and scale height of the disk, respectively, and Σ_\odot is its local surface density. The corresponding gravitational potentials for these density models, Φ_{bulge} and Φ_{disk} , can be easily obtained by numerically solving the respective Poisson equations, giving $\Phi_{\text{VM}} = \Phi_{\text{bulge}} + \Phi_{\text{disk}}$.

The density models specified above have a total of seven free parameters, namely, r_s , $\rho_{\text{DM},\odot}$, ρ_{b0} , r_b , Σ_\odot , R_d , and z_d . We determine the most-likely values and the 68% C.L. upper and lower ranges of these parameters by performing a Markov Chain Monte Carlo (MCMC) analysis (see, e.g., Refs. [160]) using the observed RC data of the Galaxy.

2.4 Results : Local DM density, Velocity distribution function and physically relevant quantities

For a given set of the Galactic model parameters, the circular rotation speed, $v_c(R)$, as a function of the Galactocentric distance R , is given by,

$$v_c^2(R) = R \frac{\partial}{\partial R} \left[\Phi_{\text{DM}}(R, z=0) + \Phi_{\text{VM}}(R, z=0) \right]. \quad (2.9)$$

For the observational data, we use RC data given in [161] that extends to Galactocentric distances well beyond the visible edge of the Galaxy. This data set

Parameter Units	r_s kpc	$\rho_{\text{DM},\odot}$ GeV/cm ³	$\rho_{\text{b0}} \times 10^{-4}$ GeV/cm ³	r_b kpc	Σ_{\odot} M_{\odot}/pc^2	R_d kpc
Most-likely	30.36	0.19	1.83	0.092	57.9	3.2
Lower	14.27	0.17	1.68	0.083	55.51	2.99
Upper	53.37	0.23	2.0	0.102	58.0	3.27
Mean	41.35	0.20	1.84	0.092	54.30	3.14
SD	20.51	0.02	0.059	0.001	3.47	0.11

Table 2.1: The most-likely values of the Galactic model parameters, as well as their 68% C.L. lower and upper ranges, means and standard deviations (SD), obtained from our MCMC analysis using the observed rotation curve data.

corresponds to a choice of the Local Standard of Rest (LSR) set to $(R_0, V_0) = (8.0 \text{ kpc}, 200 \text{ km s}^{-1})$. For the MCMC analysis, we use the χ^2 -test statistic defined as $\chi^2 \equiv \sum_{i=1}^{i=N} \left(\frac{v_{\text{c,obs}}^i - v_{\text{c,th}}^i}{v_{\text{c,error}}^i} \right)^2$, where $v_{\text{c,obs}}^i$ and $v_{\text{c,error}}^i$ are, respectively, the observational value of the circular rotation speed and its error at the i -th value of the Galactocentric distance, and $v_{\text{c,th}}^i$ is the corresponding theoretically calculated circular rotation speed given by equation (2.9).

For priors on the free parameters involved, we have taken the following ranges of the relevant parameters based on currently available observational knowledge : For the VM parameters, $\rho_{\text{b0}} : [0.1 - 2] \times 4.2 \times 10^2 M_{\odot} \text{ pc}^{-3}$ [159]; $r_b : [0.01 - 0.2] \times 0.103 \text{ kpc}$ [159]; $\Sigma_{\odot} : [35 - 58] M_{\odot} \text{ pc}^{-2}$ [162]; $R_d : [1.7 - 3.5] \text{ kpc}$ [163, 159]. The parameter z_d has been fixed at 340 pc [164] since the results are fairly insensitive to this parameter. For the DM parameters we took a wide prior range for $r_s : [0.1 - 100] \text{ kpc}$ and $\rho_{\text{DM},\odot} : [0.1 - 0.5] \text{ GeV cm}^{-3}$ consistent with values quoted in literature [150].

The results of our MCMC analysis are summarized in Table 2.1 and Figure 2.1. Figure 2.2 shows the theoretically calculated rotation curve for the most-likely set of values of the Galactic model parameters obtained from the MCMC analysis, listed in Table 2.1, and its comparison with the observed rotation curve data. In Table 2.2, we display the values of some of the physical quantities of interest characterizing the Galaxy, derived from the Galactic parameters listed in Table 2.1. The values

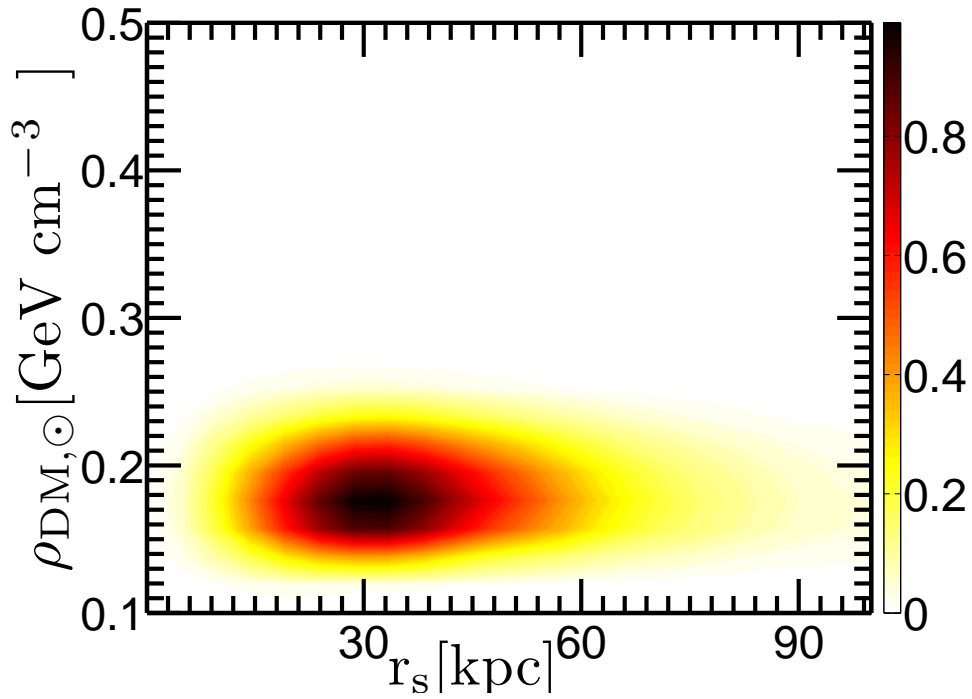


Figure 2.1: The 2D posterior probability density function for Dark Matter parameters ($r_s - \rho_{DM,\odot}$), marginalized over the visible matter parameters.

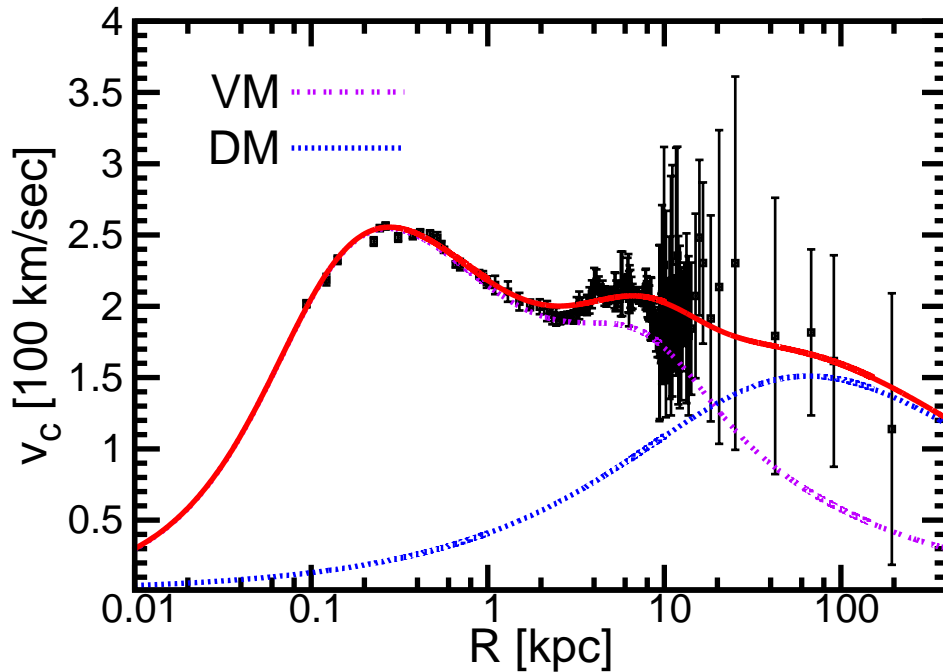


Figure 2.2: Rotation curve of the Galaxy with the most-likely set of values of the Galactic model parameters listed in Table 2.1. The data with error bars are from Ref. [161].

Derived Quantities	Unit	Values
Bulge mass (M_b)	$10^{10} M_\odot$	$3.53^{+1.81}_{-1.29}$
Disk mass (M_d)	$10^{10} M_\odot$	$4.55^{+0.2}_{-0.22}$
Total VM mass ($M_{VM} = M_b + M_d$)	$10^{10} M_\odot$	$8.07^{+2.01}_{-1.51}$
DM Halo virial radius (r_{vir})	kpc	$199.0^{+75}_{-53.5}$
Concentration parameter ($\frac{r_{vir}}{r_s}$)	—	$6.55^{+5.01}_{-2.05}$
DM halo virial mass (M_h)	$10^{11} M_\odot$	$8.61^{+14.01}_{-5.22}$
Total mass of Galaxy ($M_{VM} + M_h$)	$10^{11} M_\odot$	$9.42^{+14.21}_{-5.37}$
DM mass within R_\odot	$10^{10} M_\odot$	$1.89^{+0.72}_{-0.3}$
Total mass within R_\odot	$10^{10} M_\odot$	$7.09^{+1.9}_{-1.15}$
Total surface density :		
at R_\odot ($ z \leq 1.1$ kpc)	$M_\odot \text{ pc}^{-2}$	$69.21^{+2.52}_{-3.55}$
Total Mass within 60 kpc	$10^{11} M_\odot$	$3.93^{+2.15}_{-1.41}$
Total Mass within 100 kpc	$10^{11} M_\odot$	$5.92^{+4.35}_{-2.56}$
Local Circular velocity ($v_{c,\odot}$)	km s^{-1}	$206.47^{+24.67}_{-16.3}$
Local maximum velocity ($v_{max,\odot}$)	km s^{-1}	$516.02^{+120.85}_{-97.58}$

Table 2.2: The most-likely values of various relevant physical parameters of the Milky Way and their upper and lower ranges derived from the most-likely- and 68% C.L. upper and lower ranges of values of the Galactic model parameters listed in Table 2.1.

in Table 2.2 are in reasonably good agreement with the values of these quantities quoted in recent literature [165, 161, 166]. The relatively large uncertainties in the values of some of the quantities that receive dominant contribution from the DM halo properties at large Galactocentric distances are simply a reflection of the relatively large uncertainties of the rotation curve data at those distances.

The Galactic model parameters determined above allow us to reconstruct the total gravitational potential $\Phi(\mathbf{x})$ at any location in the Galaxy. Because of the axisymmetric nature of the VM disk, this potential is non-spherical. To use equation (2.7), which is valid only for a spherically symmetric situation, we use the spherical approximation [167, 165], $\Phi_{VM}(r) \simeq G \int_0^r M_{VM}(r')/r'^2 dr'$, where M_{VM} is the total VM mass contained within r . The spherical approximation is inevitable as we have employed Eddington's method which rests on the assumption that the potential and density profiles are spherically symmetric. Therefore we had to apply this approximation to VM potentials in our case, which is actually axisymmetric in nature. The error

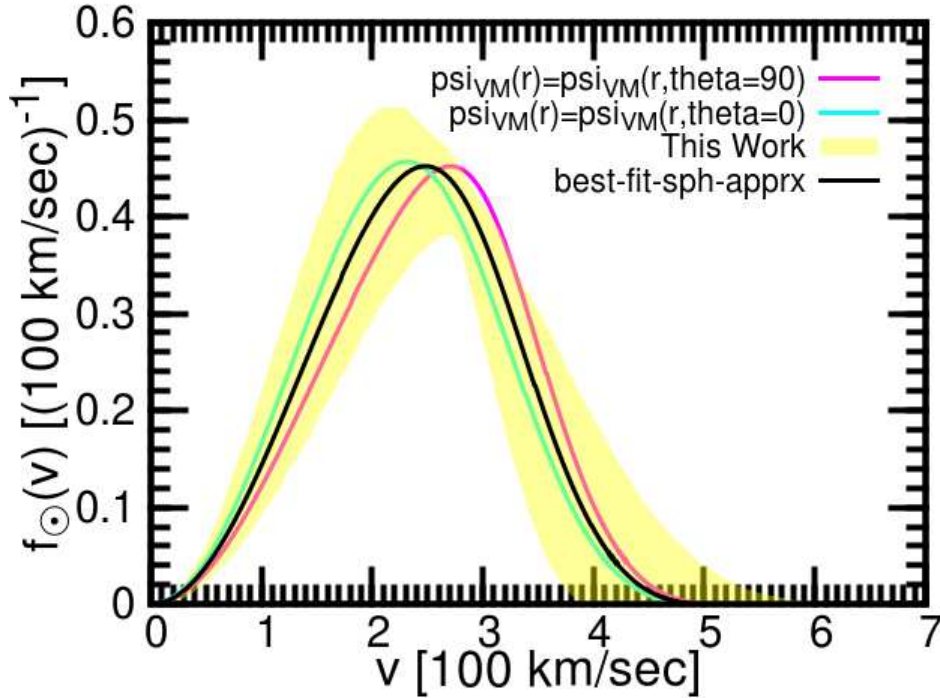


Figure 2.3: The local VDF for the approximated Visible Matter potential $\Phi_{\text{VM}}(r)$ and the local VDFs for the VM potentials in $z=0$ $\Phi_{\text{VM}}(r, \theta = \pi/2)$ plane and along z -axis $\Phi_{\text{VM}}(r, \theta = 0)$ respectively are presented. The plot shows that the local VDF for the approximated Visible matter potential is kind of an average between the local VDFs obtained with $\Phi_{\text{VM}}(r, \theta = \pi/2)$ and $\Phi_{\text{VM}}(r, \theta = 0)$.

introduced in the final result is due to this approximation which we can calculate in terms of the percentage error in the VM potential at solar neighborhood which comes out to be $\leq 10\%$ which is insignificant compared to the uncertainty introduced from the Circular Speed data itself. The approximated $\Phi_{\text{VM}}(r)$ we have used is kind of a average between $\Phi_{\text{VM}}(r, \theta = \pi/2)$ and $\Phi_{\text{VM}}(r, \theta = 0)$. If the local VDF is drawn with these above mentioned VM potentials for these two extreme cases, they lie completely within the actual VDF uncertainty (due to RC curve) band as shown in Figure 2.3.

The resulting normalized speed distribution, $f(v) \equiv (4\pi v^2) f(\mathbf{v})$ (with $\int f(v) dv = 1$), evaluated at the location of the Sun, giving the most-likely $f_{\odot}(v)$, is shown in Figure 2.4. For comparison, we also show in the same Figure the best Maxwellian fit (with $f_{\odot}^{\text{Maxwell}}(v) \propto v^2 \exp(-v^2/v_0^2)$) to the most-likely $f_{\odot}(v)$ obtained from MCMC

analysis.

As evident from Figure 2.4, the speed distribution differs significantly from the Maxwellian form. We find that the following parametrized form, which goes over to the standard Maxwellian form in the limit of the parameter $k \rightarrow 0$, gives a good fit to our numerically obtained most-likely local speed distribution shown in Figure 2.4:

$$f_{\odot}(v) \approx 4\pi v^2 (\xi(\beta) - \xi(\beta_{\max})) , \quad (2.10)$$

where $\xi(x) = (1+x)^k e^{-x^{(1-k)}}$, $\beta = v^2/v_0^2$, $\beta_{\max} = v_{\max,\odot}^2/v_0^2$, $v_0 = 339 \text{ km s}^{-1}$ and $k = -1.47$.

As a quantitative measure of the deviation of a model form of the local speed distribution, f^{model} , from the numerically obtained most-likely (ML) form, f^{ML} , shown in Figure 2.4, the quantity $\chi_f^2 \equiv (1/N) \sum_{i=1}^N [f^{\text{ML}}(v_i) - f^{\text{model}}(v_i)]^2$ has a value of $\sim 7.2 \times 10^{-5}$ for the parametrized form (2.10) compared to a value $\sim 1.7 \times 10^{-3}$ for the best Maxwellian fit shown in Figure 2.4. We also compare our results with those from four large N-body simulations [168] in Figure 2.5. Note also that our results differ significantly from those obtained from the N-body simulations.

In Figure 2.6 we show the most-likely $f(v)$'s at several different values of the Galactocentric distance r . It may be noted that the peak of the distribution shifts towards smaller values of v and the width of the distribution shrinks, as we go to larger r , with the distribution eventually becoming a delta function at zero speed at asymptotically large distances, as expected. The non-Maxwellian nature of the distribution at all locations is also clearly seen, with the Maxwellian approximation always overestimating the number of particles at both low as well as extreme high velocities.

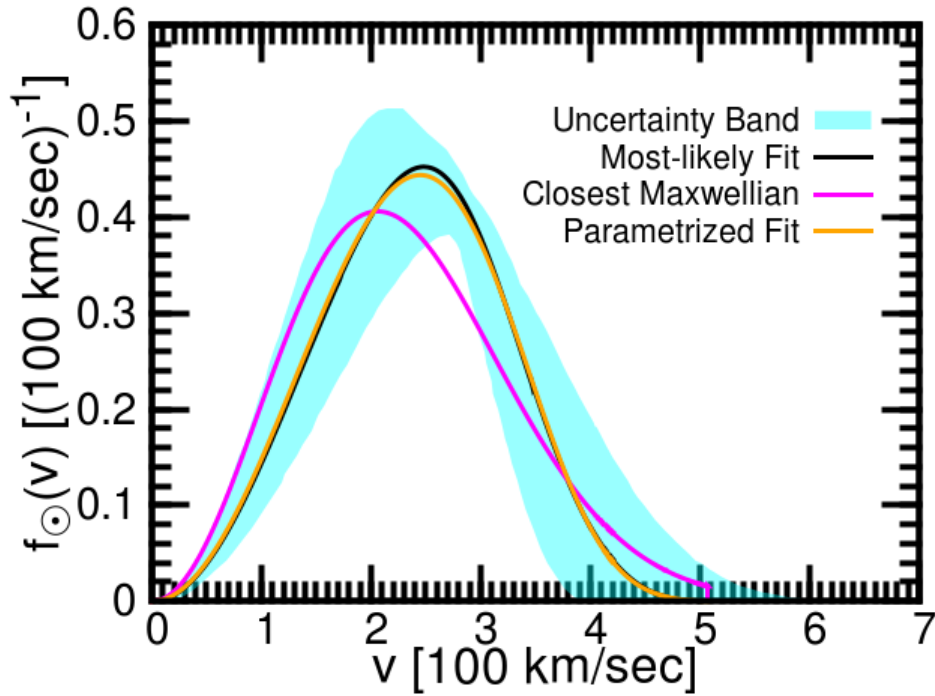


Figure 2.4: Normalized local speed distribution, $f_{\odot}(v)$, corresponding to the most-likely (ML) set of values of the Galactic model parameters given in Table 2.1 (black curve) and its uncertainty band (cyan band) corresponding to the 68% C.L. upper and lower ranges of the Galactic model parameters. The best parametrized non-Maxwellian (orange curve) fit (equation 2.10 — almost indistinguishable from the ML curve) as well as the closest Maxwellian fit (pink curve), the latter with the form $f_{\odot}^{\text{Maxwell}}(v) \propto v^2 \exp(-v^2/v_0^2)$ truncated at $v_{\text{max},\odot} = 516 \text{ km s}^{-1}$ (see Table 2.2) and with the free parameter v_0 determined to be 206 km s^{-1} , are also shown.

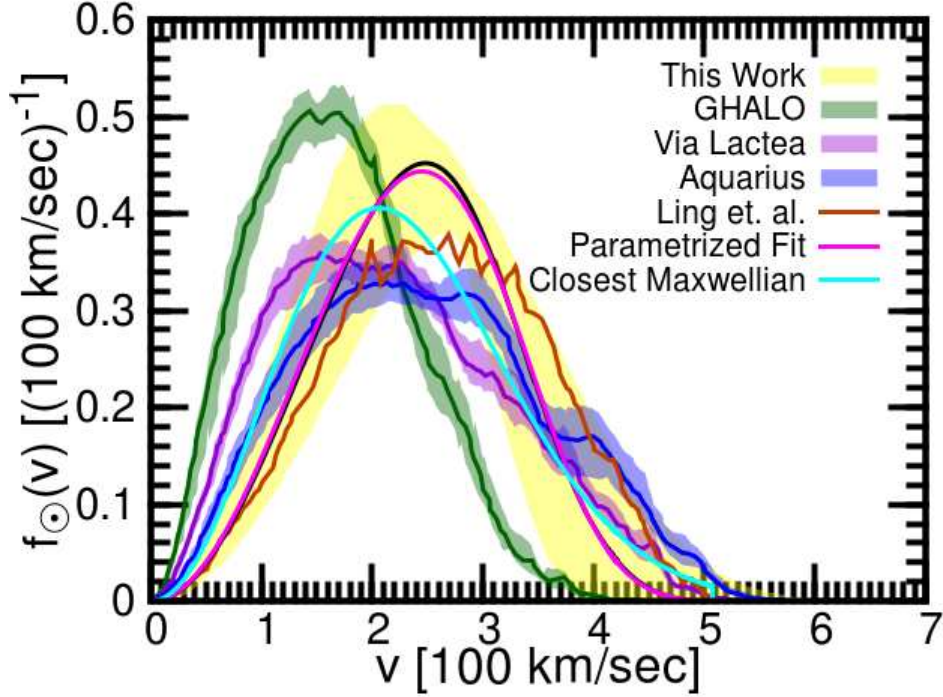


Figure 2.5: Same as Figure 2.4 along with comparison with results obtained from various numerical simulations [168].

Another important quantity is the pseudo phase space density, $Q(r)$, defined as $Q \equiv \rho / \langle v^2 \rangle^{3/2}$. $Q(r)$ has the same dimensions as the phase-space density, f , but it is not a true measure of it that is why it is referred to as pseudo or as a surrogate measure of phase-space density. Despite this, $Q(r)$ relates two moments of f which occur often in equations that describe equilibrium systems, and therefore simple relations between them are extremely useful when constructing dynamical models. The inset in Figure 2.6 shows our results for the pseudo phase space density, $Q(r)$, as a function of r , and its comparison with the power-law behavior predicted from simulation results [169]. Note the agreement with the power-law behavior at large distances but strong deviation from it at smaller Galactocentric radii, which we attribute to the effect of the visible matter. For a given DM density profile, the additional gravitational potential provided by the VM supports higher velocity dispersion of the DM particles, making Q smaller than that for the DM-only case.

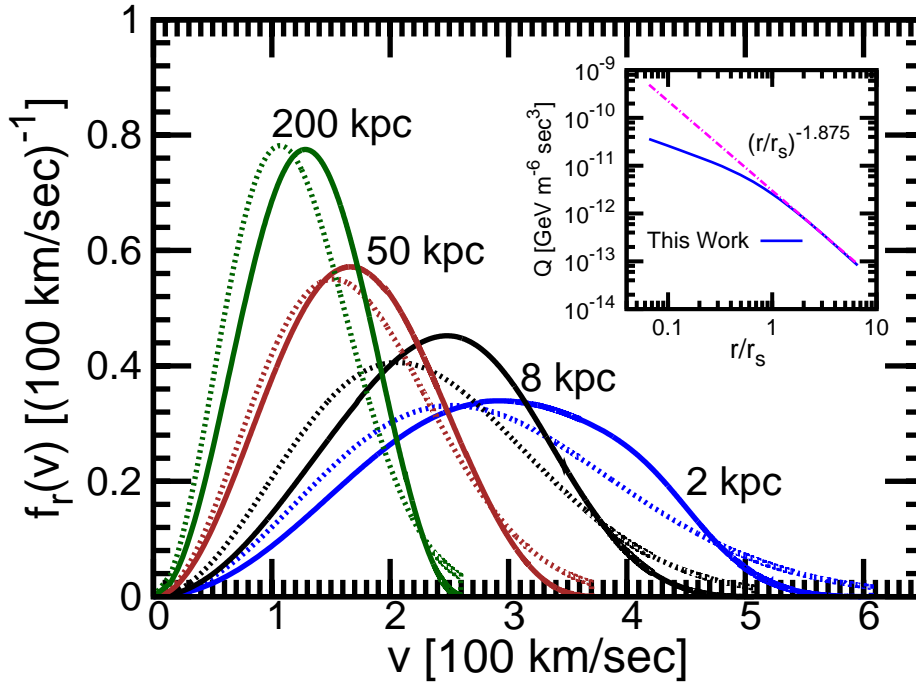


Figure 2.6: Normalized speed distribution of the DM particles at various Galactocentric radii (solid curves), corresponding to the most-likely set of values of the Galactic model parameters given in Table 2.1. The curves (dotted) for the corresponding best Maxwellian fit are also shown for comparison. The inset shows the pseudo-phase space density of DM, $Q \equiv \rho / \langle v^2 \rangle^{3/2}$, as a function of r .

2.5 Summary

To summarize, in this chapter we have attempted to derive the velocity distribution (assumed isotropic) of the dark matter particles in the Galaxy directly using the rotation curve data. We started from a simulation motivated density profile, namely NFW, and then inverted it using the Eddington's formalism to obtain the PSDF of the system. In this exercise, we have included the gravitational effect of the visible matter on the dark matter particles in a self-consistent manner. By performing the MCMC analysis using the Galactic rotation curve data the best-fit parameter values of the models are found. The main result of this chapter is that the derived VDF deviates significantly from the Maxwellian form customarily used in the standard halo model (SHM). This feature is observed not in just solar location but also at every other location in the Galaxy, as expected from simulations also. We have

also given a parametrised form of the non-Maxwellian VDF corresponding to the most likely values of the parameters of the model obtained from fit to the RC data. The derived best-fit local dark matter density comes out to be 0.2 GeV cm^{-3} which is lower than the standard value 0.3 GeV cm^{-3} mostly adopted in literature. This may have resulted from the fact that the local circular velocity influences the trend of the RC data itself which in turn affects the local dark matter density value. Higher the local circular velocity higher should be the local dark matter density. Here the local circular velocity at which the RC curve data is standardized is taken as 200 km s^{-1} for which we get a local dark matter density of 0.2 GeV cm^{-3} as compared to standard model density of 0.3 GeV cm^{-3} where the local circular velocity is taken as 220 km s^{-1} . This dependence of local dark matter density on Galactic constant namely the local circular velocity through the RC data is discussed in detail in Chapter IV. In this chapter we have further calculated other physically relevant quantities. The virial radius of the Galaxy is found to be $\sim 200 \text{ kpc}$ and the maximum velocity v_{max} which is important for the calculation of direct and indirect detection rates is self-consistently determined to be 516 km s^{-1} .

Chapter 3

Rotation Curve of Milky Way out to 200 kpc

3.1 Introduction

The circular velocity, $v_c(r) = \sqrt{GM(r)/r}$, of a test particle at a radial distance r from the center of a mass distribution gives a direct measure of the total gravitational mass, $M(r)$, contained within that radius. A measured profile of v_c as a function of r for a spiral galaxy, often simply called its Rotation Curve (RC), is therefore a direct probe of the spatial distribution of the total gravitating mass inside the galaxy including its dark matter (DM) content [137, 138, 139, 140, 141, 142]. In the previous chapter we have discussed how the RC of the Milky Way can be directly used to derive not only the local density of DM, but also the velocity distribution of the DM particles in the Galaxy [135], which are crucial for analyzing the results of both direct as well as indirect DM search experiments [2]; see also [170, 155, 146, 171].

In the previous chapter we have also described how the rotation curve (RC) can

be used to determine the values of the parameters of the dark matter and visible matter models adopted to describe the phase space distribution function of the dark matter. Therefore the RC plays an important role in determining the density and velocity distributions of the Galaxy which are basically two crucial astrophysical inputs for the analysis of DM detection experimental results. The derived RC depends on the choice of the Galactic constants (GCs), $\left[\frac{R_0}{\text{kpc}}, \frac{V_0}{\text{km s}^{-1}} \right]$, where R_0 and V_0 are the sun's distance from and circular rotation speed around the Galactic center, respectively. In the previous chapter the Rotation Curve data that had been used was standardized at a value of Galactic constants, $\left[\frac{R_0}{\text{kpc}}, \frac{V_0}{\text{km s}^{-1}} \right] = [8.0, 200]$. However, recent observations on Oort's constant [139] suggest value of the local circular velocity on the higher side around 244 km s^{-1} and the Galactocentric distance to be around 8.3 kpc . The RC however does not simply scale in a straight forward manner with the value of V_0 . The circular velocity of a test particle in the Galaxy is, of course, not a directly measured quantity. The RC of the Galaxy has to be derived from the kinematical as well as positional data for an appropriate set of tracer objects moving in the gravitational field of the Galaxy. Except in few cases, the full 3-D velocity information of the tracers is not available, and the RC has to be reconstructed from only the measured line-of-sight (*los*) velocity and positional information of various tracer objects in the Galaxy. One has to derive the RC for a given set of GCs starting from the kinematical data on the tracers, especially for the non disk tracers. In this chapter we aim to see how the RC trends depends on the choice of the GCc and also on the choice of the velocity anisotropy of the chosen tracer distribution, particularly in case of the non-disk tracers.

For the purpose of deriving DM density and velocity distributions using RC it is essential to derive the RC of the Galaxy to as large a Galactocentric distance as possible without referring to any specific model of the DM halo of the Galaxy. With this motivation, in this chapter we attempt to derive the RC of the Galaxy out to a large Galactocentric distances $\sim 200 \text{ kpc}$ using kinematical data on a variety of

tracer objects moving in the gravitational potential of the Galaxy, without assuming any model of the VM and DM halo of the Galaxy. We shall focus primarily on the RC in the non-disk region of the Galaxy. In Section 3.2 we present the Jeans equation formalism to calculate the RC beyond the disk region. In the next Section 3.3 we discuss about the non-disk tracers samples adopted and their density distributions and velocity dispersions. In Section 3.4 we present the RC profiles obtained for different choices of GC sets and tracer velocity anisotropy parameters and discuss the results. Finally, in Section 3.5 we summarize our methods and results obtained.

3.2 Rotation Curves beyond Disk region : The Jeans equation approach

For deriving the RC in the disk region of the Galaxy, one usually makes the reasonable assumption that the disk tracer objects move in circular orbits around the Galactic center. From the observed heliocentric los velocities, v_h , of the tracers and their position coordinates in the Galaxy, and with an assumed set of values of the Galactic Constants (GCs), $\left[\frac{R_0}{\text{kpc}}, \frac{V_0}{\text{km s}^{-1}} \right]$, that define the Local Standard of Rest (LSR) frame, and applying corrections for the peculiar motion of the sun with respect to the LSR, one can obtain the circular velocities around the Galactic center, v_c , in a fairly straightforward manner [172].

Observations on a variety of tracers such as HI regions, CO emission associated with HII regions, compact objects like Carbon stars (C stars), Cepheids, planetary nebulae (PNe), masers, and so on, have been used to derive the RC of the Galaxy in the disk region. Some recent compilations of RC data for the disk region of the Galaxy can be found, e.g., in [143, 173, 171].

In this thesis we mainly concentrate on the construction of the RC in region beyond

the Galactic disk and out to large Galactocentric distance of ~ 200 kpc. For detailed description of the RC in the disk region of the Galaxy see [143, 156].

To derive the RC in the outer regions of the Galaxy beyond the Galactic disk, one has to rely on distant tracers like Blue Horizontal Branch (BHB) stars, K Giant (KG) stars and relatively rare tracer objects like Globular Clusters (GCl), dwarf spheroidal (dSph) galaxies and so forth which populate the Milky Way's extended DM halo out to Galactocentric distances of several hundreds of kpc. Unlike the disk tracers, these non-disk tracers do not exhibit any systematic circular motion, and move about in the Galaxy along various different orbits. The standard approach then is to assume that the tracer population under consideration is isotropically distributed in the halo of the Galaxy and then use the Jeans equation [133] for spherical systems. The Jeans equation relates the circular velocity v_c at radius r to the number density and galactocentric radial as well as transverse velocity dispersions of the tracers at that radius and is given by [133],

$$v_c^2(r) = \frac{GM(r)}{r} = -\sigma_r^2 \left(\frac{d \ln n_{\text{tr}}}{d \ln r} + \frac{d \ln \sigma_r^2}{d \ln r} + 2\beta \right). \quad (3.1)$$

Here $r = (R_0^2 + r_h^2 - 2R_0 r_h \cos b \cos l)^{1/2}$ is the Galactocentric radial distance of a tracer (see Figure 3.1) and n_{tr} , σ_r and β are, respectively, the number density of the tracer population, their Galactocentric radial velocity dispersion, and the velocity anisotropy parameter, at r . Of course, in absence of full 3-D velocity information, with only the observed radial velocity dispersion available, the RC constructed using Jeans equation depends on the unknown velocity anisotropy parameter $\beta \equiv 1 - \sigma_t^2/2\sigma_r^2$ (σ_r and σ_t being the radial and transverse velocity dispersions of the tracers, respectively).

The Jeans equation approach has been used in several recent studies to extend the RC of the Galaxy to distances beyond the extent of the Galaxy's stellar disk.

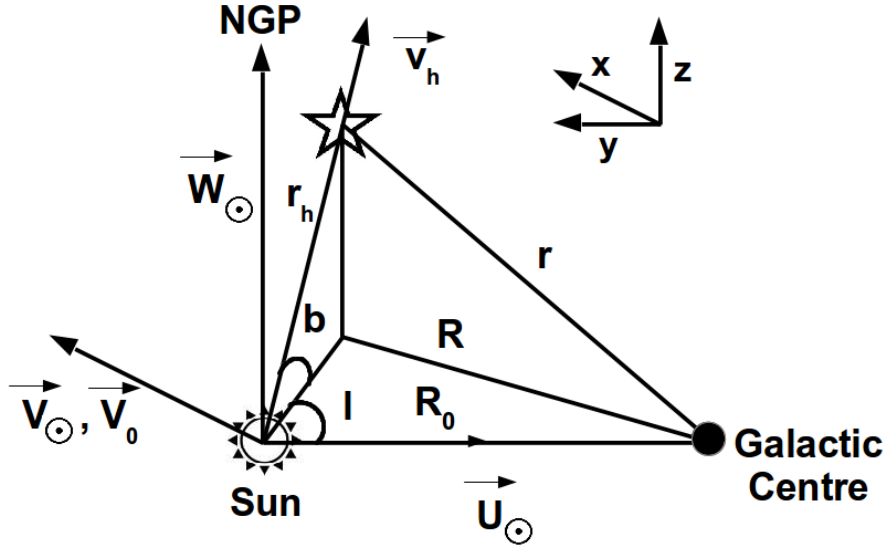


Figure 3.1: Schematic diagram showing the coordinate system, velocity and distance notations used in this chapter.

Accurate measurements of *los* velocities of a sample of 2401 BHB stars drawn from SDSS DR6 [174] were used by [175] to derive the RC of the Galaxy to ~ 60 kpc for two constant (r -independent) values of β , namely $\beta = 0$ (isotropic velocity distribution) and $\beta = 0.37$, the latter derived from results of numerical simulations. More recently, the Jeans equation has also been employed, together with certain analytical models of the phase-space distribution function of the tracer population, to construct the RC of the Galaxy to various distances of ~ 25 to ~ 80 kpc [176, 177, 178].

A crucial ingredient in the derivation of the distant RC using Jeans equation is the measured radial velocity dispersion of the tracers as a function of their Galactocentric distance r . An important finding in this regard is the result, first shown in [179], that the radial velocity dispersion remains almost constant at a value of $\sim 120 \text{ km s}^{-1}$ out to ~ 30 kpc and then steadily *declines* down to a value of $\sim 50 \text{ km s}^{-1}$ at $r \sim 120$ kpc. Ref. [179] used a heterogeneous sample of about 240 halo objects consisting of field blue horizontal branch stars, red giant stars, globular clusters and distant satellite galaxies. Similar trend of the radial velocity disper-

sion profile has been found in several subsequent studies using different samples of tracers, e.g., by [175, 176, 177, 180, 181], and most recently in large cosmological simulations by [182].

Here we consider a combination of a variety of non-disk tracers to construct the RC of the Galaxy beyond the disk region out to ~ 200 kpc. We perform a detailed analysis of the dependence of the RC on the choice of the GCs and also the dependence on the anisotropy parameter β of the non-disk tracers. It is found that, while the RC in the disk region is significantly influenced by the choice of the GCs, the dominant uncertainty in the RC at large distances beyond the stellar disk comes from the uncertainty in the value of β . Since currently not much reliable observational information on β is available, we calculate the circular velocities using Jeans equation with the velocity anisotropy β of the tracers taken as (a) a radially constant free parameter varying over a possible range of values from $\beta = 0$ (corresponding to complete isotropy of the tracers' orbits) to $\beta = 1$ (corresponding to completely radial orbits of the tracers), (b) a radially varying β of the Osipkov-Merritt (OM) form [133] given by $\beta(r) = (1 + r_a^2/r^2)^{-1}$, with r_a the ‘‘anisotropy radius’’, and (c) a radial profile of β obtained from a recent large high resolution hydrodynamical simulations of formation of late-type spirals like our Galaxy [182].

3.3 Non-Disk tracer samples

We have chosen two independent classes of non-disk stellar tracers, namely, a sample of 4985 Blue Horizontal Branch (BHB) stars from SDSS-DR8 compiled by [183] and a set of 4781 K Giant (KG) stars from SDSS-DR9 [184]. These two samples allow us to probe the Galactic halo up to a Galactocentric distance of ~ 100 kpc. In order to reach out further we consider an additional heterogeneous (Hg) sample of 430 objects comprising of 143 Globular Clusters (GC1) [185], 118 red halo giants (RHG)

[186], 108 field blue horizontal branch (FHB) stars [187], 38 RR-Lyrae stars (RRL) [188], and 23 dwarf spheroidals (dSph) [189]. To ensure that the sample comprises of only halo objects, we applied a cut on the z and R coordinates of the tracers, leaving out objects with $r < 25$ kpc in all the non-disk tracer samples mentioned above. After these cuts, we are left with a “BHB” sample of 1457 blue horizontal branch stars, a “KG” sample of 2227 K-giant stars and a “Hg” sample of 65 objects comprising of 16 GCs, 28 FHB stars and 21 dSphs, with which we shall construct our RC for the non-disk region. The last sample allows us to extend the RC to a Galactocentric distance of 190 kpc, the mean r of the objects in the furthest radial bin in the Hg sample. The spatial distributions of the three final non-disk tracer samples (after position cuts mentioned above) in terms of x - z , y - z and x - y scatter plots are shown in Figure 3.2).

The number density of the tracers, n_{tr} , appearing in the Jeans equation (3.1) is estimated in the following way. We radially bin the objects in a given sample and estimate the tracer density from the star counts in the annular volume of each bin and assign it at the mean radius of the objects contained within that bin. In order to ensure a reasonably good number of objects per bin we adopt a variable bin size increasing with distance. For the BHB sample, a uniform bin size of 2 kpc is used over its entire range of r from 25 to 55 kpc. For the KG samples, the bin widths are 2 kpc for $25 \text{ kpc} < r \leq 55 \text{ kpc}$ and 4 kpc for $55 \text{ kpc} < r \leq 103 \text{ kpc}$; objects with $r > 103 \text{ kpc}$ (up to 110 kpc) are all placed in one single bin. For the Hg sample, because of the relatively small total number (65) of objects, we adopt the following optimal, “object wise” binning in increasing order of the galactocentric distance r of the objects: the first 6 radial bins contain 8 objects in each bin; the next 2 bins contain 6 objects in each bin; and, finally, the remaining 5 objects are placed in one single bin. Uncertainties in the number density estimates are obtained from Poissonian errors on the tracer counts in each bin.

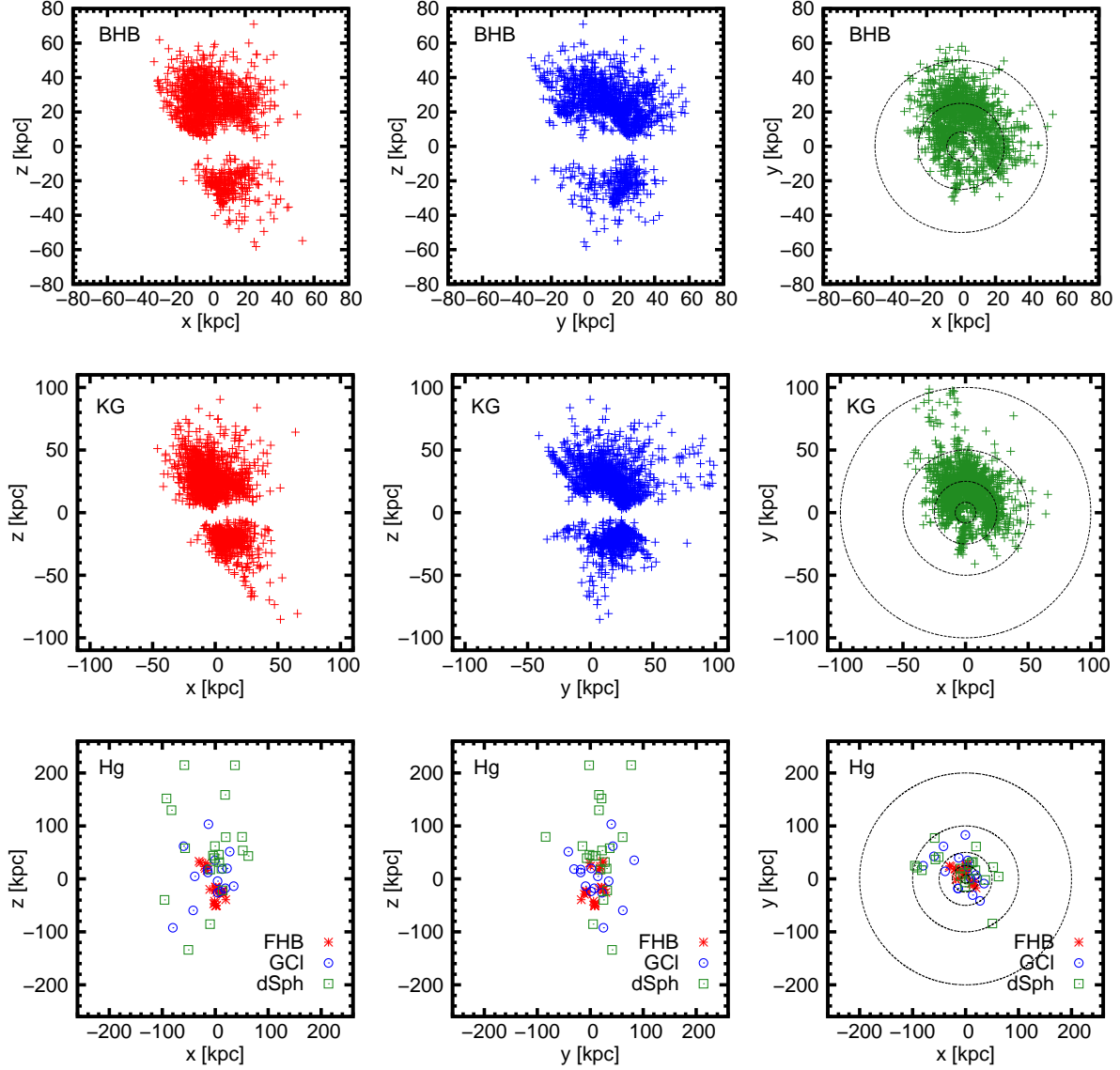


Figure 3.2: x - z , y - z and x - y scatter plots (after removing objects with $r < 25$ kpc; see text) for the three samples of non-disk tracer objects considered in this chapter, namely, (1) the “BHB” sample, a set of 1457 blue horizontal branch stars from the compilation of [183], (2) the “KG” sample, a set of 2227 K-Giant stars from the compilation of [184], and (3) the “Hg” sample, a heterogeneous set of 65 objects comprising of 16 Globular Clusters (GCl) from [185], 28 field blue horizontal branch (FHB) stars from [187], and 21 dwarf spheroidals (dSph) from [189], for $R_0 = 8.3$ kpc with the sun located at $(x = 0, y = R_0, z = 0)$.

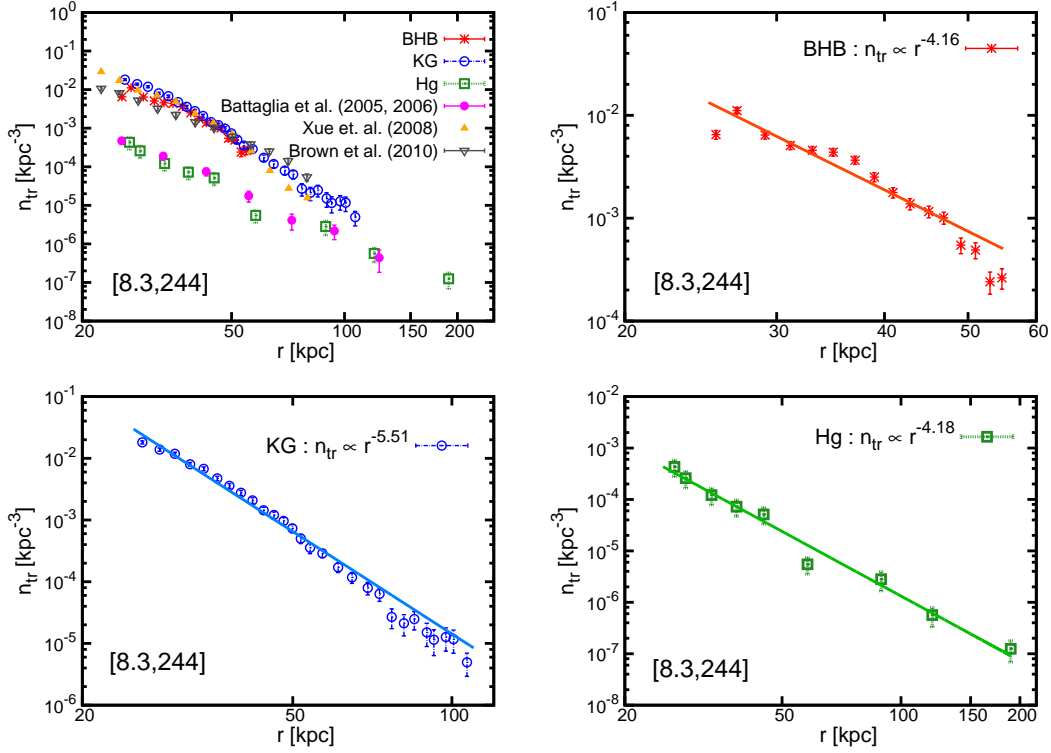


Figure 3.3: The tracer number density, n_{tr} , for the three non-disk tracer samples considered in this chapter (see text and Figure 3.2 for details and source references for the samples). The top left panel shows, for comparison, the tracer densities obtained in some earlier studies [179, 175, 180] which used different tracer samples. The other three panels show the best power law fits to the radial profiles of n_{tr} for the three non-disk samples. The GC set used is $\left[\frac{R_0}{\text{kpc}}, \frac{V_0}{\text{km s}^{-1}}\right] = [8.3, 244]$.

The resulting density estimates for the three samples mentioned above with the GCs set $\left[\frac{R_0}{\text{kpc}}, \frac{V_0}{\text{km s}^{-1}}\right] = [8.3, 244]$ are shown in Figure 3.3, where for comparison (see the top left panel of Figure 3.3) the tracer densities from some earlier studies that used different tracer samples are also shown. These results are seen to be in reasonably good agreement with those obtained in the previous studies.

It is convenient to use an analytical form of the density distribution of tracers in order to solve the Jeans equation. Therefore, we perform power-law fits ($n_{\text{tr}}(r) \propto r^{-\gamma}$) to the radial profile of the tracer number density for each of the three samples separately. The resulting best power-law fits are also shown in Figure 3.3. The values of the parameters of the best power-law fit for each tracer sample are given

in Table 3.1. Within each sample, there is no significant difference in the values of n_{tr} for the three different sets of GCs, as also seen from the values of the power-law fit parameters given in Table 3.1.

Next, we have to calculate the Galactocentric radial velocity dispersion, σ_r , that appears in the Jeans equation (3.1), for our non-disk samples. To do this we first transform the observed heliocentric los velocity, v_h , of each individual tracer object to v_{GSR} , the velocity that would be measured in the Galactic Standard of Rest (GSR) frame. This is easily done by correcting for the circular motion of the LSR (V_0) and solar peculiar motion with respect to LSR, $(U_\odot, V_\odot, W_\odot)$ (see Figure 3.1) as given below,

$$\begin{aligned} v_{\text{GSR}} = & v_h + U_\odot \cos b \cos l + V_\odot \cos b \sin l \\ & + W_\odot \sin b + V_0 \cos b \sin l. \end{aligned} \quad (3.2)$$

For large samples like the BHB and KG stars described above, we calculate the v_{GSR} for all the individual tracers in the same radial bins as used in the estimation of the tracers' number density described above, calculate their dispersion, σ_{GSR} , and assign it to the mean radius of all the tracers contained within that bin. The corresponding uncertainty, $\Delta\sigma_{\text{GSR}}$, in our estimate of σ_{GSR} in each bin is calculated by using the standard formula $\Delta\sigma_{\text{GSR}} = \sqrt{1/[2(N-1)]}\sigma_{\text{GSR}}$ [190, 191, 192], where N is the number of objects in the bin.

For the Hg sample, however, owing to its small size, we follow a different method, similar to that used in [179], for calculating the σ_{GSR} and its uncertainty in each radial bin: we randomly generate a sample of 10,000 mock values of v_h for each tracer object in a radial bin using a Gaussian centered at the observed value of v_h and a width of typically $\sim (10 - 20)\%$ of this v_h value. We then transform these 10,000 v_h values for each tracer in the bin to get the corresponding 10,000 values

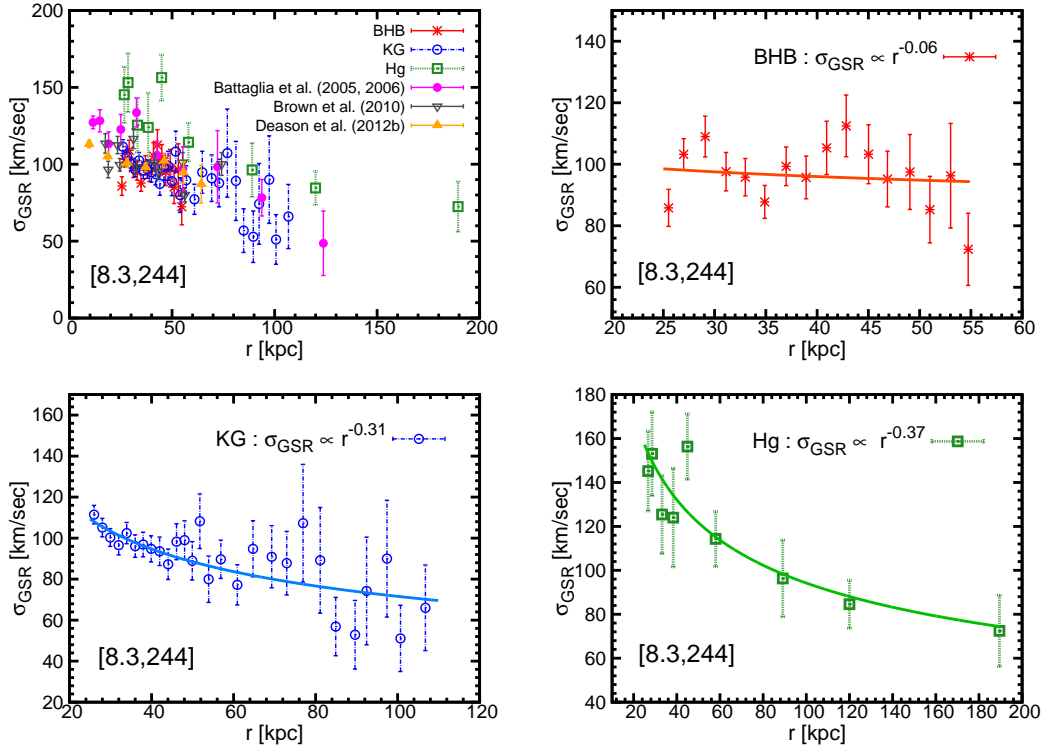


Figure 3.4: The GSR frame los velocity dispersion of the tracers, σ_{GSR} , for the three non-disk tracer samples considered in this chapter (see text and Figure 3.2 for details and source references for the samples). The top left panel also shows, for comparison, the σ_{GSR} obtained in some earlier studies [179, 180, 181] which used different tracer samples. The other three panels show the best power-law fits to the radial profiles of σ_{GSR} for the three non-disk samples. The GC set used is $\left[\frac{R_0}{\text{kpc}}, \frac{V_0}{\text{km s}^{-1}} \right] = [8.3, 244]$.

of v_{GSR} using equation (3.2), and calculate the associated dispersions σ_{GSR} in that bin. We assign the mean value of the σ_{GSR} values for all the objects in a given bin to the mean radius of all the objects in the bin. The corresponding uncertainty in σ_{GSR} is taken to be the r.m.s. deviation of the σ_{GSR} values in that bin.

The results for σ_{GSR} for the three tracer samples are shown in Figure 3.4 in which we also show for comparison (see the top left panel of Figure 3.4) the σ_{GSR} values obtained in some earlier studies using different samples, which, again, are seen to be in reasonably good agreement with our results.

For σ_{GSR} also we use fitted forms in order to solve the Jean's equation in a conve-

nient manner. The other three panels of Figure 3.4 show the best power-law fits ($\sigma_{\text{GSR}}(r) \propto r^{-\alpha}$) to the radial profiles of σ_{GSR} for each of the three non-disk samples. The values of the parameters of the best power-law fits for the three tracer samples are given in Table 3.1. Again, as in the case of n_{tr} , the effect of variation of the Galactic Constants on σ_{GSR} is negligible.

Finally, the Galactocentric radial velocity dispersion, σ_r , can be obtained from σ_{GSR} by using the relation [179]

$$\sigma_r = \frac{\sigma_{\text{GSR}}}{\sqrt{1 - \beta H(r)}}, \quad (3.3)$$

where

$$H(r) = \frac{r^2 + R_0^2}{4r^2} - \frac{(r^2 - R_0^2)^2}{8r^3 R_0} \ln \frac{r + R_0}{r - R_0}, \quad (r > R_0) \quad (3.4)$$

and β is the velocity anisotropy of the tracers defined earlier. Equation (3.3) is derived by decomposing the v_{GSR} 's into their Galactocentric radial and transverse components and taking the averages of the squares of the velocity components.¹

The last quantity that remains to be specified before we can solve the Jeans equation (3.1) is the velocity anisotropy parameter, β , of the tracers. There is not much definite observational information available on the value of β of the tracers because of the lack of availability of proper motion measurements on sufficiently large number of tracer objects. In general β can be a function of r . A recent maximum likelihood analysis [177] of radial velocity data of a large sample of halo stars, performed within the context of a model for the (in general anisotropic) velocity distribution function of the halo stars, indicates the stellar velocity anisotropy being radially biased with a value of $\beta \sim 0.5$ for r from ~ 16 kpc up to $r \sim 48$ kpc. This is also indicated by the recent results from the large numerical simulation study of [182], which finds the velocity distribution of the Galaxy's stellar population at large r

¹Note that equation (3) given in the 2005 paper of [179] is incorrect. The correct equation, same as equation (3.3) above, is given in the 2006 (Erratum) paper of [179] and also in [193].

to be radially biased ($\beta > 0$) with stellar orbits tending to purely radial ($\beta \rightarrow 1$) at $r \gtrsim 100$ kpc. Based on these considerations, to explore various possibilities for β , here we have calculated the RCs for (a) three representative constant values of β , namely, $\beta = 0$ (isotropic), 0.5 (mildly radially biased anisotropy), and 1 (fully radially anisotropic), (b) a radially varying β of the Osipkov-Merrit (OM) form [133] given by $\beta(r) = (1 + r_a^2/r^2)^{-1}$, r_a being the “anisotropy radius”, and (c) a radial profile of β obtained from the recent large high resolution hydrodynamical simulations done by [182]. In principle, β and its radial profile may be different for different tracer samples. But since currently no reliable measurements of β for the different samples extending to large Galactocentric distances are available, any choice of different β for different samples would be necessarily arbitrary. For simplicity, therefore, we assume the same values of β and its radial profile for our three tracer samples.

3.4 Rotation Curves from different tracer samples and the combined Grand Rotation Curve

With n_{tr} , σ_r and β specified in the previous section, we can now proceed to solve the Jeans equation (3.1) to obtain the v_c profiles for the three different tracer samples described above. For each tracer sample we calculate the v_c 's in the same radial bins as used in calculating the n_{tr} 's and σ_{GSR} 's, and the best-fit power-law forms of n_{tr} and σ_{GSR} described above are used for calculating the radial derivatives appearing in the Jeans equation (3.1). The corresponding 1σ error, Δv_c , on v_c within each radial bin is calculated from those of n_{tr} and σ_{GSR} in the bin by standard quadrature.

The resulting RCs for the three tracer samples are shown in Figure 3.5. As clear from the left panels of Figure 3.5 the RCs for different choices of GCs almost overlap, thus indicating that the RC at large Galactocentric distances beyond a few tens of kpc is

$\left[\frac{R_0}{\text{kpc}}, \frac{V_0}{\text{km s}^{-1}} \right]$	Number densities and radial velocity dispersions of non-disk tracers			
	$n_{\text{tr}} = n_0 \left(\frac{r}{50 \text{ kpc}} \right)^{-\gamma}, \sigma_{\text{GSR}} = \sigma_0 \left(\frac{r}{50 \text{ kpc}} \right)^{-\alpha}$			
	$\frac{n_0}{\text{kpc}^3}$	γ	$\frac{\sigma_0}{\text{km s}^{-1}}$	α
	BHB			
[8.3, 244]	7.51×10^{-4}	4.16	93.0	0.06
[8.5, 220]	7.66×10^{-4}	4.15	94.45	0.07
[8.0, 200]	7.45×10^{-4}	4.17	93.58	0.05
	KG			
[8.3, 244]	6.57×10^{-4}	5.51	86.75	0.31
[8.5, 220]	6.53×10^{-4}	5.51	88.23	0.30
[8.0, 200]	6.40×10^{-4}	5.51	87.89	0.29
	Hg			
[8.3, 244]	2.37×10^{-5}	4.18	121.21	0.37
[8.5, 220]	2.39×10^{-5}	4.18	117.51	0.40
[8.0, 200]	2.38×10^{-5}	4.17	115.34	0.42

Table 3.1: Best-fit parameter values for power-law fits to the radial profiles of the number density, n_{tr} , and the Galactic Standard of Rest (GSR) frame *los* velocity dispersion, σ_{GSR} , of the tracers for the three non-disk tracer samples considered in this chapter (see text and Figure 3.2 for details and source references for the samples). The parameter values are given for three different sets of values of the GCs, $\left[\frac{R_0}{\text{kpc}}, \frac{V_0}{\text{km s}^{-1}} \right]$.

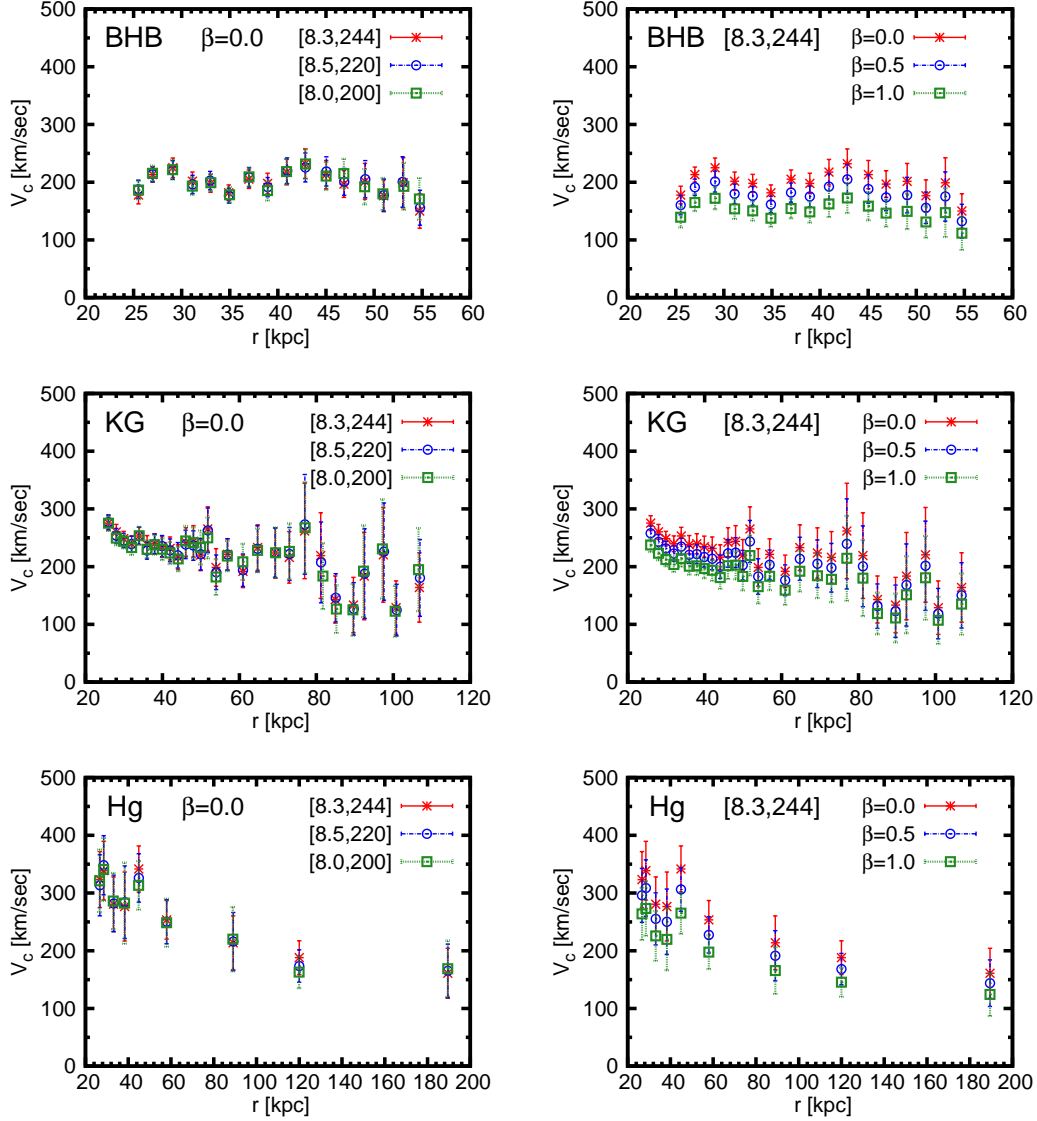


Figure 3.5: Circular velocities with their 1σ error bars for the three different non-disk tracer samples used here in Figure 3.2. The left panels are for tracer velocity anisotropy $\beta = 0$ and three different sets of values of the Galactic constants, $\left[\frac{R_0}{\text{kpc}}, \frac{V_0}{\text{km s}^{-1}}\right]$, as indicated, whereas the right panels show the results for three different constant (r -independent) values of $\beta = 0, 0.5$ and 1 , with $\left[\frac{R_0}{\text{kpc}}, \frac{V_0}{\text{km s}^{-1}}\right] = [8.3, 244]$.

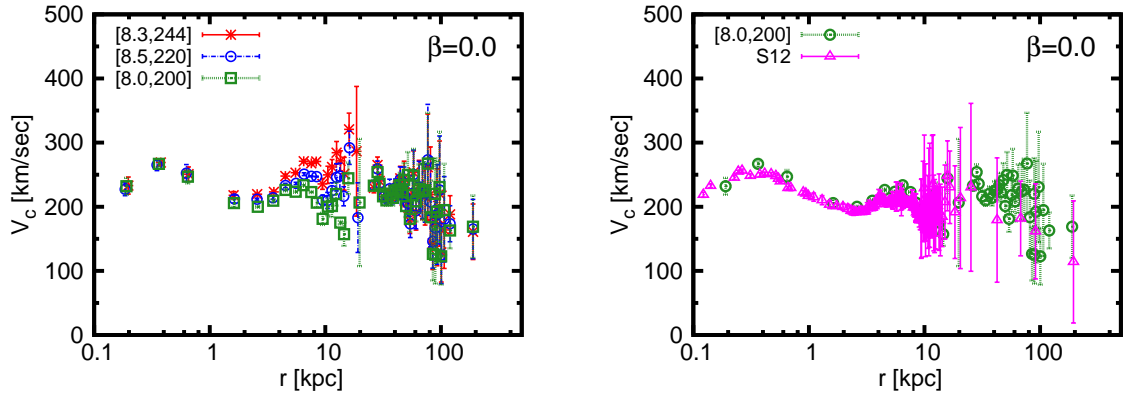


Figure 3.6: Left: Rotation curve of the Galaxy for three different sets of values of the Galactic constants $\left[\frac{R_0}{\text{kpc}}, \frac{V_0}{\text{km s}^{-1}}\right]$ as indicated and non-disk tracers' velocity anisotropy parameter $\beta = 0$. The data points and their 1σ error bars shown here are obtained by weighted averaging over the combined v_c data obtained from different disk and non-disk tracer samples. Right: Rotation curve of the Galaxy for $\left[\frac{R_0}{\text{kpc}}, \frac{V_0}{\text{km s}^{-1}}\right] = [8.0, 200]$ and non-disk tracers' velocity anisotropy parameter $\beta = 0$ compared with that obtained by [140] (S12).

fairly insensitive to the precise values of the GCs. Instead, the main uncertainty in the RC comes from the unknown value of the tracers' velocity anisotropy parameter β , as evident from the right panels of Figure 3.5. As expected, the lowest rotation speeds obtain for the most radially biased velocity anisotropy ($\beta = 1$).

We now combine the rotation curves obtained from disk as given in Ref. [143] and non-disk tracers (Figure 3.5) to construct the rotation curve of the Galaxy up to ~ 200 kpc. For the disk region ($r < 25$ kpc) we have taken the data from [143]. For the non-disk region ($r \geq 25$ kpc), we combine the v_c data from Figure 3.5 for the three tracer samples in every 2 kpc radial bins and calculate the resulting mean circular speed (v_c) and its 1σ uncertainty (Δv_c) within a bin by weighted averaging [194] using,

$$v_c = \frac{\sum_i w_i V_{c,i}}{\sum_i w_i}, \quad \text{and} \quad \Delta v_c = \sqrt{\frac{1}{\sum_i w_i}}, \quad (3.5)$$

with $w_i = 1/(\Delta V_{c,i})^2$, where $V_{c,i}$ and $\Delta V_{c,i}$ are the v_c value and its 1σ error, respectively, of the i -th data point within the bin.

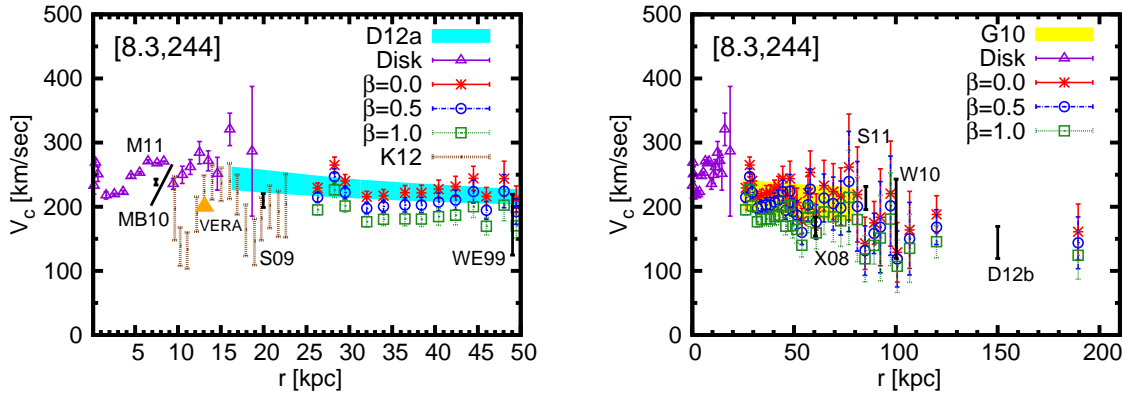


Figure 3.7: Rotation Curve for $\left[\frac{R_0}{\text{kpc}}, \frac{V_0}{\text{km s}^{-1}}\right] = [8.3, 244]$ and various values of β . The shaded bands marked D12a and G10 in the left and right panels, respectively, represent the RCs and their uncertainty bands obtained earlier by [177] (D12a) (up to $r \sim 50$ kpc) and [176] (G10) (up to $r \sim 80$ kpc), respectively. In addition, estimates of circular velocities at certain specific values of r obtained from various independent considerations by [178] (K12), [195] (M11), [196] (MB10), [197] (VERA), [173] (S09), [198] (WE99), [175] (X08), [199] (S11), [200] (W10), and [181] (D12b) are shown for comparison.

The resulting rotation curves for $\beta = 0$ and three sets of values of the GCs are shown in Figure 3.6, and those for different values of β , for one particular set of GCs, $\left[\frac{R_0}{\text{kpc}}, \frac{V_0}{\text{km s}^{-1}}\right] = [8.3, 244]$, are shown in Figure 3.7. For comparison, we also present in Figure 3.7 estimates of circular velocities at specific values of r obtained from a variety of independent considerations in some earlier studies by various authors.

The β dependence of the radial profile of the cumulative mass, $M(r) = rv_c^2(r)/G$, is shown in Figure 3.8. Again, estimates of $M(r)$ from various independent considerations and given at certain specific values of r in some earlier works, are also shown in Figure 3.8 for comparison. Note that the lowest mass of the Galaxy corresponds to $\beta = 1$, which allows us to set a lower limit on the mass of the Galaxy, $M(\sim 200 \text{ kpc}) \geq (6.8 \pm 4.1) \times 10^{11} M_\odot$.

In Figure 3.10 we present the full rotation curve of the Galaxy out to ~ 200 kpc for $\left[\frac{R_0}{\text{kpc}}, \frac{V_0}{\text{km s}^{-1}}\right] = [8.3, 244]$ and for a radial profile of the non-disk tracers' velocity anisotropy parameter β of the OM form, $\beta(r) = (1 + r_a^2/r^2)^{-1}$, for two different

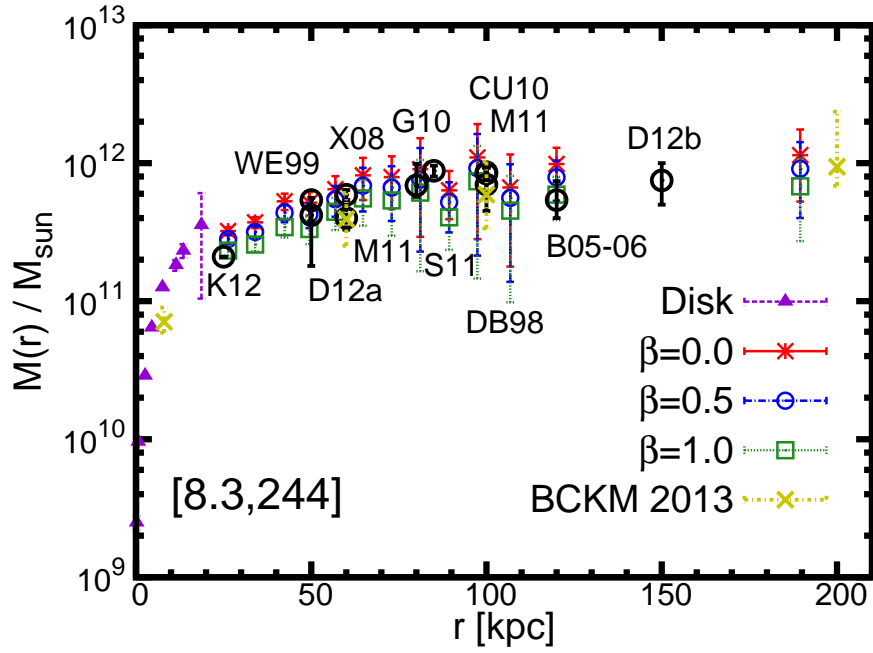


Figure 3.8: The mass, $M(r) = rv_c^2(r)/G$, within r , as a function of r , obtained from the RCs shown in Figure 3.7 for $\left[\frac{R_0}{\text{kpc}}, \frac{V_0}{\text{km s}^{-1}}\right] = [8.3, 244]$ and various values of the tracers' velocity anisotropy parameter β . Estimates of $M(r)$ at certain specific values of r obtained from various independent considerations in some earlier works, namely, [178] (K12), [198] (WE99), [177] (D12a), [175] (X08), [195] (M11), [176] (G10), [199] (S11), [201] (CU10), [202] (DB98), [179] (B05-06), [181] (D12b), and [135] (BCKM 2013), are shown for comparison.

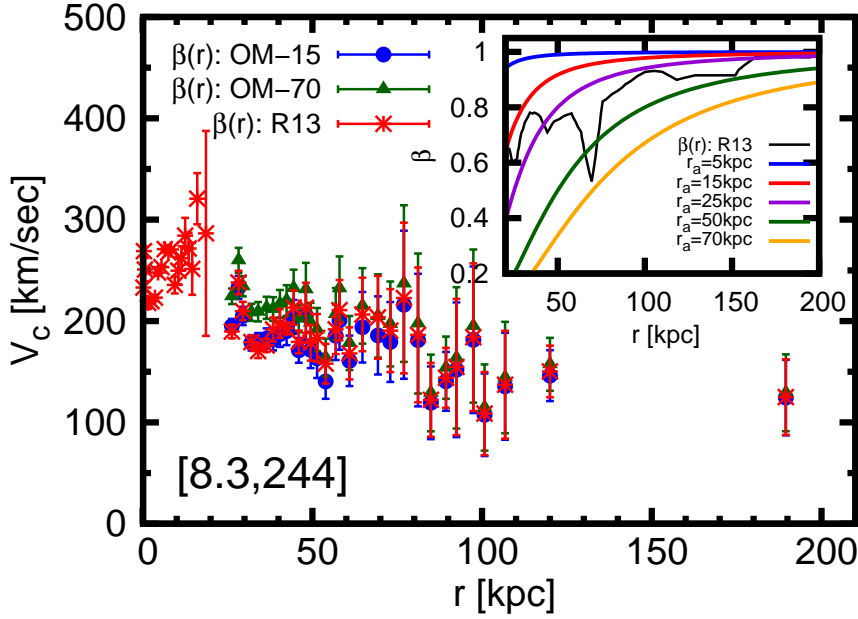


Figure 3.9: Rotation curve of the Milky Way to ~ 200 kpc for $\left[\frac{R_0}{\text{kpc}}, \frac{V_0}{\text{km s}^{-1}}\right] = [8.3, 244]$ and for a radial profile of the non-disk tracers’ velocity anisotropy parameter β of the Osipkov-Merritt (OM) form, $\beta(r) = (1 + r_a^2/r^2)^{-1}$, with two values of the “anisotropy radius” $r_a = 15$ kpc (OM-15) and 70 kpc (OM-70). The RC data generated with a radial profile of β derived from Figure 2 of [182] (R13) (data points marked $\beta(r)$:R13) are also shown for comparison. The inset shows the OM β profile for various values of r_a together with the β profile from Figure 2 of R13.

values of $r_a = 15$ kpc and 70 kpc. In addition, we show the RC generated with a β profile extracted from Figure 2 of [182] with the corresponding numerical data in tabular form given in Table 3.2. The inset in the left panel of Figure 3.10 shows the OM β profile for various values of r_a as well as the β profile obtained in [182]. The latter is seen to roughly follow the OM form and is reasonably well bracketed within OM β profiles with $r_a = 15$ kpc and $r_a = 70$ kpc. In Figure 3.10 we also plot the circular velocity data from terminal velocities and rotation curve fits for the Burkert and NFW models of the DM halo of the Galaxy given in [141] (up to ~ 100 kpc) in comparison with the RC generated with the β profile of [182].

A noticeable feature of the rotation curve, irrespective of the velocity anisotropy of the tracer objects, is its clearly declining nature beyond about ~ 60 kpc, as would be expected of an effectively finite size of the dark matter halo of the Galaxy. It is to be

r (kpc)	v_c (km s ⁻¹)	Δv_c (km s ⁻¹)	r (kpc)	v_c (km s ⁻¹)	Δv_c (km s ⁻¹)
0.20	233.0	13.32	38.41	191.57	11.73
0.38	268.92	4.67	40.42	197.59	14.12
0.66	250.75	11.35	42.40	192.79	5.92
1.61	217.83	5.81	44.49	213.22	17.17
2.57	219.58	1.48	45.99	179.39	11.23
3.59	223.11	2.43	48.06	213.03	24.72
4.51	247.88	2.99	49.49	178.57	17.63
5.53	253.14	1.69	51.39	183.31	23.58
6.50	270.95	2.19	53.89	157.89	19.57
7.56	267.80	0.96	56.89	191.76	24.35
8.34	270.52	0.66	57.98	210.72	29.81
9.45	235.58	8.44	60.92	168.02	25.67
10.50	249.72	13.44	64.73	206.47	36.27
11.44	261.96	11.71	69.31	203.62	40.89
12.51	284.30	17.50	72.96	190.53	40.98
13.53	271.54	15.57	76.95	222.72	74.37
14.59	251.43	25.60	81.13	186.29	66.53
16.05	320.70	25.27	84.90	122.25	36.46
18.64	286.46	101.18	89.35	143.95	29.49
26.30	189.64	6.74	92.44	154.66	67.23
28.26	237.99	11.54	97.41	184.0	72.86
29.51	209.82	9.16	100.72	108.68	40.99
32.04	179.14	6.65	106.77	137.15	53.17
33.99	170.37	6.93	119.98	150.18	25.46
36.49	175.92	6.62	189.49	125.01	37.32

Table 3.2: The circular velocity, V_c , and its 1- σ error, Δv_c , for various values of the Galactocentric distance, r , for a radial profile of the non-disk tracers' velocity anisotropy parameter β derived from Figure 2 of [182], with $\left[\frac{R_0}{\text{kpc}}, \frac{V_0}{\text{km s}^{-1}} \right] = [8.3, 244]$.

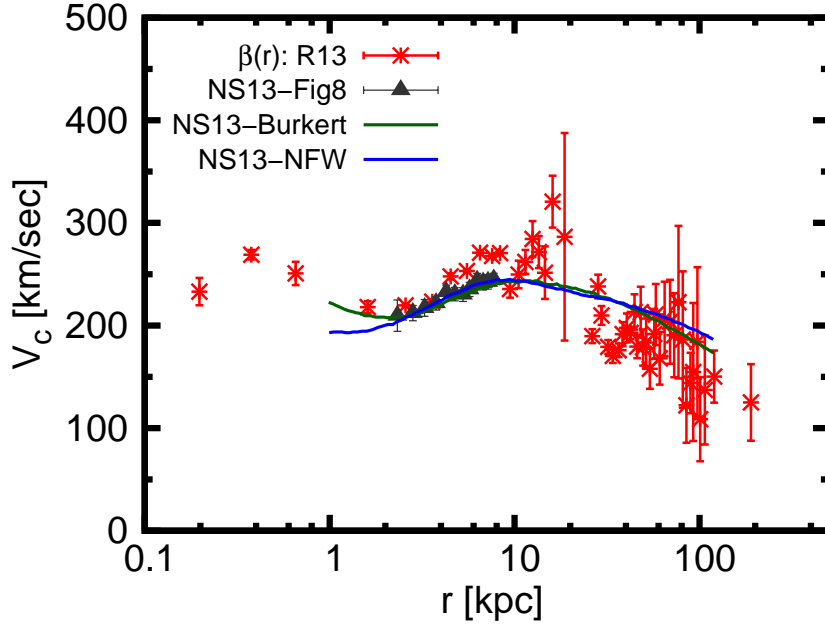


Figure 3.10: Rotation curve of the Milky Way to ~ 200 kpc for $\left[\frac{R_0}{\text{kpc}}, \frac{V_0}{\text{km s}^{-1}}\right] = [8.3, 244]$ and for β derived from Figure 2 of [182] (R13) in log scale and compared with the circular velocity data from terminal velocities (NS13-Fig8) and rotation curve fits for Burkert (NS13-Burkert) and NFW (NS13-NFW) models from [141]. The numerical data for $\beta(r)$:R13 are given in Table 3.2.

emphasized that, for any given β , the rotation curve and mass profile of the Galaxy shown in Figures 3.7 and 3.8, respectively, are based entirely on observational data, and are obtained without making any models of the mass distributions of the various components (the bulge, disk and dark matter halo) of the Galaxy.

3.5 Summary

In this chapter, we have constructed the rotation curve (RC) of the Galaxy beyond the disk region out to ~ 200 kpc by using kinematical data on a variety of non-disk objects that trace the gravitational potential of the Galaxy, without assuming any theoretical models of the visible and dark matter components of the Galaxy. We have studied the dependence of the RC on the choice of the Galactic constants (GCs) and also studied the dependence on the velocity anisotropy parameter β of

the non-disk tracers. The RC in the disk region depends significantly on the choice of values of the GCs but the rotation curve at large distances beyond the stellar disk, however, depends more significantly on the parameter β than on the values of the GCs. In general, the mean RC is found to steadily decline beyond $r \sim 60$ kpc, irrespective of the value of β . At any given Galactocentric distance r , the circular speed is lower for larger values of β . Considering that the largest allowed value of β is unity (complete radial anisotropy), this allows us to set a model-independent lower limit on the total mass of the Galaxy, giving $M(\lesssim 200 \text{ kpc}) \geq (6.8 \pm 4.1) \times 10^{11} M_{\odot}$. It is also noted that recent results from high resolution hydrodynamical simulations of formation of galaxies like Milky Way [182] indicate an increasingly radially biased velocity ellipsoid of the Galaxy's stellar population at large distances, with stellar orbits tending to be almost purely radial ($\beta \rightarrow 1$) beyond ~ 100 kpc. This implies that the above lower limit on the Galaxy's mass (obtained from our results with $\beta = 1$) may in fact be a good estimate of the actual mass of the Galaxy out to ~ 200 kpc. The RC derived here will be used in Chapter IV to study the phase space structure of the DM halo of the Galaxy.

Chapter 4

Velocity anisotropy of Dark

Matter : Michie Model

4.1 Introduction

The dynamics of the dark matter (DM) particles in our Galaxy is not very well-known. There are numerous attempts and methodologies adopted in literature to find the DM density distribution and velocity distribution specifically at solar location as these are the main astrophysical inputs that go into the calculation of the possible event rate at different dark matter detection experiments (both direct and indirect). The DM particles being mainly collisionless they can be assumed to satisfy the Collisionless Boltzmann Equation(CBE). Therefore, in most of the cases the Phase Space Distribution function (PSDF) of DM particles is described by an isothermal model which is a solution of CBE [133, 144]. In Chapter II, we have described the Isothermal model or the so called “Standard Halo Model” (SHM) which uses the isotropic Maxwellian velocity distribution. But SHM has its own severe drawbacks, specifically to note that it is not finite in configuration space which results into an

unbound mass.

The phase space distribution functions provides us with the most general and complete way of statistical description of dark matter halos. Our knowledge on the PSDF is still being improved, mostly due to numerical experiments. In the last few years cosmological simulations have revealed increasingly detailed features of phase-space structure of DM halos. These also extract information about the velocity anisotropy. It has been demonstrated that the outer parts of the halos exhibit more radially anisotropic trajectories than the halo centre [203, 204, 205, 206, 207].

There are previous works in literature [208, 209, 210, 211, 212, 213, 214, 215, 216, 217, 218, 219, 220, 221] that also attempted to extract the velocity anisotropy features of our Galaxy motivated by recent N-body simulations. These simulations suggest that the velocity distribution is not actually isotropic and the anisotropy parameter β increases from 0 at centre to 0.5 towards the outer region as observed from clusters [222, 223, 224, 225].

As mentioned , there have been several approaches to extract the anisotropy feature of DM distributions. There is proposal by [216] to generalize the Osipkov-Merritt model ([226, 227]) to the DF which generates an arbitrary value of anisotropy parameter in the halo centre with the orbits becoming fully radial at infinity. Although an analytical inversion for these models exists, the anisotropy profile cannot be reconciled with the numerical results [206]. Another work by An & Evans [228] noticed that a non- trivial profile of the anisotropy can be obtained from a sum of DFs with a constant anisotropy for which an analytical inversion is known [216, 229, 230]. However, the resulting anisotropy profiles are decreasing functions of radius and do not agree with those measured in cosmological simulations.

A different approach has been presented by [231] where the authors introduced a general ansatz for the anisotropy profile and then, for a given potential-density pair,

derived the DF as a series of some special functions. This approach works well under the condition that the potential can be expressed as an elementary function of the corresponding density. This requirement, however, is not satisfied by many models, including the NFW density profile [136] which is commonly used as a good approximation of the universal density profile of DM halos.

In Chapter II we have also presented the Eddington's formalism to revert a given density distribution to obtain the phase space distribution function and hence the velocity distribution function which by construction is a isotropic one. However as discussed above that the velocity distribution is practically an anisotropic one, also suggested by state of the art numerical simulations. The phase space distribution of dark matter particles is a priori unknown. Another plausible approach to determine the PSDF is by starting from an ansatz that the PSDF can be represented by the solution of collisionless Boltzmann equation as the DM particles can also be thought as a system of collisionless particles. In this chapter we attempt to describe a model which includes the possible anisotropic features via the description of phase space distribution function which is a function of both total energy and total angular momentum. Here we try to probe the dark matter halo structure by taking recourse to observed rotation curve data extending upto large distance [143] as discussed in previous chapter. In section 4.2 we present the visible matter model adopted in this chapter. We couple the VM with DM in a self-consistent manner and let the system converge in an iterative way so as to include the gravitational effect of VM on the DM distributions. In Section 4.3 we describe the "Michie model" of phase space distribution used here. In Section 4.4 we calculate radial and tangential dispersions, anisotropy profile, local dark matter velocity distribution (radial and tangential as well) and anisotropy parameter values at each radial point up to truncation radius, characterizing the finite extent of the DM halo. We further calculate different significant physical quantities like mass enclosed within a few representative Galactocentric radii, escape velocity etc. We further demonstrated the effect of VM on the

DM density distribution, velocity distribution, dispersion etc. for self-consistently coupled system. Finally in 4.5 we summarize our results and findings.

4.2 Visible Matter Model

We model the Visible Matter (VM) distribution of our Galaxy as a superposition of a central spherical bulge and a double exponential disk [155, 232, 233, 234]. The forms are given below:

Bulge:

$$\rho_{\text{bulge}} = \rho_{b,0} \frac{1}{[1 + (r/r_b)^2]^{3/2}}, \quad (4.1)$$

Disk:

$$\rho_{\text{disk}} = \frac{\Sigma_{\text{VM}}}{2z_d} \exp \left[-\frac{(R - R_\odot)}{r_d} \right] \exp [-z/z_d], \quad (4.2)$$

with the following parameter values : central bulge density ($\rho_{b,0}$) = $4.2 \times 10^2 M_\odot/\text{pc}^3$, bulge scale radius (r_b) = 0.103 kpc, disk scale length (r_d) = 3 kpc, disk scale height (z_d) = 0.3 kpc. We have taken three values of the local visible matter surface density (Σ_{VM}) = $48 \pm 9 M_\odot/\text{pc}^2$ i.e. (39, 48, 57) M_\odot/pc^2 .

4.3 An anisotropic Phase Space Distribution Functions for DM : The Michie Model

In this chapter we explore another approach, different from the Eddington method described in Chapter II, to find the a priori unknown PSDF of dark matter starting from an ansatz. As the DM particles are Collisionless system of particles they can

be assumed to obey the Collisionless Boltzmann equation. According to the Jeans theorem the PSDF of DM which is basically solution of the CBE are considered to depend on the position and velocity co-ordinates only via the integrals of motion. As described earlier the Isothermal model depends on the total energy of the system only and hence governs a isotropic velocity distribution. Here in this chapter we consider the Michie model which is a function of total energy and total angular momentum hence gives rise to an anisotropic velocity distribution. The PSDF of the Michie model [133, 235, 236] is given by,

$$f(\mathcal{E}, L) = \rho_1 e^{\frac{L^2}{4\pi r_a^2}} \left[e^{\frac{\Psi - v^2/2}{\sigma^2}} - 1 \right] \quad \text{for } \mathcal{E} > 0 \quad (4.3)$$

$$= 0 \quad \text{otherwise ,} \quad (4.4)$$

where $\mathcal{E} = -E + \Phi_0$ is the relative energy of the system as already discussed in Chapter II and $L = \mathbf{r} \times \mathbf{v} = rv \sin \eta$ is the angular momentum per unit mass of the system. There are four parameters in the model, namely, a density parameter (ρ_1) which can be conveniently expressed in terms of local dark matter density $\rho_{\text{DM},\odot}$, velocity anisotropy radius (r_a), which sets the length scale from where the velocity anisotropy sets in, velocity parameter (σ) which is related to the velocity dispersion and finally a truncation radius (r_t) which does not appear explicitly in the expressions but enters via the constant $\Phi_0 = \Phi(r_t)$ that defines the relative potential $\Psi(\mathbf{x}) = -\Phi(\mathbf{x}) + \Phi_0$ as described in Chapter II.

Integrating $f(\mathcal{E}, L)$ over all velocities gives the DM density at the position r as below,

$$\rho_{\text{DM}}(\mathbf{x}) \equiv \rho_{\text{DM}}(r) = \int d^3\mathbf{v} f(\mathcal{E}, L) = 2\pi \int_0^\pi d\eta \sin \eta \int_0^{v_{\text{max}}} dv v^2 f(\Psi - \frac{1}{2}v^2, rv \sin \eta) , \quad (4.5)$$

where $v_{\text{max}} (= \sqrt{2\Psi})$ goes to zero at some chosen value of truncation radius (r_t). The

density distribution satisfies the Poisson equation given by,

$$\nabla^2 \Phi_{\text{DM}}(\mathbf{x}) = 4\pi G \rho_{\text{DM}}(\mathbf{x}), \quad (4.6)$$

where Φ_{DM} is the contribution of the DM component to the total gravitational potential,

$$\Phi(\mathbf{x}) = \Phi_{\text{DM}}(\mathbf{x}) + \Phi_{\text{VM}}(\mathbf{x}), \quad (4.7)$$

in presence of the visible matter (VM) whose gravitational potential, Φ_{VM} , satisfies its own Poisson equation, namely,

$$\nabla^2 \Phi_{\text{VM}}(\mathbf{x}) = 4\pi G \rho_{\text{VM}}(\mathbf{x}). \quad (4.8)$$

We choose the boundary conditions

$$\Phi_{\text{DM}}(0) = \Phi_{\text{VM}}(0) = 0, \quad \text{and} \quad (\nabla \Phi_{\text{DM}})_{|\mathbf{x}|=0} = (\nabla \Phi_{\text{VM}})_{|\mathbf{x}|=0} = 0. \quad (4.9)$$

In practice a test particle can sense the gravitational potential of both the DM and VM. In such a coupled condition therefore the total potential is basically given by,

$$\Phi_{\text{tot}}(\mathbf{x}) = \Phi_{\text{DM,coupled}}(\mathbf{x}) + \Phi_{\text{VM}}(\mathbf{x}), \quad (4.10)$$

where $\Phi_{\text{DM,coupled}}(\mathbf{x})$ is the modified DM potential in presence of gravitational field of VM and it satisfies the Poisson's equation,

$$\nabla^2 \Phi_{\text{DM,coupled}}(\mathbf{x}) = 4\pi G \rho_{\text{DM,coupled}}(\mathbf{x}). \quad (4.11)$$

The coupled dark matter density now is given as, using equation (4.5),

$$\rho_{\text{DM,coupled}}(r) = 2\pi \int_0^\pi d\eta \sin \eta \int_0^{v_{\text{max}}} dv v^2 f(\Psi_{\text{tot}} - \frac{1}{2}v^2, rv \sin \eta), \quad (4.12)$$

with the $\Psi(\mathbf{x})$ in equation (4.5) being replaced by $\Psi_{\text{tot}}(\mathbf{x})$ where $\Psi_{\text{tot}}(\mathbf{x})$ is given below,

$$\begin{aligned} \Psi_{\text{tot}}(\mathbf{x}) &= \Psi_{\text{DM,coupled}}(\mathbf{x}) + \Psi_{\text{VM}}(\mathbf{x}), \\ &= -\Phi_{\text{DM,coupled}}(\mathbf{x}) + \Phi_{\text{DM,coupled}}(r_t) - \Phi_{\text{VM}}(\mathbf{x}) + \Phi_{\text{VM}}(r_t). \end{aligned} \quad (4.13)$$

The coupled Poisson's equation can be solved in an iterative manner until the system converges by including the effect of the VM in a self-consistent manner as described above. By deriving the potential distribution in this way one can calculate the density distribution.

With the radial and tangential velocities defined as

$$v_r = v \cos \eta \quad \text{and} \quad v_t = \sqrt{v_\theta^2 + v_\phi^2} = v \sin \eta,$$

respectively, one can calculate normalized velocity distributions, i.e. total, radial and tangential as given bellow.

The normalized total velocity distribution function:

$$f(r, v) = \frac{2\pi}{\rho(r)} \int_0^\pi d\eta \sin \eta v^2 f(\Psi - \frac{1}{2}v^2, rv \sin \eta) \quad \text{with } v : 0 \text{ to } \sqrt{2\Psi}, \quad (4.14)$$

with $\int_0^{v_{\text{max}}=\sqrt{2\Psi}} f(r, v) dv = 1$.

The normalized radial velocity distribution function :

$$f_r(r, v_r) = \frac{2\pi}{\rho(r)} \int_{-\sqrt{2\Psi-v_r^2}}^{\sqrt{2\Psi-v_r^2}} dv_t v_t f\left(\Psi - \frac{1}{2}(v_r^2 + v_t^2), rv_t\right) \text{ with } v_r : -\sqrt{2\Psi} \text{ to } \sqrt{2\Psi}, \quad (4.15)$$

with $\int_{-\sqrt{2\Psi}}^{\sqrt{2\Psi}} f_r(r, v_r) dv_r = 1$.

The normalized tangential velocity distribution function :

$$f_t(r, v_t) = \frac{2\pi}{\rho(r)} \int_0^{\sqrt{2\Psi-v_t^2}} dv_r v_r f\left(\Psi - \frac{1}{2}(v_r^2 + v_t^2), rv_t\right) \text{ with } v_t : 0 \text{ to } \sqrt{2\Psi}, \quad (4.16)$$

with $\int_0^{\sqrt{2\Psi}} f_t(r, v_t) dv_t = 1$.

One can calculate the velocity moments and the anisotropy parameter $\beta = 1 - \frac{\sigma_t^2}{2\sigma_r^2}$ with the aid of the expressions given above. The quantities σ_t and the σ_r are the tangential and radial velocity dispersions, respectively.

The advantages of the Michie model are the followings : it represents a finite sized galaxy as the model has a truncation radius r_t and the velocity space is also bound by a maximum allowed velocity v_{\max} self-consistently determined by the model itself. The model also allows the velocity distribution to have anisotropic nature as the PSDF is function of both total energy and total angular momentum.

4.4 Deriving the parameters of Michie model by fitting the RC data : Results

For a given set of the Galactic model parameters, the circular rotation speed, $v_c(R)$, as a function of the Galactocentric distance R , is given by,

$$v_c^2(R) = R \frac{\partial}{\partial R} \left[\Phi_{\text{DM}}(R, z=0) + \Phi_{\text{VM}}(R, z=0) \right]. \quad (4.17)$$

For the observational data, we use RC data given in Chapter III [143]. The rotation curve data adopted is standardized at the two GC sets $\left[\frac{R_0}{\text{kpc}}, \frac{V_0}{\text{km s}^{-1}}\right] : [8.3, 244]$ and $[8.5, 220]$ and a velocity anisotropy of the tracer distribution adopted from the hydrodynamic simulation by [182]. The RC extends up to Galactocentric distances well beyond the visible edge of the Galaxy up to ~ 200 kpc. In order to perform the fit we use the χ^2 -test defined as $\chi^2 \equiv \sum_{i=1}^{i=N} \left(\frac{v_{\text{c,obs}}^i - v_{\text{c,th}}^i}{v_{\text{c,error}}^i}\right)^2$, where $v_{\text{c,obs}}^i$ and $v_{\text{c,error}}^i$ are, respectively, the observational value of the circular rotation speed and its error at the i -th value of the Galactocentric distance, and $v_{\text{c,th}}^i$ is the corresponding theoretically calculated circular rotation speed given by equation (4.17). The VM model and the VM parameter values are taken as described in Section 4.2.

The results of the fit to the rotation curve data with Michie model are presented in Figure 4.1. These plots also demonstrate the effect of varying the Σ_{VM} on the results. The left panel of Figure 4.1 shows the RC fit for the GC standard $[8.3, 244]$ for three adopted values of VM disk surface density at solar location, namely, $(39, 48, 57)M_{\odot}/\text{pc}^2$ from top to bottom panel respectively. The right panel represents the same but with GC set $[8.5, 220]$. The reason for choosing two sets of GCs is the following : as the local circular velocity increases the RC profile as a whole shifts in upward direction specifically at the solar location. This rise in the RC profile at solar location can be supported by increased local dark matter density and/or the local VM disk surface density. The local dark matter density (ρ_{\odot}) is kept as a free parameter whereas the local VM disk surface density (Σ_{VM}) is fixed at three values widely covering the range suggested by other observations [233]. The effect is evident in Table 4.1 in which the best fit parameter values obtained are summarized. For the GC set with higher local circular velocity i.e. 244 km s^{-1} the local dark matter density ρ_{\odot} comes out to be larger around 0.6 GeV cm^{-3} whereas for the GC set with lower circular velocity i.e. 220 km s^{-1} ρ_{\odot} comes out to be smaller around 0.4 GeV cm^{-3} irrespective of the value of local Σ_{VM} . Therefore the results show that the local dark matter density is sensitive to the choice of the GC values.

Local VM Disk Surface Density		DM Parameters			
Σ_{VM} ($M_{\odot}\text{pc}^{-2}$)	$\rho_{\text{DM},\odot}$ (GeV cm^{-3})	σ (100 km s^{-1})	r_t (kpc)	r_a (kpc)	χ^2 -
		GC : [8.3,244]			
39	0.65	17.5	232	0.9	7.23
48	0.62	8.0	278	2.2	7.3
57	0.57	20.5	295	0.9	7.58
		GC : [8.5,220]			
39	0.44	13.0	318	1.2	4.69
48	0.40	10.0	370	1.8	5.04
57	0.36	11.5	374	1.9	5.60

Table 4.1: Best Fit Michie model (DM) parameters for two different sets of Galactic Constants (GCs) : $\left[\frac{R_0}{\text{kpc}}, \frac{V_0}{\text{km s}^{-1}} \right]$, namely [8.3,244] and [8.5,220] (I.A.U. standard) with the visible matter model and the parameter values as described in previous section. The visible matter disk surface density at solar location is fixed at three values ($\Sigma_{\text{VM}} = 48 \pm 9 M_{\odot}\text{pc}^{-2}$) covering the range as allowed by observations [237].

Higher the local circular velocity higher is the local dark matter density. This result is quite robust even with the variation of the local VM disk surface density Σ_{VM} .

In Table 4.2 we present various physical quantities like bulge mass, disk mass, DM halo mass, total mass of the Galaxy upto various Galactocentric radii etc. We further present the values of local dark matter circular velocity, maximum velocity, radial, tangential and total velocity dispersions and local anisotropy parameter. The values are calculated for two sets of GCs as mentioned also for three choices of the VM disk surface density. As we can clearly observe from Table 4.2 that the total mass of the Galaxy at different radii is also higher for the GC set with higher local circular velocity and as a result the local maximum velocity is also higher in this case i.e. 523 km s^{-1} as compared to 468 km s^{-1} for $\Sigma_{\text{VM}} = 48 M_{\odot}\text{pc}^{-2}$.

In Figure 4.2 we present the density distribution of the dark matter and the visible matter along equatorial plane and in vertical direction. We also present the DM

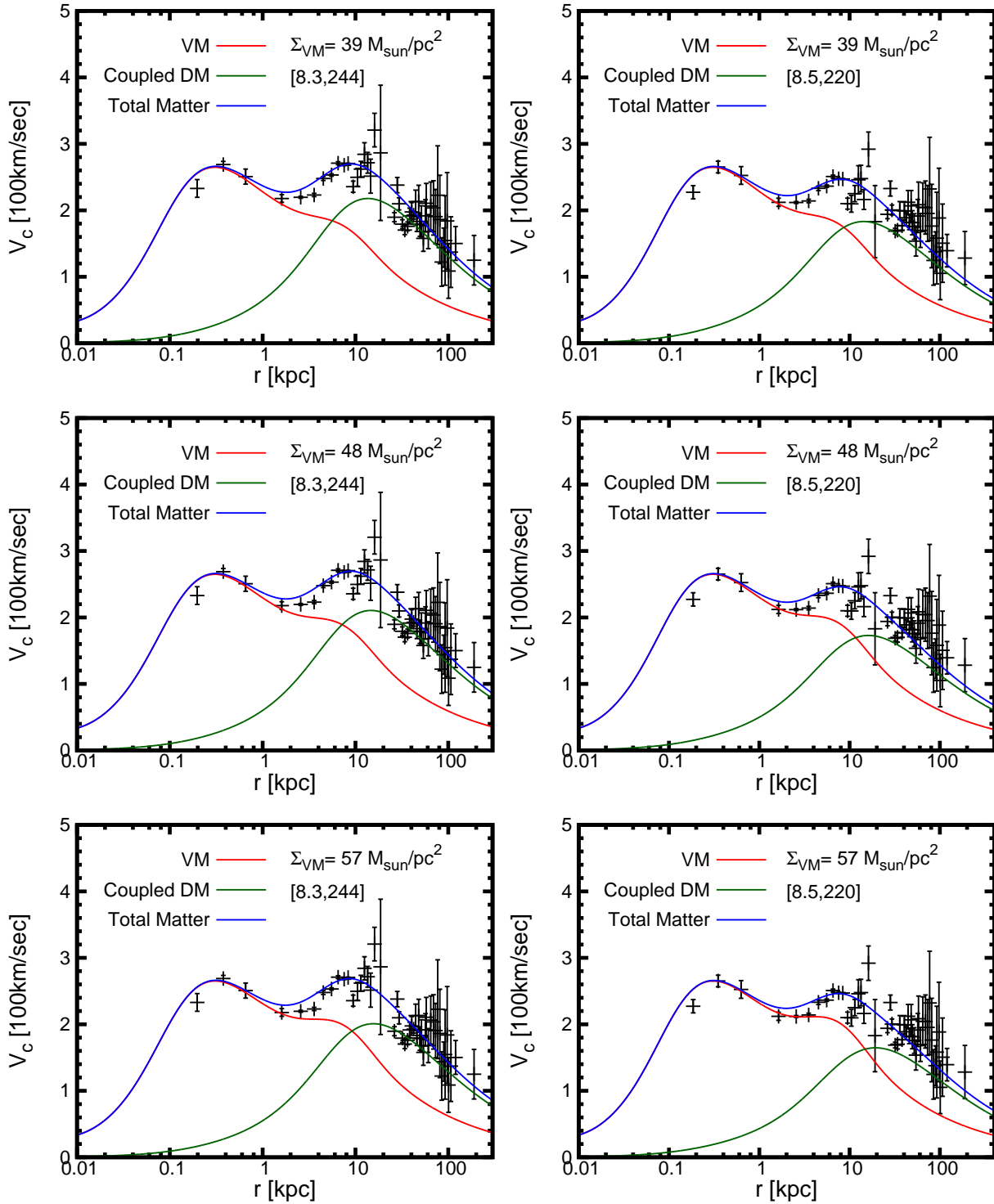


Figure 4.1: Fit to the rotation curve data standardized at two sets of GCs $\left[\frac{R_0}{\text{kpc}}, \frac{V_0}{\text{km s}^{-1}}\right]$: [8.3, 244] and [8.5, 220] left and right panel respectively. Plots are also demonstrated for three values of Σ_{VM} from top panel to bottom panel, (39, 48, 57) $M_{\odot}\text{pc}^{-2}$ respectively.

Derived Quantities	Unit		[8.3,244]			[8.5,220]	
Σ_{VM}	$M_{\odot}\text{pc}^{-2}$	39	48	57	39	48	57
Bulge mass	$10^{10} M_{\odot}$	4.4	4.4	4.4	4.5	4.5	4.5
Disk mass	$10^{10} M_{\odot}$	3.5	4.4	5.2	3.8	4.7	5.6
Total VM mass	$10^{10} M_{\odot}$	7.9	8.8	9.6	8.3	9.2	10.1
DM Halo virial radius	kpc	156	157	155	143	143	146
DM Halo virial mass	$10^{11} M_{\odot}$	4.1	4.2	4.1	3.2	3.2	3.4
Total virial mass	$10^{11} M_{\odot}$	4.9	5.1	5.0	4.0	4.1	4.3
Truncation radius	kpc	232	278	287	318	370	374
DM halo mass	$10^{11} M_{\odot}$	4.2	4.3	4.2	3.3	3.4	3.6
Total mass of Galaxy	$10^{11} M_{\odot}$	5.0	5.2	5.1	4.2	4.3	4.6
DM mass within R_{\odot}	$10^{10} M_{\odot}$	8.2	7.4	6.5	5.9	5.0	4.1
VM mass within R_{\odot}	$10^{10} M_{\odot}$	5.0	5.6	6.3	5.3	5.9	6.6
Total mass within R_{\odot}	$10^{11} M_{\odot}$	1.3	1.3	1.3	1.1	1.1	1.1
Total Mass within 50 kpc	$10^{11} M_{\odot}$	4.1	4.1	4.0	3.2	3.2	3.3
Total Mass within 60 kpc	$10^{11} M_{\odot}$	4.3	4.3	4.2	3.4	3.4	3.5
Total Mass within 100 kpc	$10^{11} M_{\odot}$	4.7	4.8	4.7	3.8	3.9	4.1
Total Mass within 200 kpc	$10^{11} M_{\odot}$	4.9	5.1	5.1	4.1	4.2	4.5
Local maximum velocity	km s^{-1}	519	523	519	468	468	471
Local most probable velocity	km s^{-1}	280	287	299	257	269	289
Local anisotropy	km s^{-1}	0.51	0.45	0.42	0.47	0.38	0.29
Local total dispersion	km s^{-1}	298	304	307	272	279	288
Local radial dispersion	km s^{-1}	212	210	209	189	187	186
Local tangential dispersion	km s^{-1}	209	220	225	195	207	220
Local DM surface density	$M_{\odot}\text{pc}^{-2}$	39.5	37.6	34.6	27.4	24.9	22.4

Table 4.2: Physically relevant derived quantities calculated for Michie model for three different Σ_{VM} values and for two sets of GCs.

distribution for two cases, namely “coupled” i.e. when the system includes the effect of VM self consistently and converges in an iterative manner as described in Section 4.3 and “uncoupled” case in which the gravitational effect of VM on DM is not taken into account. As we notice from the figure that the DM core density is much higher and the core radius is much shorter in the coupled case as compared to the uncoupled case because of the fact that the VM pulls in more DM towards the centre. The DM density in the disk region is also enhanced (almost by $\sim 20\%$) due to the the effect of VM.

In Figure 4.3 and Figure 4.4 we present the mass distribution and maximum velocity v_{\max} profiles respectively for two sets of rotation curve data standardized at $\left[\frac{R_0}{\text{kpc}}, \frac{V_0}{\text{km s}^{-1}}\right]$ [8.3,244] and [8.5,220]. The plots are made for the local VM disk surface density value $\Sigma_{\text{VM}} = 48M_{\odot}\text{pc}^{-2}$ only, as from the table 4.1 it is evident that variation of local Σ_{VM} doesn't affect the results significantly.

In Figure 4.5 we present the velocity dispersion profiles for all three cases, namely, the radial, tangential and total velocity dispersions for above mentioned cases. An important point to note is that the VM coupling significantly affects all the velocity dispersion profiles. For the coupled case (referred in the figures as “with VM” case) the dispersion is much higher. In Figure 4.6 all three velocity distribution functions, i.e. radial, tangential and total, at solar location are presented. These plots also demonstrate that for the coupled case the distribution is wider (i.e. the velocity dispersion is larger) and the maximum velocity v_{\max} and the most probable velocity represented by the position of the peak of the distribution are also higher. We also present the VDFs at other Galactic radii in Figure 4.7 which are visibly non-Maxwellian like the VDFs described above as expected for simulation results also. Local VDFs are important for calculation of direct dark matter event rates whereas for indirect case one needs global information in order to evaluate the rates at Galactic centre, substructure etc. From the cosmological simulations it is observed

that the shape of the radial VDF changes as a function of radius [205, 238, 239, 240] as also observed here. In particular, VDFs in the inner region tend to have long tails i.e. more particles at high velocity compared to a Gaussian one whereas those at larger radii tend to have stronger reduction in the number of high velocity particles.

The radial dependence of the anisotropy parameter (β) is shown in Figure 4.8. The plots are presented for the local VM disk surface density value of $\Sigma_{\text{VM}} = 48M_{\odot}\text{pc}^{-2}$. For the GC set [8.3,244] the best fit anisotropy radius value is found to be 2.2 kpc and the local anisotropy parameter value is 0.45. For the GC set [8.5,220] the best fit anisotropy radius value is found to be 1.8 kpc and the corresponding local anisotropy parameter value is 0.38. These values are not significantly changed for other Σ_{VM} values. Both the profiles show that the anisotropy profile rises from 0 value at centre to constant value 1 towards outer radii consistent with the behavior observed from various numerical simulations.

We further demonstrate the effect of choice of various VM disk surface density Σ_{VM} at solar location on mass profile and local VDFs are illustrated in Figure 4.9. The mass profiles remain unaffected, however the local VDFs are affected by small amount without changing the overall nature.

4.5 Summary

In this chapter we have constructed a phase space distribution function of dark matter particles with anisotropic velocity distribution starting from an ansatz. We have assumed that being collisionless system of particles the DM obeys the collisionless Boltzmann equation (CBE) and hence their PSDF can be expressed as a solution of the CBE. Here we have adopted the ‘‘Michie model’’ which is a function of both total energy and total angular momentum of the system thus allowing possible velocity anisotropy of the system as also suggested by recent numerical simulations of

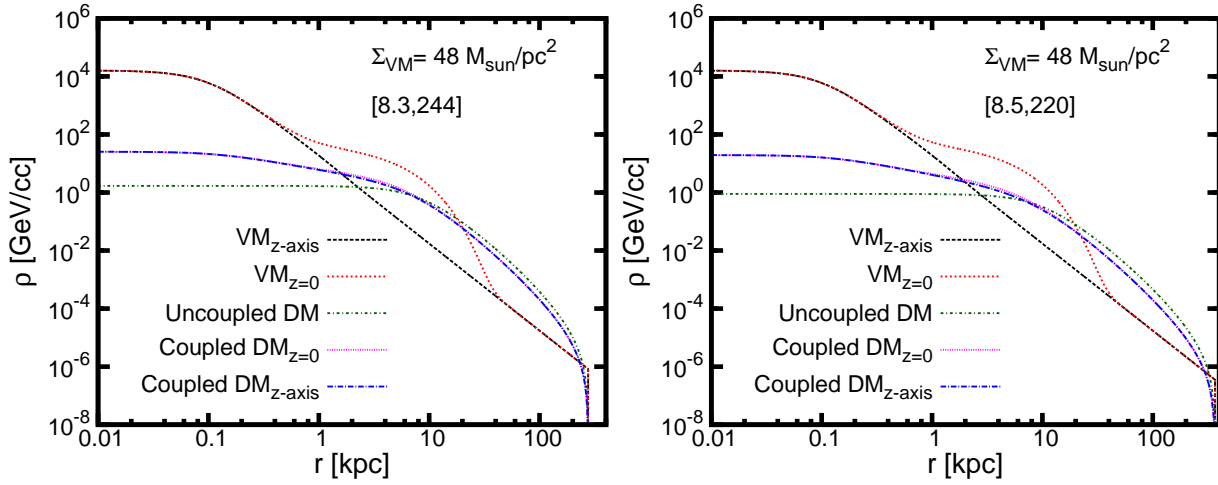


Figure 4.2: Density profile for best-fit model parameter values. The plots shown are for the $\Sigma_{\text{VM}} = 48 M_{\odot} \text{pc}^{-2}$ value and for the two RC data profiles standardized at two sets of GCs $\left[\frac{R_0}{\text{kpc}}, \frac{V_0}{\text{km s}^{-1}} \right] : [8.3, 244]$ and $[8.5, 220]$ in left and right panel respectively. The plots further demonstrate the effect of inclusion of VM in a self consistent manner. The core density is increased and the core radius is shortened. The DM density around the disk is also significantly enhanced.

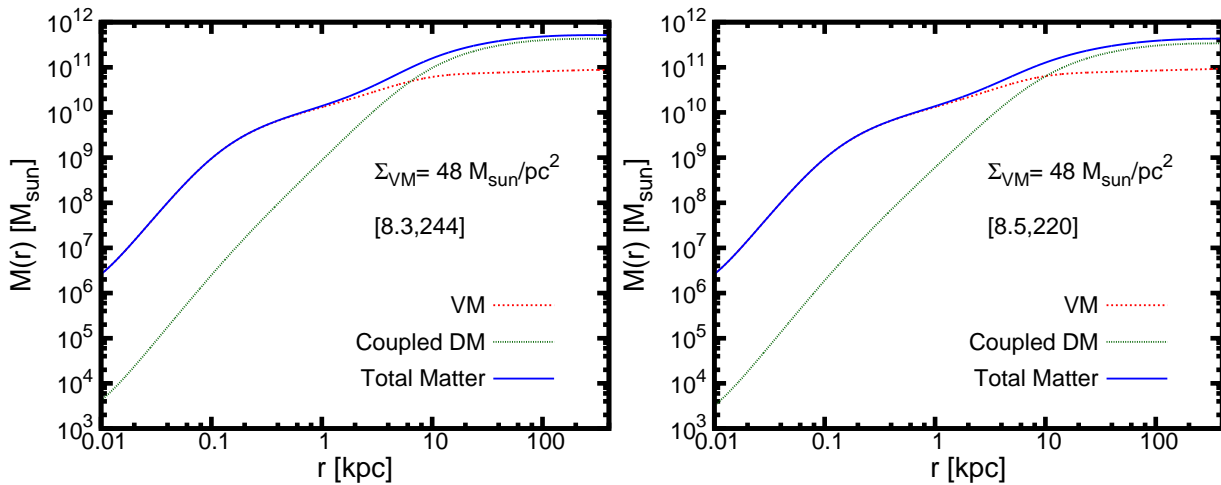


Figure 4.3: The mass profiles are shown for the $\Sigma_{\text{VM}} = 48 M_{\odot} \text{pc}^{-2}$ value and for the two RC data profiles standardized at two sets of GCs $\left[\frac{R_0}{\text{kpc}}, \frac{V_0}{\text{km s}^{-1}} \right] : [8.3, 244]$ and $[8.5, 220]$ in left and right panel respectively.

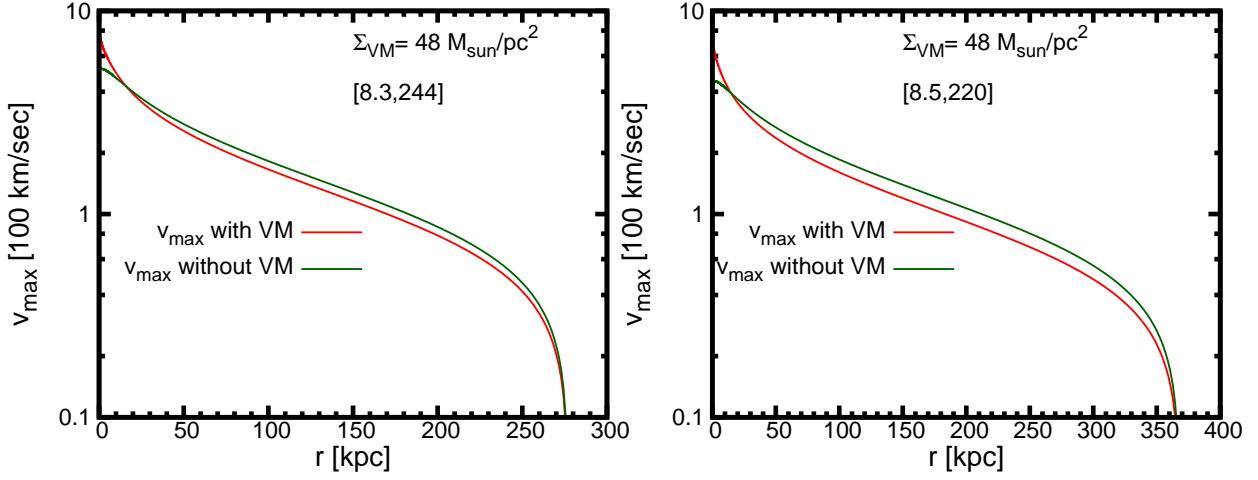


Figure 4.4: The Maximum velocity v_{\max} profiles are shown for the $\Sigma_{\text{VM}} = 48 M_{\odot} \text{pc}^{-2}$ value and for the two RC data profiles standardised at two sets of GCs $\left[\frac{R_0}{\text{kpc}}, \frac{V_0}{\text{km s}^{-1}} \right]$: [8.3, 244] and [8.5, 220] in left and right panel respectively.

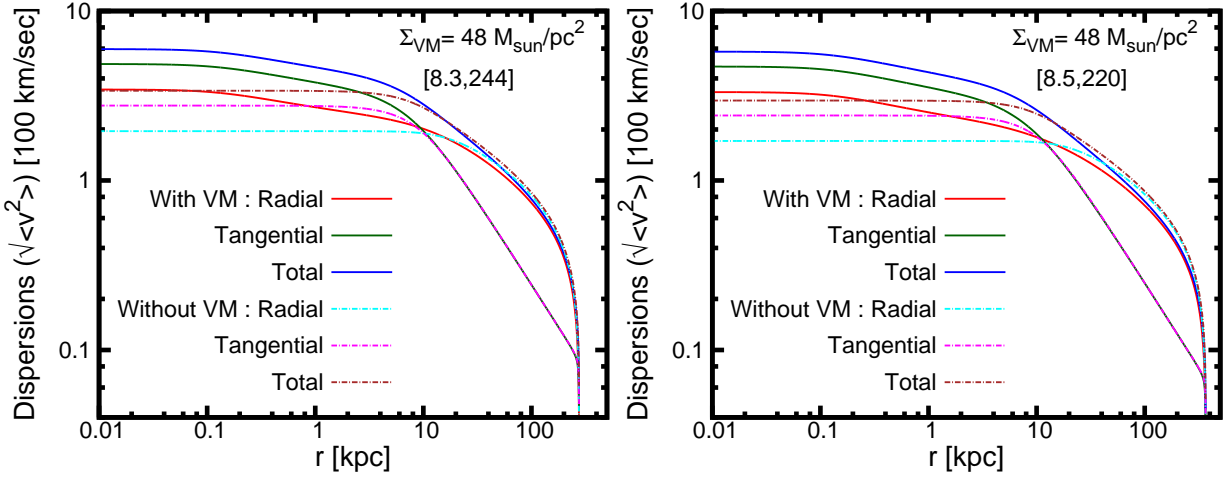


Figure 4.5: The velocity dispersion profiles (radial, tangential and total) are shown for the $\Sigma_{\text{VM}} = 48 M_{\odot} \text{pc}^{-2}$ value and for the two RC data profiles standardized at two sets of GCs $\left[\frac{R_0}{\text{kpc}}, \frac{V_0}{\text{km s}^{-1}} \right]$: [8.3, 244] and [8.5, 220] in left and right panel respectively.

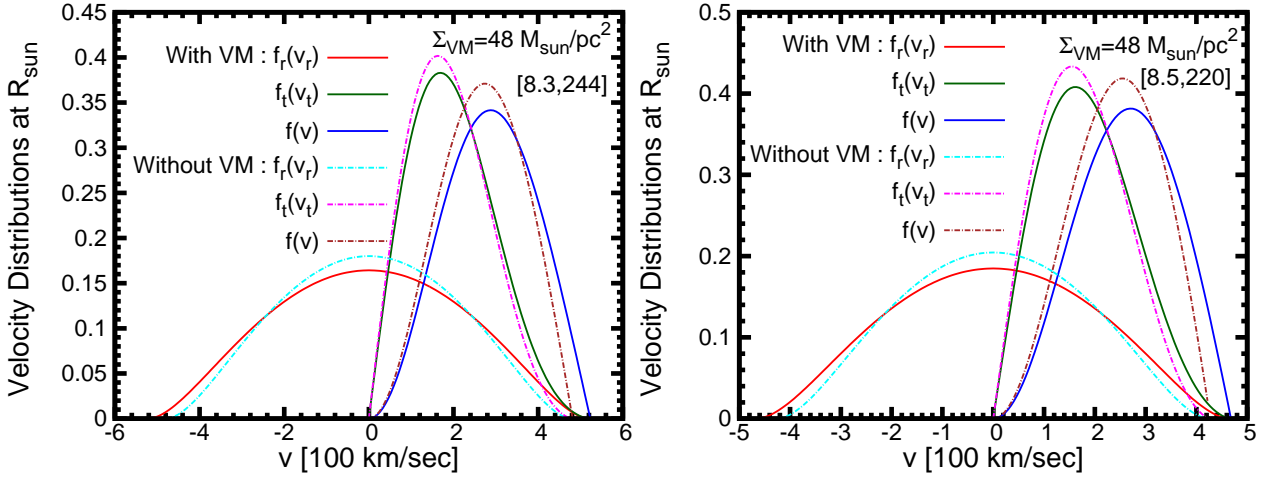


Figure 4.6: The local velocity distribution functions (radial, tangential and total) are shown for the $\Sigma_{\text{VM}} = 48 M_{\odot} \text{pc}^{-2}$ value and for the two RC data profiles standardized at two sets of GCs $\left[\frac{R_0}{\text{kpc}}, \frac{V_0}{\text{km s}^{-1}} \right] : [8.3, 244]$ and $[8.5, 220]$ in left and right panel respectively.

galaxies and clusters. We have self-consistently included the gravitational effect of visible matter in the model. We have performed fit to the rotation curve data to determine the best-fit values of the model parameters. We have found that the local dark matter density which is one of the parameters of the model comes out to be higher for that set of rotation curve data which is standardized at higher value of local circular velocity and this result is independent of the choice of the local VM disk surface density. As an effect of the coupling with the visible matter the core radius of the dark matter halo gets shortened and the core density is increased because the VM pulls in more dark matter towards the centre. The dark matter density near the disk region is also enhanced by a factor of $\sim 20\%$. The velocity dispersions, namely the radial, tangential and total velocity dispersions are also found to be higher in the coupled case as compared to the uncoupled case. The radial, tangential and total velocity distributions at solar location as well as at other Galactic radii is found to be non-Maxwellian. The value of the anisotropy parameter is observed to rise from a 0 value at centre to a value 1 at long distance which is consistent with observations from numerical simulations.

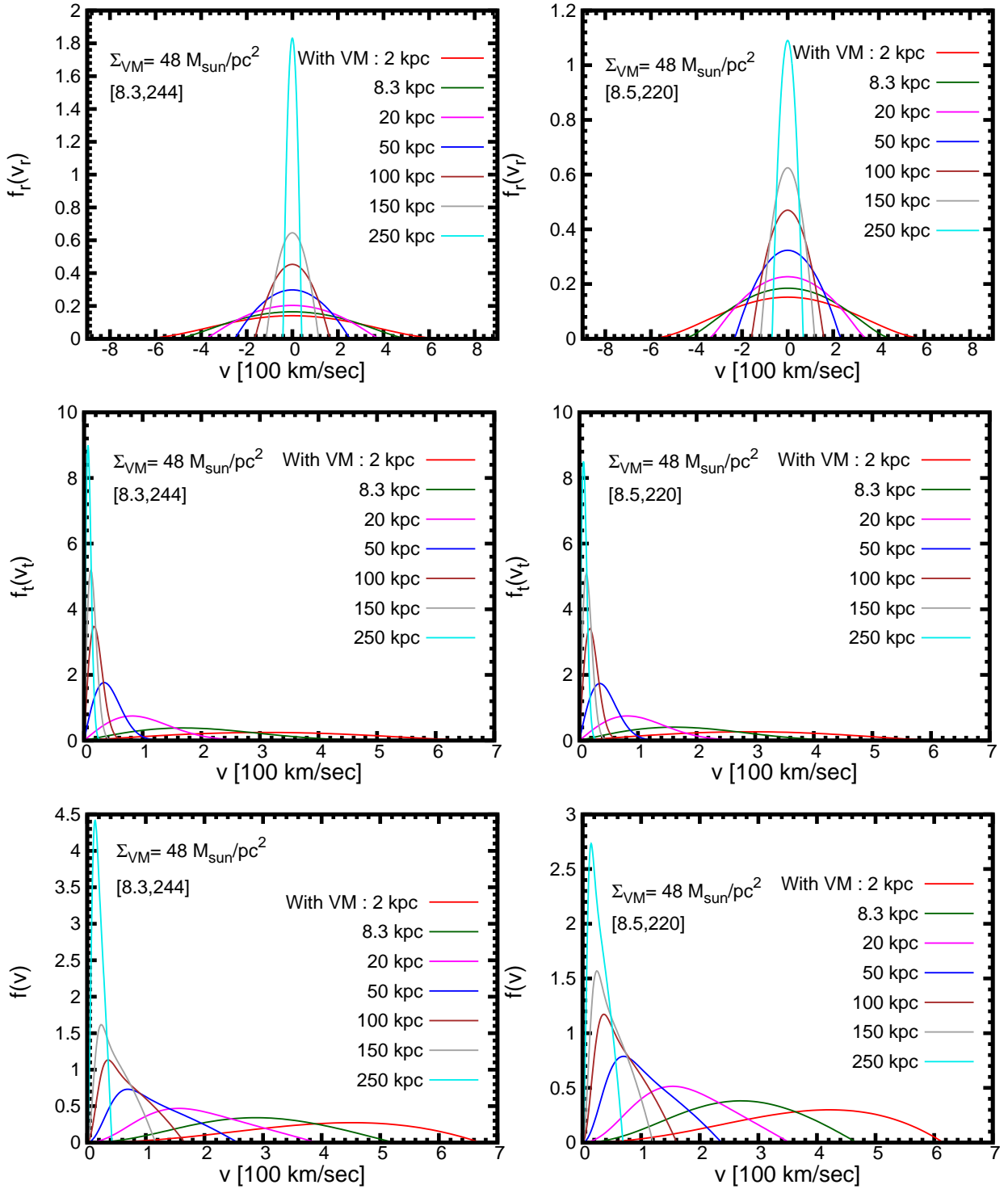


Figure 4.7: The velocity distribution functions (radial, tangential and total) at various Galactic radii are shown for the $\Sigma_{\text{VM}} = 48 M_{\odot} \text{pc}^{-2}$ value and for the two RC data profiles standardized at two sets of GCs $\left[\frac{R_0}{\text{kpc}}, \frac{V_0}{\text{km s}^{-1}} \right] : [8.3, 244]$ and $[8.5, 220]$ in left and right panel respectively.

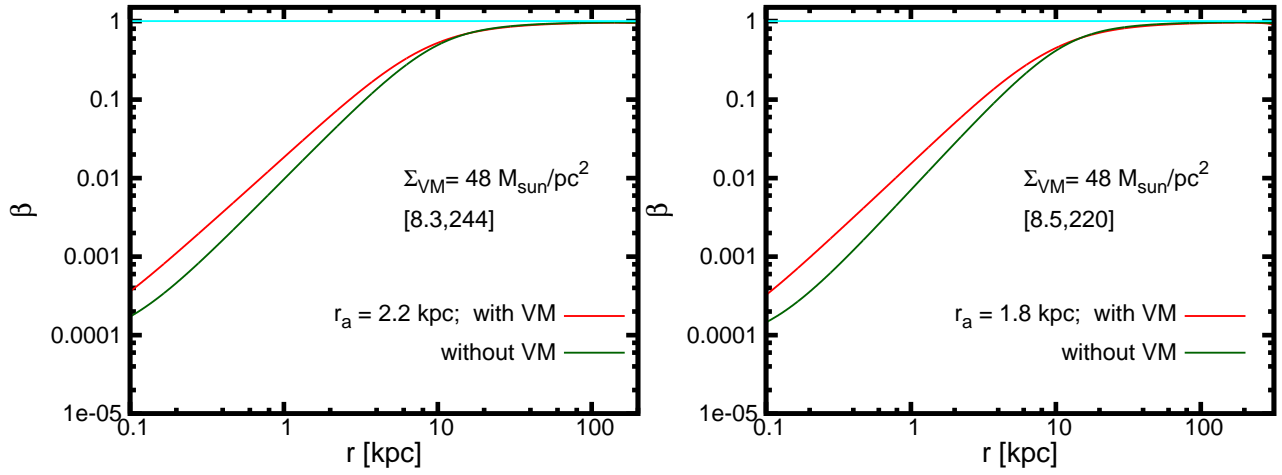


Figure 4.8: The anisotropy parameter profile for the $\Sigma_{\text{VM}} = 48 M_{\odot} \text{pc}^{-2}$ value and for the two RC data profiles standardized at two sets of GCs $\left[\frac{R_0}{\text{kpc}}, \frac{V_0}{\text{km s}^{-1}} \right] : [8.3, 244]$ and $[8.5, 220]$ in left and right panel respectively.

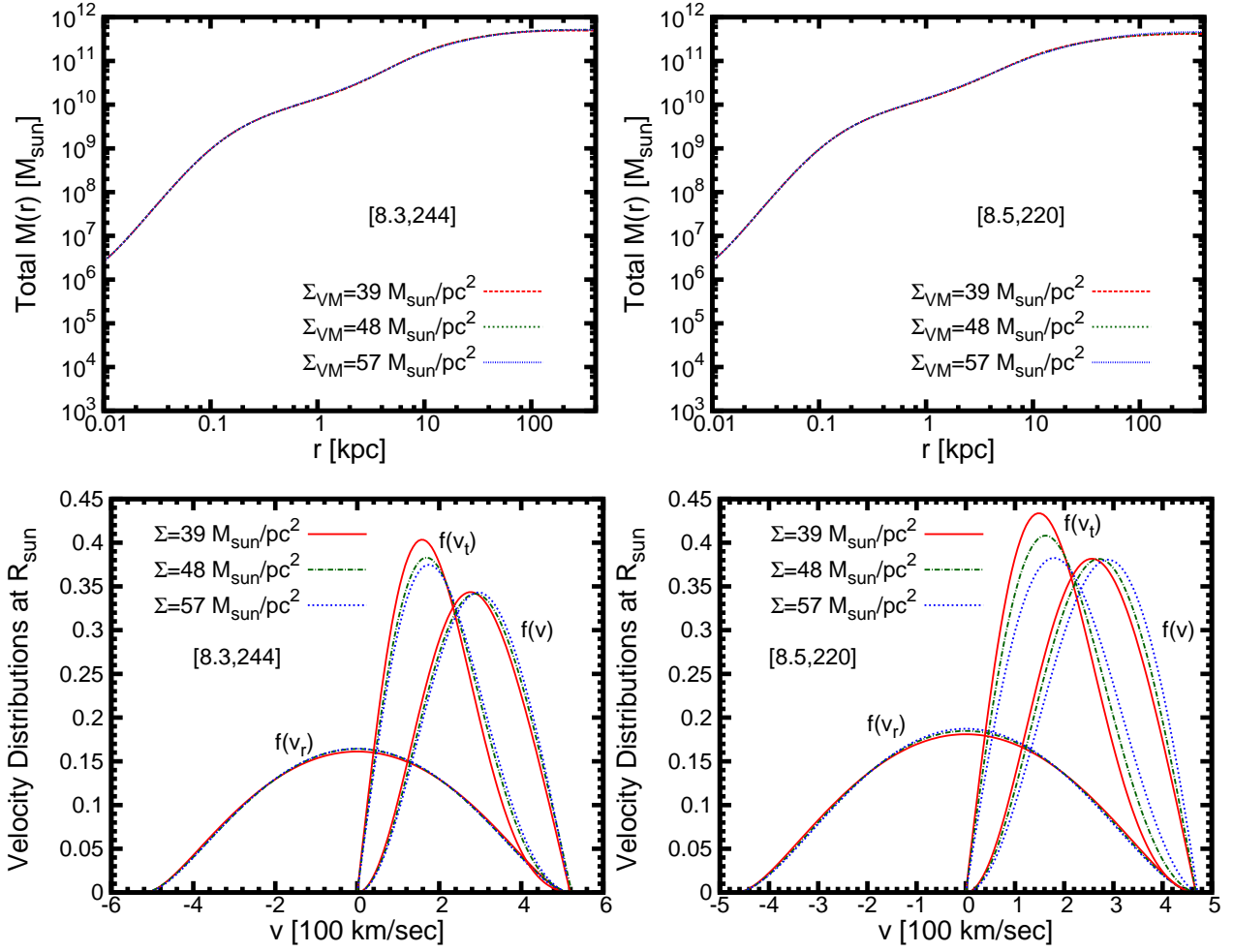


Figure 4.9: Effect of different Σ_{VM} on Mass profiles (top panel) and local velocity profiles (bottom panel) for the two RC data profiles standardized at two sets of GCs $\left[\frac{R_0}{\text{kpc}}, \frac{V_0}{\text{km s}^{-1}} \right] : [8.3, 244]$ and $[8.5, 220]$ in left and right panel respectively.

Chapter 5

Indirect Detection of WIMPs : Capture and Annihilation Rates of WIMPs within the Sun

5.1 Introduction

In the previous chapters we have discussed how the rotation curve (RC) data can be used to extract information about the phase space distribution of the weakly interacting massive particles (WIMPs) hypothesized to constitute the dark matter (DM) halo of our Galaxy, the Milky way. We have seen that the velocity distribution function (VDF) of the DM particles constituting a finite sized DM halo of the Galaxy can depart significantly from the Maxwellian form usually assumed in the standard halo model (SHM). We have also seen how the gravitational influence of the visible matter (VM) of the Galaxy can have significant effect in determining the density and velocity distribution of dark matter particles, especially within the solar circle. As already mentioned the density and velocity distribution of the DM particles in the

solar neighborhood have direct bearings on the direct as well as indirect detection of the WIMPs. In the present chapter and in the following one, we discuss indirect detection of WIMPs through neutrino signal due to capture and annihilation of the WIMPs inside the Sun within the context of a self-consistent model of the phase space structure of the finite sized DM halo of the Galaxy. The model is based on the so called “King model”, also referred to as “lowered (or truncated) Isothermal model”, the PSDF of which is a solution of collisionless Boltzmann equation (CBE). The model is properly modified to include the effect of the gravitational influence of the observed visible matter (VM) in a self consistent manner, with the parameters of the model determined by fit to the observed RC data for the Galaxy extending upto Galactic radii as large as ~ 200 kpc.

In this chapter and the next chapter we focus on the indirect detection of WIMPs [2, 3, 4, 145, 6] through neutrino signal due to WIMP annihilation in the Sun. Scattering of WIMPs off nuclei can lead to capture of the WIMPs by massive astrophysical bodies such as the Sun or the Earth if, after scattering off a nucleus inside the body, the velocity of the WIMP falls below the escape velocity of the body. The WIMPs so captured over the lifetime of the capturing body would gradually settle down to the core of the body where they would annihilate and produce standard model particles, e.g., W^+W^- , Z^0Z^0 , $\tau^+\tau^-$, $t\bar{t}$, $b\bar{b}$, $c\bar{c}$, etc. Decays of these particles would then produce neutrinos, gamma rays, electrons-positrons, protons-antiprotons, etc. For astrophysical objects like the Sun or the Earth, only the neutrinos would be able to escape. Detection of these neutrinos by large neutrino detectors can, albeit indirectly, provide a signature of WIMPs. Although no detection has yet been reported, the Super-Kamiokande (S-K) detector, for example, has provided upper limits on the possible neutrino flux from WIMP annihilation in the Sun as a function of the WIMP mass [147, 148, 241]. IceCube [242, 243], another gigantic neutrino detector at the south pole, has also provided upper limits the possible neutrino flux from WIMP annihilation in the Sun. Tight limits

on the WIMP-induced neutrino flux from the Sun have been placed with neutrino telescopes such as IceCube [244], Baksan [245] and ANTARES [246]. Similarly, the γ -rays produced in the annihilation of the WIMPs in suitable astrophysical environments with enhanced DM density but low optical depth to gamma rays, such as in the central region of our Galaxy, in dark matter dominated objects such as dwarf galaxies, and in clusters of galaxies, can offer a complimentary avenue of indirect detection (ID) of WIMPs [247, 248]. Antimatter searches also can provide information about the WIMPs in the Galaxy [249, 250]. All these are discussed in detail in Chapter I.

In this chapter we present our calculation of capture and annihilation rates within the context of a self-consistent model of the phase space distribution function of the DM halo of the Galaxy, namely the King model. In Section 5.2 and Section 5.3 we describe the general formalism of calculating the capture and annihilation rates of WIMPs within the Sun. In Section 5.4 we describe the King model, appropriately modified to include the gravitational influence of the observed visible matter on the DM. We determine the parameters of the model by fit to the RC data of the Galaxy. The resulting model is then used in Section 5.5 to calculate the capture and annihilation rates of the WIMPs using the formalism described in Section 5.2 and Section 5.3. The reason of selecting the King model is the following : Our goal is to probe the WIMP parameter space namely the WIMP mass and WIMP-nucleon scattering cross section. We would present our results in terms of the limits on branching fractions in each annihilation channel. In order to do so we need to compare our upper limits on the WIMP-nucleon scattering cross section as obtained from the detection result of the Super-Kamiokande (SK) detector with those obtained from direct detection experiments then by demanding the consistency between the two we can put limit on the allowed branching fractions. Therefore we use the results on direct detection experiments as obtained in [155] in the context of the same model of the phase space distribution function, i.e. King model. Finally

we summarize the results in Section 5.6.

5.2 Calculation of Capture Rate

In the present section we focus on the calculation of WIMP capture rate by Sun. There are several works in literature that attempt to calculate the capture rate mainly within the context of the “Standard Halo Model” (SHM) described in Chapter II that gives Maxwellian velocity distribution [251, 252, 253, 149, 148, 254]. In this section we present the calculation of capture rate for any generic velocity distribution. The capture rate of WIMPs per unit volume at radius r inside the Sun can be written as [253, 251]

$$\frac{dC}{dV}(r) = \int d^3\mathbf{u} \frac{\tilde{f}(\mathbf{u})}{u} w \Omega^-(w), \quad (5.1)$$

where $\tilde{f}(\mathbf{u})$ is the WIMP velocity distribution, as measured in the Sun’s rest frame, in the neighborhood of the Sun’s location in the Galaxy, and $w(r) = \sqrt{u^2 + w_{\text{esc}}^2(r)}$ is the WIMP’s speed at the radius r inside the Sun neglecting the focusing effect of the Sun, $w_{\text{esc}}(r)$ being the escape speed at that radius inside the Sun, which is related to the escape speed at the Sun’s core, $w_{\text{esc,core}} \approx 1354 \text{ km s}^{-1}$, and that at its surface, $w_{\text{esc,surf}} \approx 795 \text{ km s}^{-1}$, by the relation,

$$w_{\text{esc}}^2(r) = (w_{\text{esc,core}})^2 - \frac{M(r)}{M_{\odot}} [(w_{\text{esc,core}})^2 - (w_{\text{esc,surf}})^2]. \quad (5.2)$$

The quantity $\Omega^-(w)$ is the capture probability per unit time, which is just the product of the scattering rate and the conditional probability that after a scattering the WIMP’s speed falls below the escape speed.

We shall here consider only the elastic scattering of the WIMPs off nuclei. The dominant contribution to the WIMP capture rate will come from the WIMPs scat-

tering off hydrogen and helium nuclei. The WIMPs can interact with the nucleons via spin-independent (SI) interaction in case of which it is assumed that the WIMP interacts coherently with the nucleus as a whole. The WIMPs may interact with the nucleons via spin-dependent (SD) interaction as well in case of which WIMP couples to the total spin J of the nucleus which has contributions from the spins of the individual protons and neutrons within the nucleus. For hydrogen, both spin-independent (SI) as well as spin-dependent (SD) cross sections, $\sigma_{\chi p}^{\text{SI}}$ and $\sigma_{\chi p}^{\text{SD}}$, respectively, will contribute, but for helium only SI cross section is relevant. (We neglect here the small contribution from ${}^3\text{He}$). In general, the effective momentum-transfer (q) dependent WIMP-nucleus SI scattering cross section, $\sigma_{\chi A}^{\text{SI}}(q)$, can be written in the usual way in terms of the “zero-momentum” WIMP-proton (or WIMP-neutron) effective cross section, $\sigma_{\chi p}^{\text{SI}} = \sigma_{\chi n}^{\text{SI}}$, as

$$\sigma_{\chi A}^{\text{SI}}(q) = \frac{\mu_{\chi A}^2}{\mu_{\chi p}^2} \sigma_{\chi p}^{\text{SI}} A^2 |F(q^2)|^2, \quad (5.3)$$

where A is the number of neutrons plus protons in the nucleus, $\mu_{\chi A}$ and $\mu_{\chi p}$ are the reduced masses of WIMP-nucleus and WIMP-proton systems, respectively, with $\mu_{\chi i} = (m_i m_\chi)/(m_i + m_\chi)$, and $F(q^2)$ is the nuclear form-factor (with $F(0) = 1$). We shall choose the Helm-Gould exponential nuclear form factor [2, 253] given by,

$$|F(q^2)|^2 = \exp\left(-\frac{q^2 R^2}{3\hbar^2}\right) = \exp\left(-\frac{\Delta E}{E_0}\right). \quad (5.4)$$

Here $R \sim \left[0.91 \left(\frac{m_A}{\text{GeV}}\right)^{1/3} + 0.3\right] \times 10^{-13}$ cm is the nuclear radius and $E_0 \equiv 3\hbar^2/(2m_A R^2)$ is the characteristic nuclear coherence energy, m_A being the mass of the nucleus and $\Delta E = \frac{q^2}{2m}$ is the WIMP energy loss.

The spin dependent cross section can be written as,

$$\sigma_{\chi A}^{\text{SD}}(q) = \frac{\mu_{\chi A}^2}{\mu_{\chi p}^2} \sigma_{\chi p}^{\text{SD}} A^2 C J(J+1), \quad (5.5)$$

where C is a factor that depends on the details of nuclear structure and J is the total angular momentum of nucleus. The values of C and J for different nuclei can be found in [2, 255, 256, 257, 258].

For the spin-dependent (SD) WIMP-proton cross-section, Hydrogen is the most abundant element in the Sun and we can neglect the heavier elements in this case. We consider spin independent elastic scattering with $\sigma_{\chi H}^{\text{SI}} = \sigma_{\chi p}^{\text{SI}}$ and $\sigma_{\chi \text{He}}^{\text{SI}} = 16\sigma_{\chi p}^{\text{SI}}$ and spin dependent scattering with $\sigma_{\chi H}^{\text{SD}} = \sigma_{\chi p}^{\text{SD}}$ and $\sigma_{\chi \text{He}}^{\text{SD}} = 0$ (we neglect the tiny contribution from spin-dependent scattering from 3He). In Sun we mainly have Hydrogen ($\sim 71\%$) and Helium ($\sim 27\%$). For Hydrogen we see there is no need to introduce form factor but for Helium we need to take it into account.

With the above form of the nuclear form factor, the kinematics of the capture process [253] allows us to write the capture probability per unit time, $\Omega^-(w)$, as given below,

$$\begin{aligned} \Omega^-(w) &= (n_A \sigma_{\chi A} w) \int_{\frac{u^2}{w^2}}^{\frac{\mu}{\mu_+}} \frac{\mu_+^2}{\mu} \exp\left(-\frac{\Delta E}{E_0}\right) d\left(\frac{\Delta E}{m_\chi w^2/2}\right) \Theta\left(\frac{\mu}{\mu_+^2} - \frac{u^2}{w^2}\right) \\ &= \frac{n_A \sigma_{\chi A}}{w} \frac{2E_0}{m_\chi} \frac{\mu_+^2}{\mu} \left[\exp\left(-\frac{m_\chi u^2}{2E_0}\right) - \exp\left(-\frac{m_\chi w^2}{2E_0} \frac{\mu}{\mu_+}\right) \right] \Theta\left(\frac{\mu}{\mu_+^2} - \frac{u^2}{w^2}\right), \end{aligned} \quad (5.6)$$

where n_A is the number density of the scattering nuclei at the radius r inside the Sun, and $\mu \equiv \frac{m_\chi}{m_A}$, $\mu_\pm \equiv \frac{\mu \pm 1}{2}$. The Θ function ensures that those particles which do not lose sufficient amount of energy to be captured are excluded.

We shall use Equation (5.6) to calculate $\Omega^-(w)$ for helium ($A = 4$). For hydrogen, however, there is no form-factor suppression, and the expression for $\Omega^-(w)$ is simpler:

$$\text{Hydrogen :} \quad \Omega^-(w) = \frac{\sigma_{\chi p} n_H}{w} \left(w_{\text{esc}}^2 - \frac{\mu_-^2}{\mu} u^2 \right) \theta \left(w_{\text{esc}}^2 - \frac{\mu_-^2}{\mu} u^2 \right), \quad (5.7)$$

where n_H is the density of hydrogen (proton) at the radius r inside the Sun. Note that in equations (5.6) and (5.7), the quantities w , w_{esc} , n_A and n_H are functions of r .

The WIMP velocity distribution appearing in equation (5.1) is related to the phase space distribution functions as described in Chapter II and Chapter IV (valid in the rest frame of Galaxy) by the Galilean transformation,

$$\tilde{f}(\mathbf{u}) = \frac{1}{m_\chi} f(\mathbf{x} = \mathbf{x}_\odot, \mathbf{v} = \mathbf{u} + \mathbf{v}_\odot), \quad (5.8)$$

where \mathbf{x}_\odot represents the sun's position in the Galaxy ($R = 8.5 \text{ kpc}, z = 0$) and \mathbf{v}_\odot is the Sun's velocity vector in the Galaxy's rest frame. Gould's calculations and the final formula for the WIMP capture rate given in Ref. [253], which are widely adopted in the literature, use a Maxwellian velocity distribution of the WIMPs in the Galaxy, and as such, cannot directly be used here since the WIMP velocity distribution in our case is non-Maxwellian. In particular, the VDF used here vanishes for speeds greater than v_{max} and consequently, equation (5.1) above can be written as,

$$\frac{dC}{dV}(r) = \frac{2\pi}{m_\chi} \int_{-1}^1 d(\cos \theta) \int_{u_{\min}=v_\odot}^{u_{\max}(\cos \theta)} u du f(\mathbf{x} = \mathbf{x}_\odot, \mathbf{v} = \mathbf{u} + \mathbf{v}_\odot) w \Omega^-(w), \quad (5.9)$$

where $v_\odot \approx 220 - 250 \text{ km s}^{-1}$ is the Sun's circular speed in the Galaxy, and u_{max} is given by the positive root of the quadratic equation

$$u_{\text{max}}^2 + v_\odot^2 + 2u_{\text{max}} v_\odot \cos \theta = v_{\text{max}}^2. \quad (5.10)$$

The total WIMP capture rate by the Sun, C_\odot , is given by

$$C_\odot = \int_0^{R_{\text{sun}}} 4\pi r^2 dr \frac{dC(r)}{dV}, \quad (5.11)$$

where R_{sun} is the radius of the Sun.

5.3 Calculation of Annihilation Rate

WIMPs that are accumulated in Sun by gravitational capture are depleted by annihilation with anti-WIMPs and also evaporation. Now the evolution of the number of WIMPs (N) with time, in Sun, is given by the following differential equation:

$$\frac{dN}{dt} = C_{\odot} - A_{\odot}N^2 - E_{\odot}N, \quad (5.12)$$

where $A_{\odot} = \frac{\langle \sigma_{ann}v \rangle}{V_{\text{eff}}}$ is velocity averaged WIMP self annihilation cross section per unit volume and V_{eff} is the effective core volume of the Sun which can be roughly estimated by matching the core temperature with the gravitational potential energy of a single WIMP at the core radius. The quantity $1/V_{\text{eff}}$ is given by V_2/V_1^2 [253, 259, 2, 149] with $V_j = 4\pi \int_0^{\mathcal{R}} r^2 \exp\left(-\frac{jm_{\chi}\phi}{T_c}\right)$ where $\phi = \int_0^r dr \frac{GM(r)}{r^2}$ is the gravitational potential with respect to the core and $M(r)$ is the mass within core. Evaluating this we get,

$$V_j = \left(\frac{3k_B T_c}{2jGm_{\chi}\rho_c} \right)^{\frac{3}{2}} = 6.5 \times 10^{28} \left(\frac{jm_{\chi}}{10 \text{ GeV}} \right)^{-\frac{3}{2}}, \quad (5.13)$$

where $T_c = 1.4 \times 10^7 \text{ K}$ and $\rho_c = 150 \text{ gm/cc}$ are core temperature and core density of Sun respectively. Finally we get,

$$V_{\text{eff}} = \frac{V_1^2}{V_2} = \sqrt{8}V_1 = 5.8138 \times 10^{30} \left(\frac{1 \text{ GeV}}{m_{\chi}} \right)^{\frac{3}{2}} \text{ cm}^3. \quad (5.14)$$

Now, it is possible that WIMPs once captured might diffuse away i.e. evaporate from the Sun by hard elastic scattering from the nuclei. E_{\odot} defines the inverse time scale for WIMPs to evaporate from Sun. An approximate expression for E_{\odot} is calculated in Ref. [252], [259], [149].

$$E_{\odot} \approx 10^{-(3.5(\frac{m_{\chi}}{\text{GeV}})+4)} \text{ s}^{-1} \quad (5.15)$$

Here we shall neglect the evaporation effect as it is important for WIMP masses lower than 4 GeV. Therefore solving equation (5.12) for N , neglecting evaporation we get,

$$N = \sqrt{\frac{C_{\odot}}{A_{\odot}}} [\tanh(t/\tau_E)] , \quad (5.16)$$

So, the WIMP annihilation rate Γ_{\odot} at present time is given by,

$$\Gamma_{\odot} = \frac{1}{2} A_{\odot} N^2 = \frac{1}{2} C_{\odot} [\tanh(t_{\odot}/\tau_E)]^2 , \quad (5.17)$$

where $t_{\odot} \sim 4.2$ billion years is the age of the Sun and $\tau_E = (C_{\odot} A_{\odot})^{-1/2}$ is the characteristic time to reach equilibrium between capture and annihilation. So, when $t_{\odot}/\tau_E \gg 1$, which is a posteriori true for Sun we expect, equilibrium is reached and annihilation rate is maximum. Therefore, we make here the standard assumption that the capture and annihilation processes have reached an approximate equilibrium state over the long lifetime of the solar system ($t_{\odot} \sim 4.2$ billion yrs). Under this assumption, the total annihilation rate of WIMPs in the Sun is simply related to the total capture rate by the relation

$$\Gamma_{\odot} \approx \frac{1}{2} C_{\odot} \quad (5.18)$$

Because of this assumption the annihilation cross section σ_{ann} disappears from the model and the only cross section we are concerned with is the WIMP nucleon elastic scattering cross section. This allows us to present our results in terms of exclusion plots in the WIMP parameter space and hence compare with the direct detection experimental finding of the WIMP nucleon scattering cross section.

5.4 The self-consistent King Model

The expected flux of neutrinos from the Sun due to WIMP annihilations depends on the rate at which WIMPs are captured by the Sun. The capture rate depends on the density as well as the velocity distribution of the WIMPs in the solar neighborhood as the Sun goes around the Galaxy. The density and velocity distribution of the WIMPs in the Galaxy are *a priori* unknown. Most earlier studies of neutrinos from WIMP capture and annihilation in the Sun have been done within the context of the so-called “Standard Halo Model” (SHM) in which the DM halo of the Galaxy is described by a single component isothermal sphere [133] with a isotropic Maxwellian velocity distribution of the DM particles in the Galactic rest frame [260, 2, 257]) as described in Chapter II.

The SHM has a few shortcomings as described in Chapter II therefore here in this chapter the model of the phase space structure of the finite-size DM halo of the Galaxy adopted is based on the so-called “lowered” (or truncated) isothermal model (often called “King model”) [133, 146] of the phase-space distribution function (DF) of collisionless particles. This model is basically the isotropic version of the “Michie model” as discussed Chapter IV (in the limit anisotropic radius approaching a very large value i.e. $r_a \rightarrow \infty$). The model is a proper self-consistent solutions of the collisionless Boltzmann Equation (CBE) representing nearly isothermal systems of finite physical size and mass. There are two important features of this model: First, at every location within the system a DM particle can have speeds up to a maximum speed which is self-consistently determined by the model itself. A particle of maximum velocity at any location within the system can just reach its outer boundary, fixed by the truncation radius, a parameter of the model, where the DM density by construction vanishes. Second, the speed distribution of the particles constituting the system is non-Maxwellian. To include the gravitational effect of the

observed visible matter on the DM particles, we modify the “pure” King model DF by replacing the gravitational potential appearing in the King model DF by the total gravitational potential consisting of the sum of those due to DM and the observed visible matter. This interaction with the visible matter influences both the density profile and the velocity distribution of the dark matter particles as compared to those for a “pure” King model. In particular, the dark matter is pulled in by the visible matter, thereby increasing its central density significantly. When the visible matter density is set to zero and the truncation radius is set to infinity, our halo model becomes identical to that of a single-component isothermal sphere used in the SHM. For further discussion of the model, see [170, 155].

The DM distribution in the Galaxy may have significant amount of substructures which may have interesting effects on the WIMP capture and annihilation rates [261]. However, not much information, based on observational data, is available about the spatial distribution and internal structures of these substructures. As such, in this chapter we shall be concerned only with the smooth component of the DM distribution in the Galaxy described by the self-consistent model mentioned above, the parameters of which are determined from the observed rotation curve data for the Galaxy.

The non-Maxwellian nature of the WIMP speed distribution in the halo model makes the calculation of the WIMP capture (and consequently annihilation) rate non-trivial since the standard analytical formula for the capture rate given by Gould [253] and Press and Spergel [251], which is widely used in the literature, is not valid for the non-Maxwellian speed distribution in our halo model, and as such has to be calculated *ab initio* as described in previous section.

The phase space distribution function (PSDF) of the DM particles constituting a truncated isothermal halo of the Galaxy can be taken, in the rest frame of the

Galaxy, to be of the “King model” form [133, 170, 155] which is isotropic extension of the “Michie Model”,

$$f(\mathbf{x}, \mathbf{v}) \equiv f(\mathcal{E}) = \begin{cases} \rho_1 (2\pi\sigma^2)^{-3/2} \left(e^{\mathcal{E}/\sigma^2} - 1 \right) & \text{for } \mathcal{E} > 0, \\ 0 & \text{for } \mathcal{E} \leq 0, \end{cases} \quad (5.19)$$

$$\text{where } \mathcal{E}(\mathbf{x}) \equiv \Phi(r_t) - \left(\frac{1}{2}v^2 + \Phi(\mathbf{x}) \right) \equiv \Psi(\mathbf{x}) - \frac{1}{2}v^2, \quad (5.20)$$

is the so-called “relative energy” and $\Psi(\mathbf{x}) = -\Phi(\mathbf{x}) + \Phi(r_t)$ the “relative potential”, $\Phi(\mathbf{x})$ being the total gravitational potential under which the particles move, with boundary condition $\Phi(0) = 0$. The relative potential and relative energy, by construction, vanish at $|\mathbf{x}| = r_t$, the truncation radius, which represents the outer edge of the system where the particle density vanishes. At any location \mathbf{x} the maximum speed a particle of the system can have is,

$$v_{\max}(\mathbf{x}) = \sqrt{2\Psi(\mathbf{x})}, \quad (5.21)$$

at which the relative energy \mathcal{E} and, as a consequence, the PSDF (5.19), vanish. The model has three parameters, namely, ρ_1 , σ and r_t . Note that the parameter σ in the King model is not same as the usual velocity dispersion parameter of the isothermal PSDF [133]. The parameter r_t represents the truncation radius, i.e. extent of the halo. Also, we shall present our results in terms of the local dark matter density $\rho_{\text{DM},\odot}$, in place of the parameter ρ_1 .

Integration of $f(\mathbf{x}, \mathbf{v})$ over all velocities gives the DM density at the position \mathbf{x} :

$$\rho_{\text{DM}}(\mathbf{x}) = \frac{\rho_1}{(2\pi\sigma^2)^{3/2}} \int_0^{\sqrt{2\Psi(\mathbf{x})}} dv 4\pi v^2 \left[\exp\left(\frac{\Psi(\mathbf{x}) - v^2/2}{\sigma^2}\right) - 1 \right] \quad (5.22)$$

$$= \rho_1 \left[\exp\left(\frac{\Psi(\mathbf{x})}{\sigma^2}\right) \operatorname{erf}\left(\frac{\sqrt{\Psi(\mathbf{x})}}{\sigma}\right) - \sqrt{\frac{4\Psi(\mathbf{x})}{\pi\sigma^2}} \left(1 + \frac{2\Psi(\mathbf{x})}{3\sigma^2}\right) \right] \quad (5.23)$$

which satisfies the Poisson equation

$$\nabla^2 \Phi_{\text{DM}}(\mathbf{x}) = 4\pi G \rho_{\text{DM}}(\mathbf{x}), \quad (5.24)$$

where Φ_{DM} is the contribution of the DM component to the total gravitational potential,

$$\Phi(\mathbf{x}) = \Phi_{\text{DM}}(\mathbf{x}) + \Phi_{\text{VM}}(\mathbf{x}), \quad (5.25)$$

in presence of the visible matter (VM) whose gravitational potential, Φ_{VM} , satisfies its own Poisson equation, namely,

$$\nabla^2 \Phi_{\text{VM}}(\mathbf{x}) = 4\pi G \rho_{\text{VM}}(\mathbf{x}). \quad (5.26)$$

We choose the boundary conditions

$$\Phi_{\text{DM}}(0) = \Phi_{\text{VM}}(0) = 0, \quad \text{and} \quad (\nabla \Phi_{\text{DM}})_{|\mathbf{x}|=0} = (\nabla \Phi_{\text{VM}})_{|\mathbf{x}|=0} = 0. \quad (5.27)$$

The mass of the system, defined as the total mass contained within r_t , is given by $GM(r_t)/r_t = [\Phi(\infty) - \Phi(r_t)]$. Note that, because of the chosen boundary condition $\Phi(0) = 0$, $\Phi(\infty)$ is a non-zero positive constant.

In practice a test particle can sense the gravitational potential of both the DM and VM. Therefore the system is coupled and the coupled Poisson's equation can be solved in an iterative manner until the system converges by including the effect of the VM in a self-consistent manner as also described in Chapter IV. Since the visible matter distribution $\rho_{\text{VM}}(\mathbf{x})$, and hence the potential $\Phi_{\text{VM}}(\mathbf{x})$, are known from observations and modeling, the solutions of equation (5.24) together with equations (5.23), (5.25) and the boundary conditions (5.27), give us a three-parameter family of self-consistent pairs of $\rho_{\text{DM}}(\mathbf{x})$ and $\Phi_{\text{DM}}(\mathbf{x})$ for chosen values of the parameters (ρ_1, σ, r_t) . The values of these parameters for the Galaxy can be determined by

comparing the theoretically calculated rotation curve, $v_c(R)$, given by,

$$v_c^2(R) = R \frac{\partial}{\partial R} [\Phi(R, z = 0)] = R \frac{\partial}{\partial R} [\Phi_{\text{DM}}(R, z = 0) + \Phi_{\text{VM}}(R, z = 0)], \quad (5.28)$$

with the observed rotation curve data of the Galaxy. Here R is Galactocentric distance on the equatorial plane and z is the distance normal to the equatorial plane. This procedure was described in detail in Refs. [170, 155].

5.5 Results Using King Model

The visible matter model is described by a superposition of a spherical bulge and double exponential disk same as that adopted in chapter IV for Michie models [155], [232], [233], [234]. The forms are given below:

Bulge:

$$\rho_{\text{bulge}} = \rho_{b,0} \frac{1}{[1 + (r/r_b)^2]^{3/2}}, \quad (5.29)$$

Disk:

$$\rho_{\text{disk}} = \frac{\Sigma_{\text{VM}}}{2z_d} \exp \left[-\frac{(R - R_\odot)}{r_d} \right] \exp[-z/z_d], \quad (5.30)$$

with the following parameter values : central bulge density ($\rho_{b,0}$) = $4.2 \times 10^2 M_\odot / pc^3$, bulge scale radius (r_b) = 0.103 kpc, disk scale length (r_d) = 3 kpc , disk scale height (z_d) = 0.3 kpc and the local visible matter surface density (Σ_{VM}) = $48 M_\odot / pc^2$.

Thereafter we determined the values of the parameters r_t and σ that gave reasonably good fit to the rotation curve data of the Galaxy [262, 263] standardized at the IAU recommended values of the Galactic constants namely Galactocentric distance of Sun and the circular velocity at Sun's location as [8.5 kpc, 220 km s^{-1}] for each of

the three chosen values of the parameter ρ_1 conveniently recast in terms of the local dark matter density $\rho_{\text{DM},\odot} = 0.2, 0.3$ and 0.4 GeV/cm^3 .

Model	$\rho_{\text{DM},\odot}$ (GeV cm^{-3})	r_t (kpc)	σ (km s^{-1})
M1	0.2	120.0	300.0
M2	0.3	80.0	400.0
M3	0.4	80.0	300.0

Table 5.1: Parameters of our self-consistent model of the Milky Way’s Dark Matter halo that give good fits to the Galaxy’s rotation curve data, for the three chosen values of the DM density at the solar neighborhood.

The best fit models, namely M1, M2, M3, are summarized in Table 5.1, which we use for our calculations in this chapter. In Figure 5.1 we present the fit to the RC data for three models namely M1, M2 and M3, in the left panel and in the right panel of the same figure we present separately the contributions from the visible matter and dark matter for model M1 only. Next in left panel of Figure 5.2 we present the density distribution of visible matter and dark matter in equatorial plane and vertical direction. As a result of coupling the DM core density is increased and core radius is shortened due to the gravitational pull of the visible matter. The DM density at disk region is also enhanced by around (15 – 20)%. In the right panel of the same figure we show the total mass plot for visible matter and dark matter separately. Both the plots are made for the model M1. In Figure 5.3 we show the v_{max} in the left panel and in right panel we present the normalized velocity distribution for the three models and the SHM together. The VDFs resulting from the King model are sharply truncated at high velocity as compared to the long tail of the Maxwellian VDF of the SHM. This will have effect on both the direct and indirect detection results. The results are discussed in detail in Ref. [155, 156].

Figure 5.4 shows the dependence of the capture rate of WIMPs by the Sun as a function of the WIMP’s mass for the three halo models specified in Table 5.1. As expected, for a given DM density, the capture rate decreases as WIMP mass

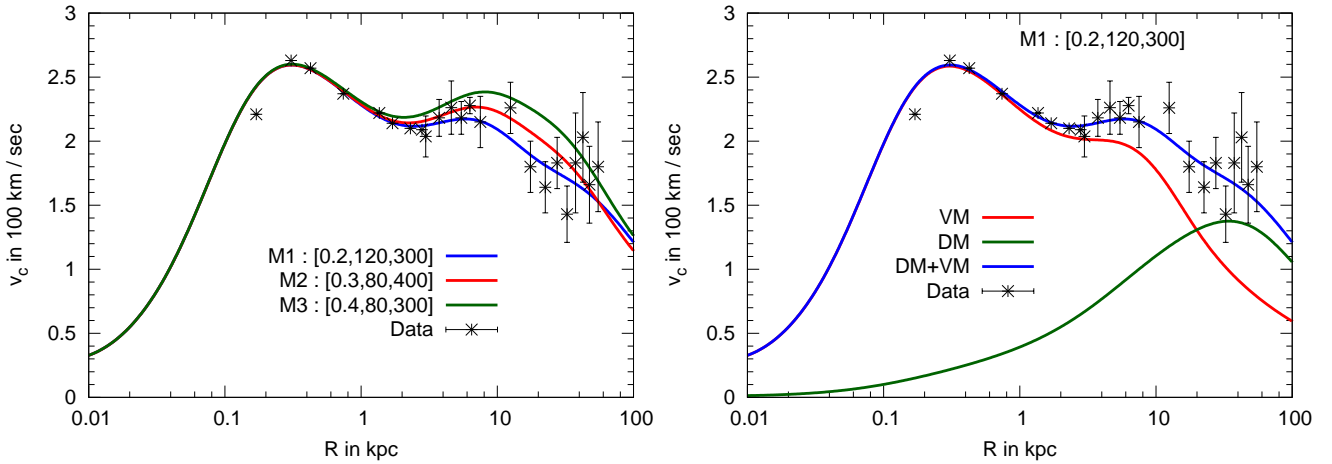


Figure 5.1: Left: Rotation curve data and fit for three models, namely M1, M2, M3, as described in Table 5.1. Right: Rotation curve fit for the model M1 only. Contributions from visible and dark matter are shown separately here.

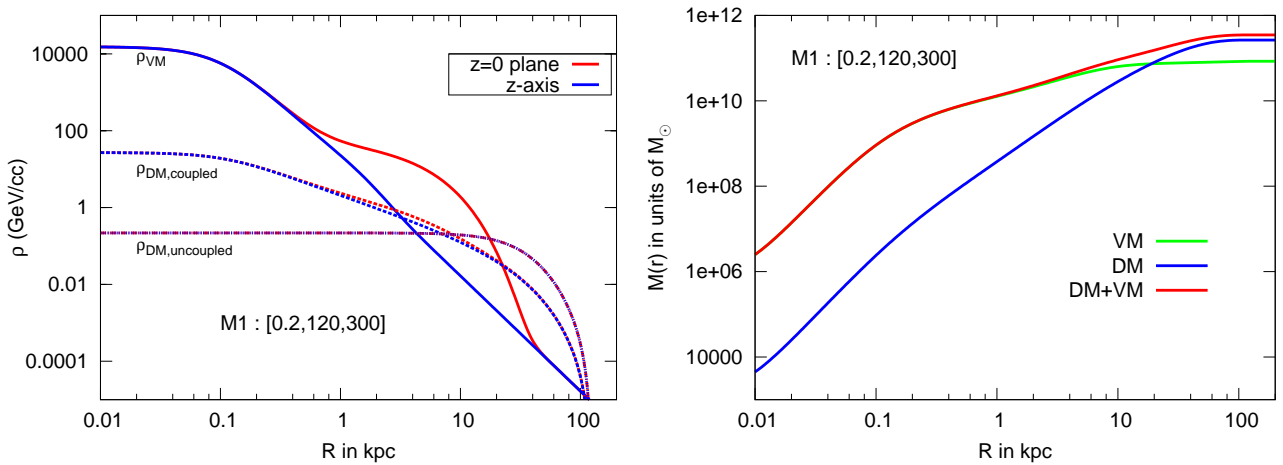


Figure 5.2: Left: Density distribution for the visible matter and the dark matter (model M1 only). The plots are given for both couple and uncoupled case as discussed in the text. In the coupled case it is evident that the core density is increased and the core radius is shortened. There is enhancement in the disk region as well. Right: Mass distribution for the M1 model separately shown for visible and dark matter.

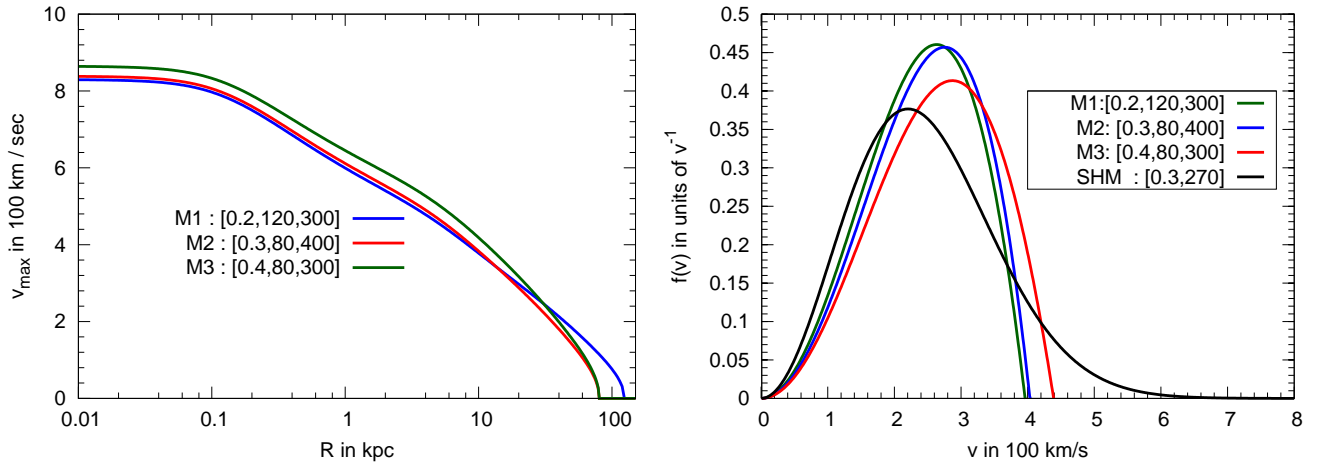


Figure 5.3: Left: Maximum velocity v_{\max} distribution for all the three models, namely M1, M2 and M3. Right: Velocity distributions at solar location for the three models along with the Maxwellian distribution of SHM. The plot shows that the distributions arising from the King model are sharply truncated at higher velocity end whereas the Maxwellian distribution has a long high velocity tail.

increases because heavier WIMPs correspond to smaller number density of WIMPs hence smaller capture rates.

5.6 Summary

In this chapter we have discussed the techniques of calculating the capture rate of WIMPs in the Sun for any given velocity distribution. We have made the standard assumption that over long life-time of the Sun the capture and annihilation rate within the Sun has reached an equilibrium. This allows us to eliminate the annihilation cross section σ_{ann} from the system and we are left with the scattering cross section only and therefore we can compare our limits with that of the direct detection scenario. We have done the calculations of the capture rate in context of a self-consistent King model. The King model is basically a lowered isothermal model that has finite limits in both configuration and velocity space determined self consistently by the model itself and thus overcomes the shortcomings of the so called SHM. We have also included the gravitational effect of the visible matter in

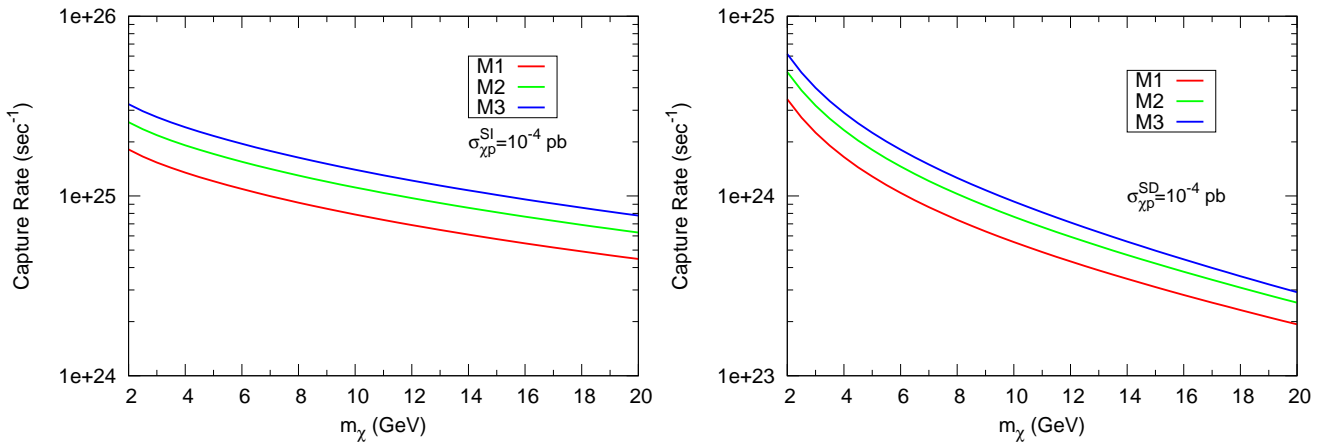


Figure 5.4: The capture rate as a function of the WIMP mass for the three halo models specified in Table 5.1, and for spin-independent (SI: left panel) and spin-dependent (SD: right panel) WIMP- proton interactions. All the curves are for a reference value of the WIMP-proton elastic SI or SD cross section of 10^{-4} pb.

the system in a self consistent manner. As an effect of which the DM core density is enhanced and the core radius is decreased. For a representative value of the scattering cross section (10^{-4} pb) for both spin dependent and independent we have found the capture rates as function of the WIMP mass. We will use these results in next chapter to calculate the event rates for the Super-Kamiokande detector and hence derive upper limits on the branching fractions on various WIMP annihilation channels.

Chapter 6

Indirect detection of WIMPs : Neutrino flux and exclusion plots

6.1 Introduction

In the previous chapter we have calculated the capture rate of WIMPs in the Sun within the context of a self-consistent model of finite sized DM halo of the Galaxy, namely, the King model, including the gravitational effect of the observed visible matter on the DM. The parameters of the model are determined by performing fit to the observed rotation curve data of the Galaxy. In the present chapter we use the results of the previous chapter to calculate the expected neutrino flux from the Sun due to annihilation of WIMPs captured and accumulated inside the Sun, and derive constraints on the WIMP- nucleon elastic scattering cross section from the upper limits on the flux of such neutrinos given by the Super-Kamiokande experiment [147]. Further combining the resulting constraint on the WIMP-nucleon elastic scattering cross section with those obtained from the analysis of direct detection experiments [155], within the context of the same “King model”, we obtain restrictions on the

branching fractions of the relevant WIMP annihilation channels. There are many works in the literature on the calculations of the expected neutrino fluxes from WIMP capture and annihilation in the Sun and the Earth [264, 265, 266, 267, 268, 269, 270, 271, 272, 273, 274, 275].

This chapter is organized as follows: In Section 6.2 we present the neutrino flux from different annihilation channels. In Section 6.3 we calculate the expected event rates of neutrinos in the Super-Kamiokande detector and in Sections 6.4 and 6.5 we derive the upper limits on the WIMP-nucleon elastic scattering cross section from the non-detection of such neutrinos by S-K detector. In these sections we also discuss the resulting constraints on the branching fraction of various WIMP annihilation channels obtained by demanding the compatibility of the S-K induced upper limits with that of the direct detection experiments. Finally in Section 6.6 we summarize the main results obtained in this chapter.

6.2 Neutrino Flux from Different Annihilation Channels

In this section we present the results for the energy spectra of neutrinos emerging from the Sun, for various WIMP annihilation channels [269, 276, 267, 268], which we will use in the calculation of event rate at a given neutrino detector described in the next section.

The differential flux of muon neutrinos observed at Earth is [269] given by,

$$\left(\frac{d\phi_i}{dE_i}\right) = \frac{\Gamma_{\odot}}{4\pi D^2} \sum_F B_F \left(\frac{dN_i}{dE_i}\right)_F, \quad (i = \nu_{\mu}, \bar{\nu}_{\mu}) \quad (6.1)$$

where Γ_{\odot} is the rate of WIMP annihilation in the Sun, D is the Earth-Sun distance,

F stands for the possible annihilation channels, B_F is the branching ratio for the annihilation channel F and $\left(\frac{dN_i}{dE_i}\right)_F$ is the differential energy spectrum of the neutrinos of type i emerging from the Sun resulting from the particles of annihilation channel F injected at the core of the Sun. WIMPs can annihilate to all possible standard model particles e.g. e^+e^- , $\mu^+\mu^-$, $\tau^+\tau^-$, $\nu_e\bar{\nu}_e$, $\nu_\mu\bar{\nu}_\mu$, $\nu_\tau\bar{\nu}_\tau$, $\bar{q}q$ pairs and also gauge and higgs boson pairs (W^+W^- , $Z\bar{Z}$, $h\bar{h}$), etc. In this chapter we are only interested in low mass (~ 20 GeV) WIMPs. Therefore, we will not consider WIMP annihilations to higgs and gauge boson pairs and top quark pairs. Light quarks like u , d , s contribute very little to the energetic neutrino flux [276], and are not considered. The same is true for muons. So, in this chapter we consider only the channels $\tau^+\tau^-$, $\bar{b}b$, $\bar{c}c$ and $\bar{\nu}\nu$.

The neutrino energy spectra, $\left(\frac{dN_i}{dE_i}\right)_F$, have been calculated numerically (see, e.g., [276, 277]) by considering all the details of hadronization of quarks, energy loss of the resulting heavy hadrons, neutrino oscillation effects, neutrino energy loss due to neutral current interactions and absorption due to charged current interactions with the solar medium, ν_τ regeneration, etc. However, the numerical results in Refs. [276, 277] are given for WIMP masses $m_\chi \geq 10$ GeV, and it is not obvious if those are valid for lower WIMP masses which are of our primary interest in this chapter. In any case, given the presence of other uncertainties in the problem, particularly those associated with astrophysical quantities such as the local density of dark matter and its velocity distribution, we argue that it is good enough to use — as we do in this chapter — approximate analytical expressions for the neutrino spectra available in the literature [269, 267, 268]. We are interested in the fluxes of muon neutrinos and antineutrinos, for which we use the analytic expressions given in Ref. [269], which neglect neutrino oscillation effects. By comparing with the neutrino fluxes obtained from detailed numerical calculations [276], we find that for small WIMP masses below ~ 20 GeV (the masses of our interest in this chapter), the analytic expressions for the muon neutrino fluxes given in [269] match with the results of

detailed numerical calculations [276] to within a few percent.

The main effect of the interaction of the neutrinos with the solar medium is that [268] a neutrino of type i ($= \nu_\mu, \bar{\nu}_\mu$) injected at the solar core with energy E_i^{core} emerges from the Sun with an energy E_i given by

$$E_i^{\text{core}} = E_i / (1 - E_i \tau_i), \quad (6.2)$$

and with probability

$$P_i = (1 + E_i^{\text{core}} \tau_i)^{-\alpha_i} = (1 - E_i \tau_i)^{\alpha_i}, \quad (6.3)$$

with

$$\alpha_{\nu_\mu} = 5.1, \quad \alpha_{\bar{\nu}_\mu} = 9.0, \quad \tau_{\nu_\mu} = 1.01 \times 10^{-3} \text{ GeV}^{-1}, \quad \text{and} \quad \tau_{\bar{\nu}_\mu} = 3.8 \times 10^{-4} \text{ GeV}^{-1}. \quad (6.4)$$

Below we present the expressions for the energy spectra of neutrinos emerging from the Sun for the four annihilation channels considered in this chapter.

6.2.1 $\tau^+ \tau^-$ channel : Neutrinos from decay of τ leptons

$$(\tau \rightarrow \mu \nu_\mu \nu_\tau)$$

For this channel, the spectrum of muon-type neutrinos at the solar surface, including the propagation effects in the solar medium, can be written as [269]

$$\left(\frac{dN_i}{dE_i} \right)_{\tau^+ \tau^-} = (1 - E_i \tau_i)^{(\alpha_i - 2)} \left(\frac{dN_i^{\text{core}}}{dE_i^{\text{core}}} \right)_{\tau^+ \tau^-}, \quad (i = \nu_\mu, \bar{\nu}_\mu) \quad (6.5)$$

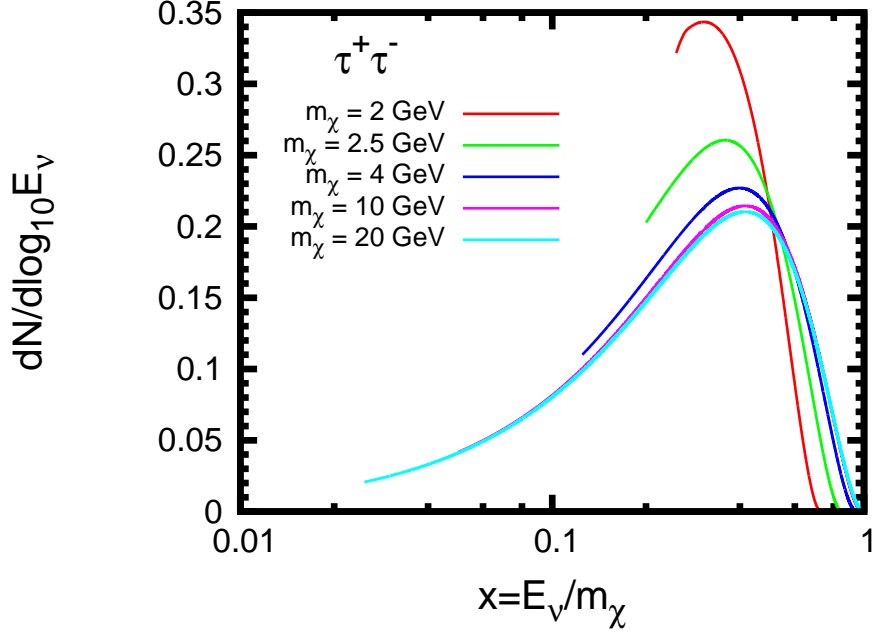


Figure 6.1: Neutrino spectra for a few representative WIMP masses for $\tau^+\tau^-$ annihilation channel.

where the relationship between E_i and E_i^{core} , and the values of α_i and τ_i , are as given by equations (6.2) and (6.4), respectively, and

$$\left(\frac{dN_i^{\text{core}}}{dE_i^{\text{core}}}\right)_{\tau^+\tau^-} = \frac{48 \Gamma_{\tau \rightarrow \mu\nu\mu\nu\tau}}{\beta\gamma m_\tau^4} \left(\frac{1}{2}m_\tau (E_i^{\text{core}})^2 - \frac{2}{3}(E_i^{\text{core}})^3\right)_{E_-}^{\min(\frac{1}{2}m_\tau, E_+)} \quad (6.6)$$

is the neutrino spectrum due to decay of the τ -leptons injected at the solar core by WIMP annihilations. Here $\Gamma_{\tau \rightarrow \mu\nu\mu\nu\tau} = 0.18$, and $E_\pm = \frac{E_i^{\text{core}}}{\gamma(1 \mp \beta)}$ with $\gamma = (1 - \beta^2)^{-1/2} = m_\chi/m_\tau$, m_τ being the τ -lepton mass and m_χ is the WIMP mass.

Note that the ν_τ s produced from τ decay may again produce τ s by charged current interactions in the solar medium, and these secondary τ s can decay to give secondary ν_μ s. But these ν_μ s would be of much lower energy compared to the primary ν_μ s from τ decay, and are not considered here. The ν_μ spectra from $\tau^+\tau^-$ annihilation channel for several values of WIMP masses as shown in Figure 6.1.

6.2.2 $\bar{b}b$ channel : Neutrinos from decay of b -quark hadrons

$$(b \rightarrow c\mu\nu_\mu)$$

The treatment is similar to the case of τ decay described above. However, here the hadronization of quarks and stopping of heavy hadrons in the solar medium have to be taken into account. The resulting spectrum of muon-neutrinos emerging from the Sun is given by [269]

$$\left(\frac{dN_i}{dE_i}\right)_{\bar{b}b} = \int_{m_b}^{E_0} \left(\frac{1}{N} \frac{dN}{dE_d}\right)^{\text{hadron}}(E_0, E_d) (1 - E_i\tau_i)^{(\alpha_i-2)} \left(\frac{dN_i^{\text{core}}}{dE_i^{\text{core}}}\right)_{\bar{b}b}(E_d, E_i^{\text{core}}) dE_d, \quad (i = \nu_\mu, \bar{\nu}_\mu) \quad (6.7)$$

where m_b is the b -quark mass, $E_0 \approx 0.71m_\chi$ is the initial energy of the b -quark hadron (the fragmentation function is assumed to be a sharply peaked function [269]),

$$\left(\frac{dN_i^{\text{core}}}{dE_i^{\text{core}}}\right)_{\bar{b}b}(E_d, E_i^{\text{core}}) = \frac{48 \Gamma_{b \rightarrow \mu\nu_\mu X}}{\beta\gamma m_b^4} \left(\frac{1}{2}m_b (E_i^{\text{core}})^2 - \frac{2}{3} (E_i^{\text{core}})^3\right)_{E_-}^{\min(\frac{1}{2}m_b, E_+)} \quad (6.8)$$

is the neutrino spectrum resulting from decay of the b -quark hadron injected at the solar core, and

$$\left(\frac{1}{N} \frac{dN}{dE_d}\right)^{\text{hadron}}(E_0, E_d) = \frac{E_c}{E_d^2} \exp\left[\frac{E_c}{E_0} - \frac{E_c}{E_d}\right], \quad (6.9)$$

with $E_c \approx 470$ GeV, is the distribution of the hadron's energy at the time of its decay if it is produced with an initial energy E_0 . In equation (6.8), $\Gamma_{b \rightarrow \mu\nu_\mu X} = 0.103$ is the branching ratio for inclusive semi-leptonic decay of b -quark hadrons to muons [278], and $E_\pm = \frac{E_i^{\text{core}}}{\gamma(1 \mp \beta)}$ with $\gamma = (1 - \beta^2)^{-1/2} = E_d/m_b$.

The ν_μ spectra from $\bar{b}b$ annihilation channel for several values of WIMP masses as shown in Figure 6.2.

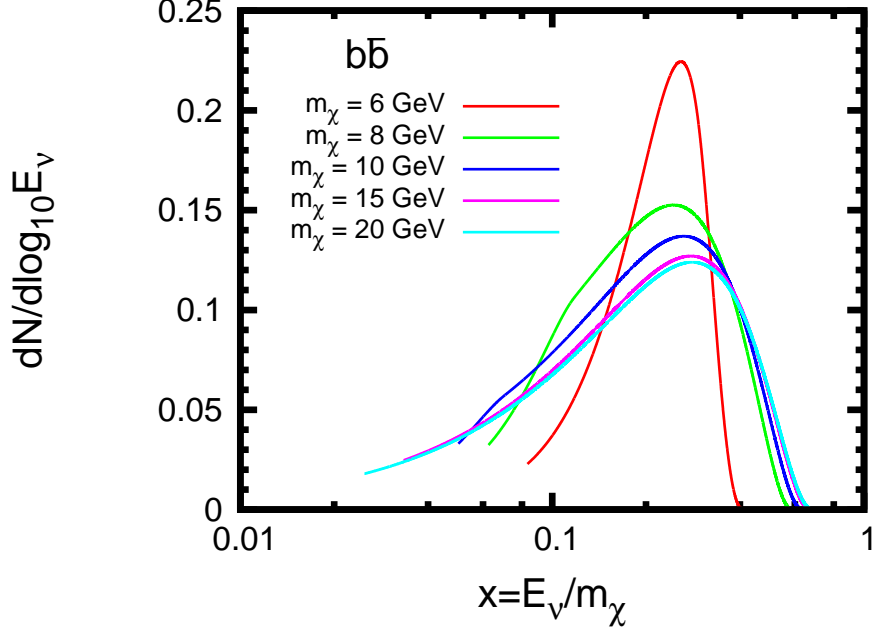


Figure 6.2: Neutrino spectra for a few representative WIMP masses for $\bar{b}b$ annihilation channel.

6.2.3 $\bar{c}c$ channel : Neutrinos from decay of c -quark hadrons

$$(c \rightarrow s\mu\nu_\mu)$$

Again, this is similar to the case of b -decay discussed above, except that the kinematics of the process is slightly different. The resulting muon neutrino spectrum is given by [269]

$$\left(\frac{dN_i}{dE_i}\right)_{\bar{c}c} = \int_{m_c}^{E_0} \left(\frac{1}{N} \frac{dN}{dE_d}\right)^{\text{hadron}}(E_0, E_d) (1 - E_i\tau_i)^{(\alpha_i-2)} \left(\frac{dN_i^{\text{core}}}{dE_i^{\text{core}}}\right)_{\bar{c}c}(E_d, E_i^{\text{core}}) dE_d, \quad (i = \nu_\mu, \bar{\nu}_\mu) \quad (6.10)$$

where m_c is the c -quark mass, $E_0 \approx 0.55m_\chi$ is the initial energy of the charmed hadron,

$$\left(\frac{dN_i^{\text{core}}}{dE_i^{\text{core}}}\right)_{\bar{c}c}(E_d, E_i^{\text{core}}) = \frac{8\Gamma_{c \rightarrow \mu\nu_\mu X}}{\beta\gamma m_c^4} \left(\frac{3}{2}m_c(E_i^{\text{core}})^2 - \frac{4}{3}(E_i^{\text{core}})^3\right)_{E_-}^{\min(\frac{1}{2}m_c, E_+)} \quad (6.11)$$

is the neutrino spectrum resulting from decay of the c -quarks injected at the solar core, with $\Gamma_{c \rightarrow \mu\nu_\mu X} = 0.13$, $E_\pm = \frac{E_i^{\text{core}}}{\gamma(1 \mp \beta)}$, $\gamma = (1 - \beta^2)^{-1/2} = E_d/m_c$, and

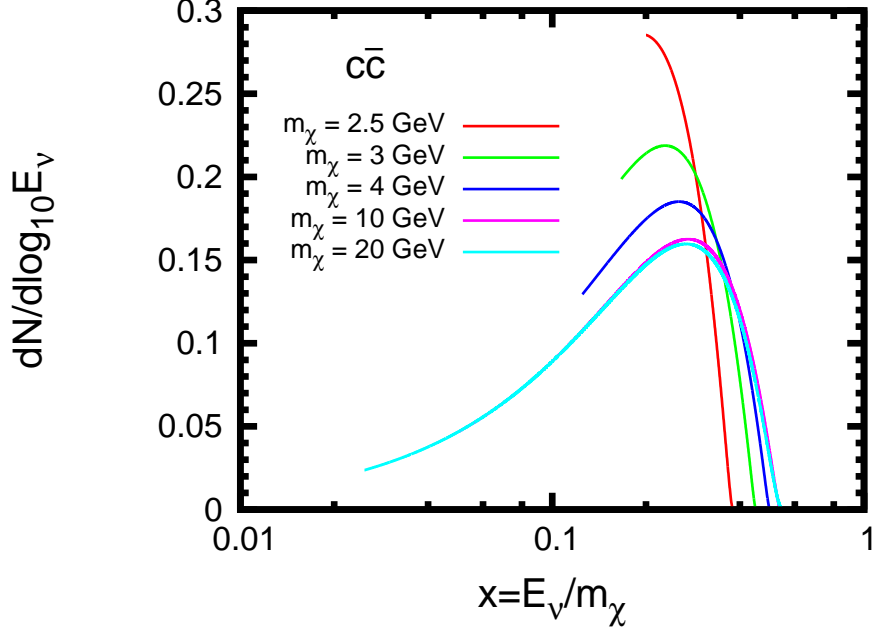


Figure 6.3: Neutrino spectra for a few representative WIMP masses for $\bar{c}c$ annihilation channel.

$\left(\frac{1}{N} \frac{dN}{dE_d}\right)^{\text{hadron}}(E_0, E_d)$ is given by equation (6.9) with $E_c \approx 250$ GeV for c -quark.

The ν_μ spectra from $\bar{c}c$ annihilation channel for several values of WIMP masses as shown in Figure 6.3.

6.2.4 $\nu\bar{\nu}$ channel : $(\chi\chi \rightarrow \nu_\mu\bar{\nu}_\mu)$

In this case the spectrum of muon neutrinos emerging from the Sun is simply given by

$$\left(\frac{dN_i}{dE_i}\right)_{\nu\bar{\nu}} = (1 - E_i\tau_i)^{(\alpha_i-2)} \left(\frac{dN_i^{\text{core}}}{dE_i^{\text{core}}}\right)_{\nu\bar{\nu}}, \quad (i = \nu_\mu, \bar{\nu}_\mu) \quad (6.12)$$

where

$$\left(\frac{dN_i^{\text{core}}}{dE_i^{\text{core}}}\right)_{\nu\bar{\nu}} = \delta(E_i^{\text{core}} - m_\chi) \equiv (1 + m_\chi\tau_i)^{-2} \delta\left(E_i - \frac{m_\chi}{1 + m_\chi\tau_i}\right). \quad (6.13)$$

The ν_μ spectra from $\nu\bar{\nu}$ annihilation channel for several values of WIMP masses as

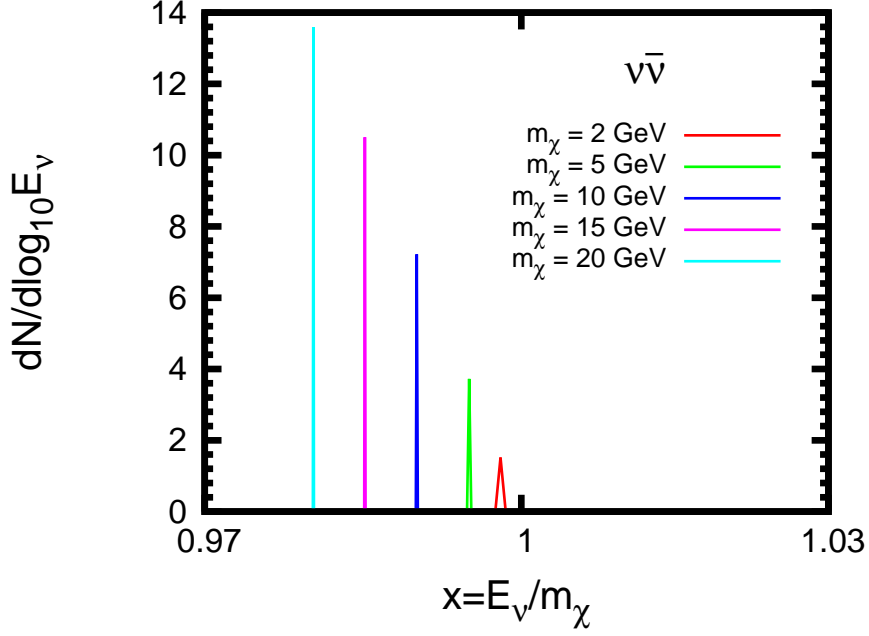


Figure 6.4: Neutrino spectra for a few representative WIMP masses for $\nu\bar{\nu}$ annihilation channel.

shown in Figure 6.4.

6.3 Calculation of Event Rates in the Super-Kamiokande Detector

The rate of neutrino induced upward-going muon events, \mathcal{R} , in the S-K detector due to ν_μ s and $\bar{\nu}_\mu$ s from WIMP annihilation in the Sun can be written as

$$\mathcal{R} = \frac{1}{2} \sum_{i=\nu_\mu, \bar{\nu}_\mu} \int \int \frac{d\phi_i}{dE_i} \frac{d\sigma_{iN}}{dy}(E_i, y) V_{\text{eff}}(E_\mu) n_p^{\text{water}} dE_i dy, \quad (6.14)$$

where $\frac{d\phi_i}{dE_i}$ is the differential flux of the neutrinos given by equation (6.1), $\frac{d\sigma_{iN}}{dy}$ are the relevant neutrino-nucleon charged current differential cross sections, $(1-y)$ ($= E_\mu/E_i$) is the fraction of the neutrino energy transferred to the muon, $V_{\text{eff}}(E_\mu)$ is the effective volume of the detector, and n_p^{water} is the number density

of protons in water (= Avogadro number). The S-K Collaboration imposed a cut on the upward-going muon path-length of > 7 meters in the inner detector which has an effective area of $A_{\text{eff}} \approx 900 \text{ m}^2$ and height ≈ 36.2 m. This 7-meter cut on the muon track length can be effectively taken into account by setting $V_{\text{eff}} = 0$ if the effective water-equivalent muon range, $R_{\mu}(E_{\mu}) \approx 5 \text{ meters} \times (E_{\mu}/\text{GeV})$, is less than 7 meters, and $V_{\text{eff}} = A_{\text{eff}} \times [R_{\mu}(E_{\mu}) + (36.2 - 7) \text{ meters}]$ otherwise [149]. The factor of $1/2$ accounts for the fact that only up-going muon events were considered in order to avoid the background due to down-going muons produced due to cosmic ray interactions in the Earth's atmosphere.

The S-K muon events were broadly classified into three categories [279], namely, (i) Fully Contained (FC), (ii) Stopping (S) and (iii) Through-Going (TG) events. For ν_{μ} energy $\lesssim 4 \text{ GeV}$ the events are predominantly of FC type, whereas for ν_{μ} energy $\gtrsim 8 \text{ GeV}$ the events are predominantly of TG type. Assuming that annihilation of the WIMP of mass m_{χ} produces neutrinos of typical energy $\sim (\frac{1}{3} - \frac{1}{2})m_{\chi}$, we can roughly divide the m_{χ} range of our interest into three regions according to the resulting muon event types namely, (i) $2 \lesssim m_{\chi} \lesssim 8 \text{ GeV}$ (FC), (ii) $8 \lesssim m_{\chi} \lesssim 15 \text{ GeV}$ (FC + S) and (iii) $15 \text{ GeV} \lesssim m_{\chi}$ (FC + S + TG).

To set upper limits on the WIMP elastic scattering cross section as a function of WIMP mass for a given annihilation channel, we use the following 90% C.L. upper limits [147, 148] on the rates of the upgoing muon events of the three different types mentioned above:

$$\begin{aligned} \mathcal{R}_{\text{FC}}^{90\% \text{C.L.}} &\simeq 13.8 \text{ yr}^{-1}, \\ \mathcal{R}_{\text{S}}^{90\% \text{C.L.}} &\simeq 1.24 \text{ yr}^{-1}, \\ \mathcal{R}_{\text{TG}}^{90\% \text{C.L.}} &\simeq 0.93 \text{ yr}^{-1}. \end{aligned} \tag{6.15}$$

The upper limits on the WIMP-nucleon elastic scattering cross section so derived

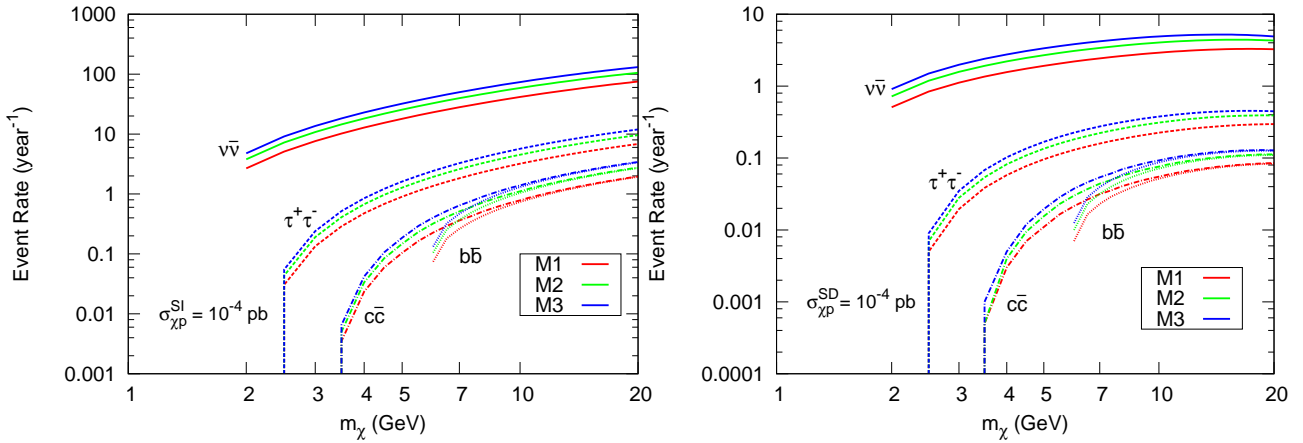


Figure 6.5: The upward going muon event rates in the Super-Kamiokande detector due to neutrinos from WIMP annihilation in the Sun as a function of the WIMP mass for the four annihilation channels as indicated, assuming 100% branching ratios for each channel by itself, and for spin-independent (SI: left panel) and spin-dependent (SD: right panel) WIMP-proton interactions. The three curves for each annihilation channel correspond, as indicated, to the three halo models specified in Table 5.1 in Chapter V. All the curves are for a reference value of the WIMP-proton elastic SI or SD cross section of 10^{-4} pb.

are then translated into upper limits on the branching fractions of various annihilation channels by demanding the consistency of the DAMA-compatible region of the WIMP parameter space obtained from an analysis of direct detection experiments discussed in Ref. [155] with S-K upper limits. These limits are discussed in the next section.

The event rates in the S-K detector as a function of the WIMP mass for the four different WIMP annihilation channels are shown in Figure 6.5 assuming 100% branching ratio for each channel by itself. For each annihilation channel the three curves correspond, as indicated, to the three halo models specified in Table 5.1 in Chapter V. It is seen that the direct annihilation to the $\nu\bar{\nu}$ channel dominates the event rate, followed by the $\tau^+\tau^-$ channel.

6.4 Exclusion Plots

Our main results are contained in Figures 6.6, 6.7 and 6.8, where we show, for the three halo models considered, the 90% C.L. upper limits on the WIMP-proton SI and SD elastic cross sections (as a function of WIMP mass) derived from the Super-Kamiokande measurements of the up-going muon events from the direction of the Sun [147, 148], for the four annihilation channels discussed in the text, assuming 100% branching ratio for each channel by itself. In these Figures, we also display, for the respective halo models, the 90% C.L. allowed regions [155] in the WIMP mass vs. WIMP-proton elastic cross section plane implied by the DAMA/LIBRA collaboration's claimed annual modulation signal [280], as well as the 90% C.L. upper limits [155] on the relevant cross section as a function of the WIMP mass implied by the null results from the CRESST-1 [281], CDMS-II-Si [282], CDMS-II-Ge [283] and XENON10 [284] experiments.

The curves in Figures 6.6, 6.7 and 6.8 allow us to derive upper limits on the branching fractions of the various WIMP annihilation channels, from the requirement of consistency of the S-K-implied upper limits on the WIMP-proton elastic cross section with the DAMA-compatible regions, the regions of the WIMP mass versus cross section parameter space within which the annual modulation signal observed by the DAMA/LIBRA experiment [280] is compatible with the null results of other DD experiments. These upper limits are shown in Table 6.1 for the three halo models discussed in the text.

Clearly, for the case of spin-independent interaction, there are no constraints on the branching fractions for the $\bar{b}b$ and $\bar{c}c$ channels since the DAMA-compatible region is already consistent with the S-K upper limit even for 100% branching fractions in these channels (the respective curves for the various annihilation channels only move upwards, keeping the shape same, as the branching fractions are made smaller). At

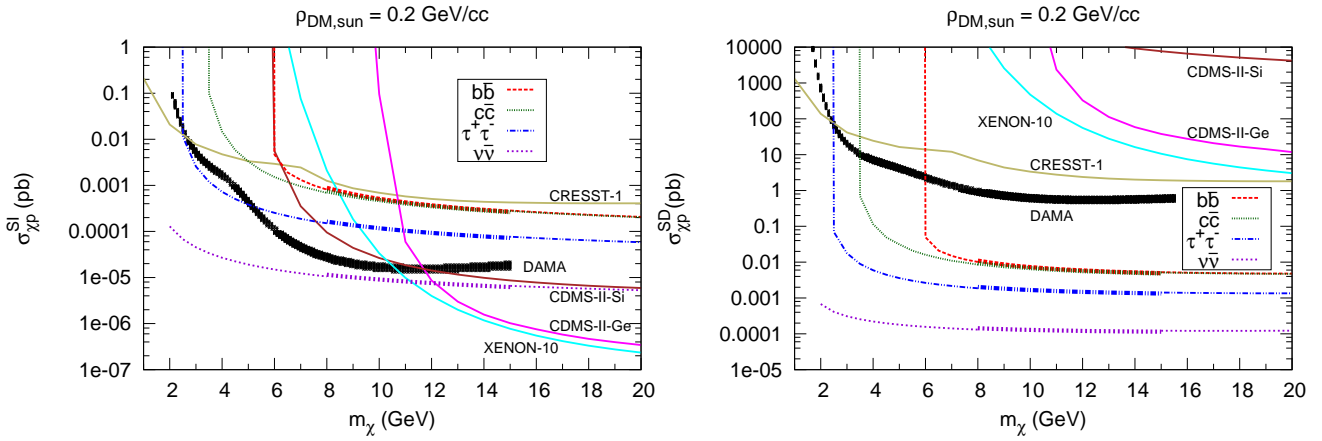


Figure 6.6: The 90% C.L. upper limits on the WIMP-proton spin-independent (SI: left panel) and spin-dependent (SD: right panel) elastic cross section as a function of WIMP mass derived from the Super-Kamiokande measurements of the up-going muon events from the direction of the Sun [147, 148], for the three relevant event types, namely, Fully Contained (FC), Stopping (S) and Through Going (TG), as discussed in the text. The thick portions of the curves serve to demarcate the approximate m_χ ranges where the different event types make dominant contributions to the upper limits. The curves shown are for the four annihilation channels, assuming 100% branching ratio for each channel by itself. The 90% C.L. allowed regions in the WIMP mass vs. WIMP-proton elastic cross section plane implied by the DAMA/LIBRA experiment's claimed annual modulation signal [280] as well as the 90% C.L. upper limits on the cross section as a function of the WIMP mass implied by the null results from the CRESST-1 [281], CDMS-II-Si [282], CDMS-II-Ge [283] and XENON10 [284] experiments (solid curves) are also shown. All the curves shown are for our halo model M1 ($\rho_{\text{DM},\odot} = 0.2 \text{ GeV}/\text{cm}^3$) specified in Table 5.1 in Chapter V.

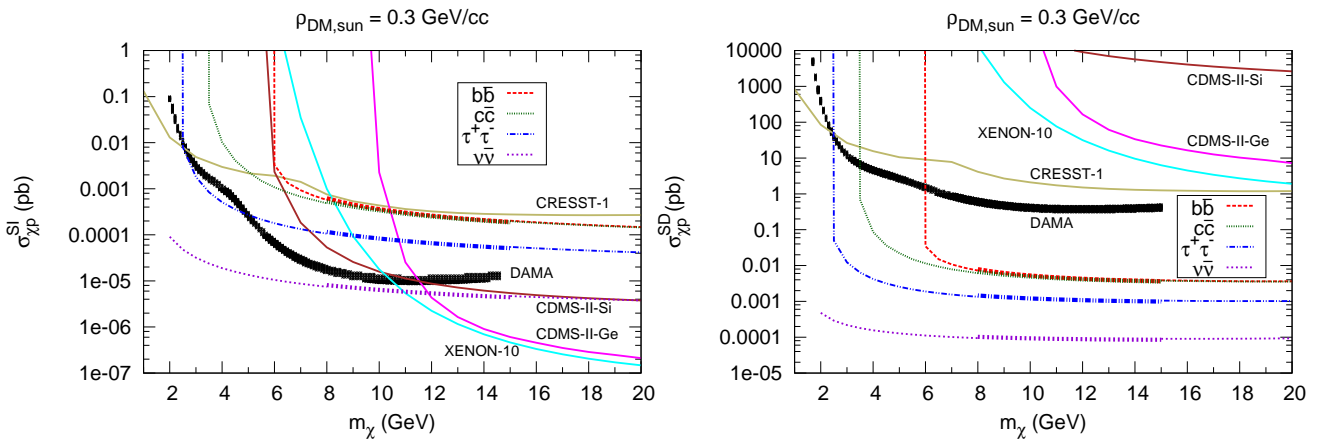


Figure 6.7: Same as Fig. 6.6, but for the halo model M2 ($\rho_{\text{DM},\odot} = 0.3 \text{ GeV}/\text{cm}^3$) specified in Table 5.1 in Chapter V.

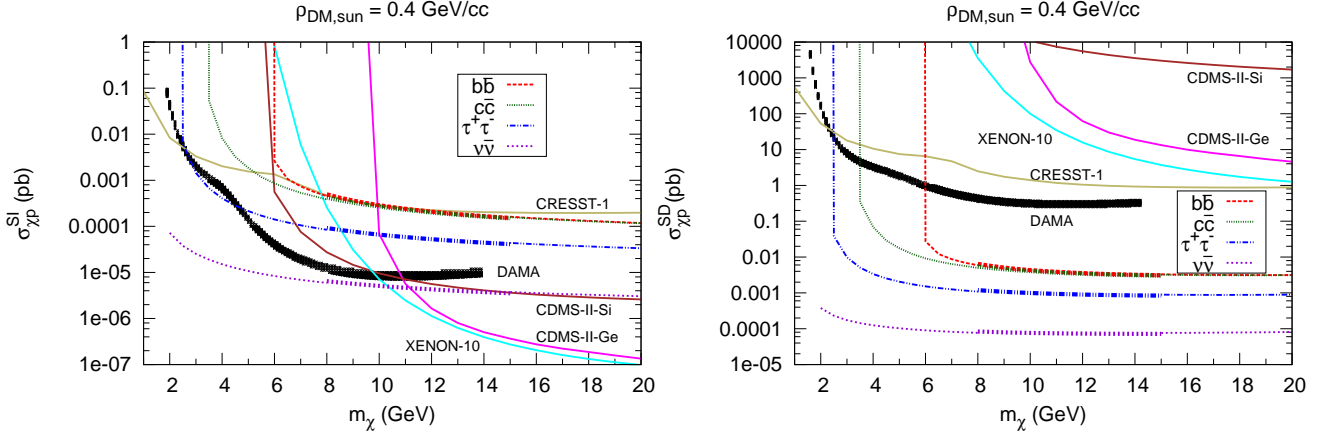


Figure 6.8: Same as Fig. 6.6, but for the halo model M3 ($\rho_{DM,\odot} = 0.4 \text{ GeV/cm}^3$) specified in Table 5.1 in Chapter V.

	EVENT TYPE (m_χ range in GeV)	UPPER LIMITS ON THE BRANCHING FRACTIONS (in %) (M1, M2, M3)			
		$b\bar{b}$	$c\bar{c}$	$\tau^+\tau^-$	$\nu\bar{\nu}$
SI	FC (2.0 – 8.0)	100, 100, 100	100, 100, 100	35, 40, 45	0.4, 0.6, 0.8
	FC+S (8.0 – 15.0)	100, 100, 100	100, 100, 100	100, 100, 100	25, 30, 35
	FC+S+TG (15.0 – 20.0)	100, 100, 100	100, 100, 100	100, 100, 100	25, 30, 35
SD	FC (2.0 – 8.0)	0.5, 0.6, 0.7	0.5, 0.6, 0.7	0.05, 0.06, 0.07	0.0005, 0.0006, 0.0007
	FC+S (8.0 – 15.0)	0.6, 0.7, 0.8	0.6, 0.7, 0.8	0.14, 0.16, 0.18	0.012, 0.014, 0.016
	FC+S+TG (15.0 – 20.0)	0.6, 0.7, 0.8	0.6, 0.7, 0.8	0.14, 0.16, 0.18	0.012, 0.014, 0.016

Table 6.1: Upper limits — derived from Figures 6.6, 6.7 and 6.8 — on the branching fractions for the four annihilation channels, from the requirement of consistency of the S-K implied upper limits on the WIMP-proton elastic cross sections with the “DAMA-compatible” region of the WIMP mass versus cross section parameter space (within which the annual modulation signal observed by the DAMA/LIBRA experiment [280] is compatible with the null results of other DD experiments determined within the context of our halo model [155]), for both spin-independent (SI) and spin-dependent (SD) interactions and the three halo models specified in Table 5.1 in Chapter V. The limits are calculated using the three different upward-going muon event types, namely, Fully Contained (FC), Stopping (S) and Through Going (TG). The three consecutive numbers for each annihilation channel and muon event type refer to the three different halo models M1, M2, M3, as indicated.

the same time, for the $\tau^+\tau^-$ channel and SI interaction, although a 100% branching fraction in this channel allows a part of the DAMA-compatible region to be consistent with the S-K upper limit, consistency of the *entire* DAMA-compatible region with the S-K upper limit requires the branching fraction for this channel to be less than 35–45% depending on the halo model. On the other hand, for the $\nu\bar{\nu}$ channel and SI interaction, there are already strong upper limits (at the level of 25 – 35%) on the branching fraction for this channel for consistency of even a part of the DAMA-compatible region with the S-K upper limit; and these upper limits become significantly more stringent (by about two orders of magnitude) if the entire DAMA-compatible region is required to be consistent with the S-K upper limits.

The constraints on the branching fractions of various annihilation channels are, however, much more severe in the case of spin-dependent interaction: For the quark channels, only parts of the DAMA-compatible region can be made consistent with the S-K upper limits, and that only if the branching fractions for these channels are restricted at the level of (0.6 – 0.8)%. On the other hand, for $\tau^+\tau^-$ and $\nu\bar{\nu}$ channels, parts of the DAMA-compatible regions can be consistent with S-K upper limits only if their branching fractions are restricted at the level of (0.14 – 0.18)% and (0.012 – 0.016)%, respectively, while consistency of the entire DAMA-compatible regions with the S-K upper limits requires these fractions to be respectively lower by about a factor of 2.5 (for the $\tau^+\tau^-$ channel) and a factor of about 25 (for the $\nu\bar{\nu}$ channel).

The above small numbers for the upper limits on the branching fractions of the four dominant neutrino producing WIMP annihilation channels imply, in the case of spin-dependent WIMP interaction, that the DAMA-allowed region of the $m_\chi - \sigma_{\chi p}^{\text{SD}}$ parameter space is essentially ruled out by the S-K upper limit on neutrinos from possible WIMP annihilations in the Sun, unless, of course, WIMPs efficiently evaporate from the Sun — which may be the case for relatively small mass WIMPs below 4 GeV [149] — or there are other non-standard but dominant WIMP annihilation

lation channels that somehow do not eventually produce any significant number of neutrinos while restricting annihilation to quark ($\bar{b}b$, $\bar{c}c$) channels to below 0.5% level and $\tau^+\tau^-$ and $\nu\bar{\nu}$ channels to below 0.05% and 0.0005% level, respectively. In the case of spin-independent interaction, however, the DAMA-compatible region of the $m_\chi - \sigma_{\chi p}^{\text{SI}}$ parameter space (or at least a part thereof) remains unaffected by the S-K upper limit if WIMPs annihilate dominantly to quarks and/or tau leptons, and annihilation directly to neutrinos is restricted below $\sim (25 - 35)\%$ level. At the same time, portions of the DAMA-compatible region can be excluded if WIMP annihilation to $\tau^+\tau^-$ occurs at larger than $(35 - 45)\%$ level and/or annihilation to $\nu\bar{\nu}$ occurs at larger than $(0.4 - 0.8)\%$ level. These results, based as they are on a self-consistent model of the Galaxy's dark matter halo, the parameters of which are determined by a fit to the rotation curve of the Galaxy, strengthen, at the qualitative level, the earlier conclusion within the SHM that the S-K upper limit on the possible flux of neutrinos due to WIMP annihilation in the Sun severely restricts the DAMA region of the WIMP mass versus cross section plane, especially in the case of spin-dependent interaction of WIMPs with nuclei, although the quantitative restrictions on the WIMP cross section and branching fractions of various WIMP annihilation channels obtained here are different (in some cases by more than a factor of 10) from those obtained in earlier calculations within the SHM [149].

6.5 Exclusion Plots from another larger dataset

A new set results of the S-K collaboration's search for upward-going muons ("up-muon") due to neutrinos from Sun is also given by Ref [285]. These new results are based on a data set consisting of 3109.6 days of data, nearly double the size of the old data set of 1679.6 days used in Ref. [147] and in the analysis of this chapter so far. In this section we consider these new results of Ref. [285] and present the resulting changes to the constraints on various WIMP annihilation channels derived

above using the earlier S-K results. In general, we find that with the new S-K results the upper limits on the branching fractions of various annihilation channels become more stringent by a factor of 3 – 4 than those derived above.

The upmu event categories used in the new S-K paper [285] are somewhat different from those in their earlier work [147]. These are: “stopping” (S), “non-showering through-going” (NSTG), and “showering through-going” (STG); see Ref. [285] for details. For a given WIMP mass, Figure 2 of Ref. [285] allows us to read out the fraction of each upmu event type contributing to the total number of events, from the consideration that the typical maximum energy of a neutrino produced in the annihilation of a WIMP of mass m_χ is $\sim m_\chi/2$. For low WIMP masses of our interest in this paper, $m_\chi \lesssim 20$ GeV (and hence typical neutrino energies $\lesssim 10$ GeV), the stopping events dominate and constitute more than 70% of the total number of upmu events, as clear from Figure 2 of Ref. [285]. It is thus expected, as indeed we do find from our calculations, that the most stringent upper limits on the branching fractions of various WIMP annihilation channels for low WIMP masses come from the observed rate of these Stopping events.¹

The 90% C.L. Poissonian upper limit on the rate of these Stopping-type upmu events for the new data set of Ref. [285], estimated from the total number of this type of upmu events and the number of background upmus due to atmospheric neutrinos given in Figure 3 of that reference, is ² ~ 3.27 yr⁻¹. With this, we can calculate, as we did in the analysis above, the 90% C.L. upper limits on the WIMP-proton SI and SD elastic cross sections as a function of WIMP mass for the new S-K data set of Ref. [285], for the case of 100% branching ratio for each of the four annihilation channels considered above. The results, for our best-fit halo model M1, are shown in Figure 6.9.

¹Recall that, for the older data set [147], the most stringent upper limits came from the fully-contained (FC) events; see Table 6.1 above.

²We take the events in the 0–30 degree cone half-angle bin around the Sun to be consistent with the analysis done above for the earlier S-K data set.

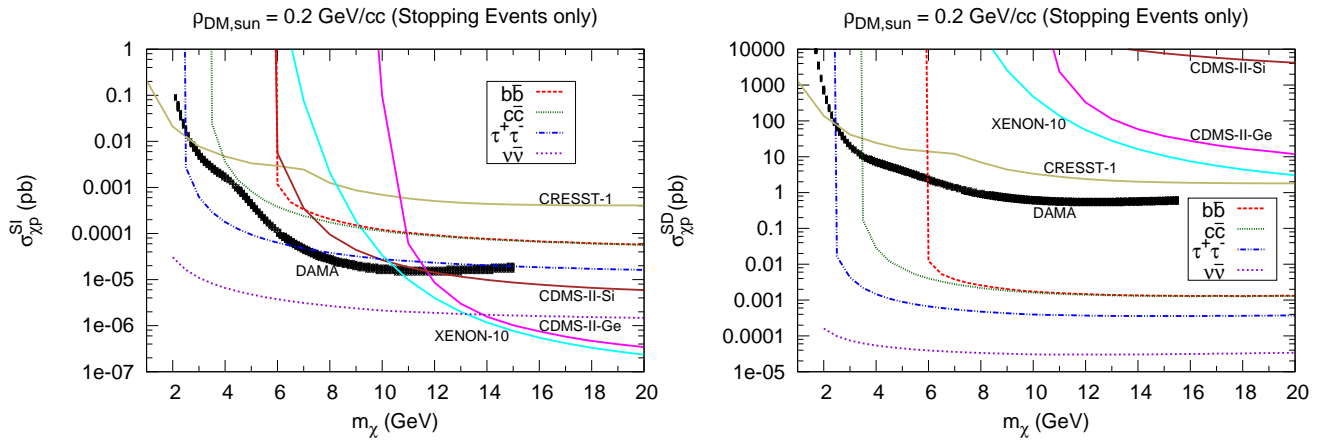


Figure 6.9: Same as Fig. 6.6, but using the new S-K data from Ref. [285] and considering their “Stopping” upmu events only.

Upper limits on the branching fractions (in %)				
from “Stopping” events, with halo model M1				
	$b\bar{b}$	$\bar{c}c$	$\tau^+\tau^-$	$\nu\bar{\nu}$
SI	100	100	10	0.11
SD	0.12	0.12	0.012	0.00013

Table 6.2: Upper limits on the branching fractions of the four annihilation channels, derived from the requirement of consistency of the new S-K-implied upper limits on the WIMP-proton elastic cross sections shown in Figure 6.9 with the “DAMA-compatible” regions, for both spin-independent (SI) and spin-dependent (SD) interactions

The resulting upper limits on the branching fractions of the four annihilation channels, derived from the requirement of consistency of the new S-K-implied upper limits on the WIMP-proton elastic cross sections shown in Figure 6.9 with the “DAMA-compatible” regions, are displayed in Table 6.2. A comparison with the corresponding numbers given in Table 6.1 shows that the new upper limits on the branching fractions for the relevant annihilation channels are roughly a factor of 3–4 more stringent.

6.6 Summary

In this section we summarize our main results. In this chapter we have calculated the expected neutrino flux from the Sun due to annihilation of WIMPs captured and accumulated inside the Sun, and derive constraints on the WIMP- nucleon elastic scattering cross section from the upper limits on the flux of such neutrinos given by the Super-Kamiokande experiment [147]. We have used the capture rate of WIMPs in the Sun calculated in the last chapter within the context of a self-consistent model of finite sized DM halo of the Galaxy, namely, the King model, including the gravitational effect of the observed visible matter on the DM. The parameters of the model are determined by performing fit to the observed rotation curve data of the Galaxy. An important aspect of the King model of the Galactic halo used in the present calculation is the non-Maxwellian nature of the WIMP velocity distribution in this model, as opposed to the Maxwellian distribution in the SHM. This directly affects the WIMP capture rate (and consequently the annihilation rate), resulting in significant quantitative differences in the values of the upper limits on the WIMP-proton elastic cross sections (implied by the S-K upper limits on the neutrinos from the Sun) compared to the values in the SHM. Similarly, the upper limits on the branching fractions of various possible WIMP annihilation channels (from the requirement of compatibility with DAMA results) are also changed. At a qualitative level, however, the general conclusion reached earlier [148, 149] within the context of the SHM, that S-K upper limits on neutrinos from the Sun severely restrict the DAMA-compatible region of the WIMP parameter space, remains true in the present model too, thus adding robustness to this conclusion.

Chapter 7

Summary, Conclusion and Outlook

Weakly interacting massive particles (WIMPs) are currently one of the most favored candidates for the dark matter (DM) in the Universe. On the scales of galaxies, the nature of the measured rotation curve, which is the the circular speed as a function of galactocentric distance, of the spiral Galaxies like our Galaxy the Milky Way can be understood most naturally under the hypothesis that the observed visible matter (VM) in these galaxies is embedded in a roughly spherical DM halo. The extent of the DM halo is perhaps a few hundred kpc in radius. The true mass and extent of the DM halo are however unknown.

Several experiments going on worldwide are currently engaged in attempts to detect these WIMPs either directly through observing the signature of scattering of these WIMPs off nuclei of suitably chosen detector material or indirectly through detecting the neutrinos, γ -rays resulting from (self-) annihilation of WIMPs captured in massive astrophysical objects such as Sun or Earth or in dense astrophysical environments such as Galactic centre or dense spherical Galaxies.

Two crucial astrophysical inputs required for the analysis and interpretation of the results of both direct as well as indirect experiments are the local (i.e. solar neigh-

borhood) density and velocity distribution of WIMPs. These are a priori unknown. In this thesis we have presented some studies with the aim of extracting information about the phase space distribution of the WIMPs that may constitute the DM halo of our Galaxy, using the observed rotation curve data of the Galaxy. We have also studied, in this thesis, the implication of phase space distribution function for indirect detection of WIMPs via neutrino signal from WIMP annihilation in Sun within the context of a self consistent model of phase space distribution function (PSDF) representing a finite sized halo. The parameters of the model are obtained by performing fit to the observed rotation curve data. The possible modification of phase space distribution function due to the gravitational influence of visible matter is also self-consistently taken in to consideration into the model.

In this thesis we have presented two different approaches to determine the phase space distribution of the DM in our Galaxy. In Chapter II we have derived the velocity distribution function (VDF) of the WIMPs directly from the circular speed (“rotation”) curve data [140] of the Galaxy assuming isotropic VDF [135]. This is done by “inverting” the Navarro-Frenk-White (NFW) [158, 136] universal density profile of the dark matter halo of the Galaxy using Eddington’s method [133, 157]. According to Eddington’s formalism, given a isotropic density profile of a set of collisionless particles, we can calculate the VDF using Eddington’s formula provided the total gravitational potential in which the particles move is known. We have determined the parameters of the model by using the Markov Chain Monte Carlo (MCMC) technique by fitting to the observational data on the Galaxy’s rotation curve extended to distances well beyond the visible edge of the disk of the Galaxy [140]. One of the parameters of the dark matter model i.e the NFW model is the local dark matter density itself which comes out to be 0.2 GeV cm^{-3} as a result of the MCMC analysis. Once the PSDF is obtained as a function of energy using the Eddington method, next we derived the most-likely local isotropic velocity distribution function (VDF). The VDF is found to be differing significantly from the

Maxwellian form assumed in the “standard halo model” (SHM) customarily used in the analysis of the results of WIMP detection experiments. We have also provided a parametrized (non-Maxwellian) form of the derived most-likely local VDF which can be readily used in direct and indirect detection analysis. We have also shown that the non-Maxwellian nature of the VDF prevails not only at the solar location but also everywhere in the Galaxy. In this chapter we have further calculated other physically relevant quantities for the Galaxy. The virial radius of the Galaxy is found to be ~ 200 kpc and the maximum velocity v_{\max} which is important for the calculation of direct and indirect detection rates is self-consistently determined to be 516 km s^{-1} .

It is evident from Chapter II that the values of the parameters of the dark matter model are determined by the rotation curve (RC) itself. These parameters in turn crucially affect the direct and indirect detection analysis of dark matter. Therefore it is necessary to construct the RC itself, extending upto large Galactocentric distances, without assuming any model of the dark matter and visible matter. However the RC is not a directly measurable quantity. In Chapter III we have constructed the rotation curve (RC) of the Galaxy from a Galactocentric distance of ~ 0.2 kpc out to ~ 200 kpc by using kinematical data on a variety non-disk objects that trace the gravitational potential of the Galaxy, without assuming any theoretical models of the visible and dark matter components of the Galaxy [143]. We have studied the dependence of the RC on the choice of the Galactic constants (GCs), $\left[\frac{R_0}{\text{kpc}}, \frac{V_0}{\text{km s}^{-1}} \right]$, where R_0 and V_0 are the sun’s distance from and circular rotation speed around the Galactic center, respectively, and also studied the dependence on the velocity anisotropy parameter β of the non-disk tracers. The RC in the disk region depends significantly on the choice of values of the GCs. The rotation curve at large distances beyond the stellar disk, however, depends more significantly on the parameter β than on the values of the GCs. We have found that in general, the mean RC steadily declines beyond $r \sim 60$ kpc, irrespective of the value of β . At any

given Galactocentric distance r , the circular speed is lower for larger values of β . The largest possible value of β is unity (complete radial anisotropy) and this allows us to set a model independent lower limit on the total mass of the Galaxy, giving $M(\lesssim 200 \text{ kpc}) \geq (6.8 \pm 4.1) \times 10^{11} M_{\odot}$. We have also noted that recent results from high resolution hydrodynamical simulations [182] of formation of galaxies like Milky Way indicate an increasingly radially biased velocity ellipsoid of the Galaxy's stellar population at large distances, with stellar orbits tending to be almost purely radial ($\beta \rightarrow 1$) beyond $\sim 100 \text{ kpc}$. This implies that the above lower limit on the Galaxy's mass (obtained from our results with $\beta = 1$) may in fact be a good estimate of the actual mass of the Galaxy out to $\sim 200 \text{ kpc}$.

In Chapter IV we have presented another approach to derive the phase space distribution function of dark matter particles by starting from an ansatz which is different from the formalism presented in Chapter II. We have assumed that being collisionless system of particles the DM obeys the collisionless Boltzmann equation (CBE) and hence their PSDF can be expressed as a solution of the CBE. We have adopted in this chapter the ‘‘Michie model’’ [133, 144] which is a function of both total energy and total angular momentum of the system thus allowing possible velocity anisotropy of the system as also suggested by recent numerical simulations of galaxies and clusters. We have self-consistently included the gravitational effect of visible matter on the DM model. We have considered two sets of rotation curve data standardized at two GC sets, namely [8.3, 244] and [8.5, 220] and the non-disk tracers' velocity anisotropy is taken from a recent hydrodynamic simulation [182] as presented in Chapter III to determine the best-fit values of the model parameters. We have performed fit to the above mentioned rotation curve data and the local dark matter density $\rho_{\text{DM},\odot}$ which is one of the parameters of the model is observed to depend on the local circular velocity V_0 , used in deriving the RC obtained in chapter III. Usually higher value of V_0 yields higher value of $\rho_{\text{DM},\odot}$. For example, as the local circular velocity V_0 is scaled from 220 km s^{-1} to 244 km s^{-1} the local

dark matter density $\rho_{\text{DM},\odot}$ scales from 0.4 GeV cm^{-3} to 0.6 GeV cm^{-3} . This result is independent of the choice of the local VM disk surface density. We have also shown that as an effect of the coupling with the visible matter the core radius of the dark matter halo gets shortened and the core density is increased because the VM pulls in more dark matter towards the centre. The dark matter density near the disk region is also enhanced by a factor of $\sim 20\%$. The gravitational effect of the VM is also evident from the velocity dispersion profiles, namely the radial, tangential and total velocity dispersion. These are also found to be higher in the coupled case as compared to the uncoupled case. The radial, tangential and total velocity distributions at solar location as well as at other Galactic radii is found to be non-Maxwellian. The value of the anisotropy parameter is observed to rise from a 0 value at centre to value 1 which is consistent with observations from numerical simulations. The local value of the velocity anisotropy parameter is found to be ~ 0.45 .

Next in Chapter V and Chapter VI we have presented the methods and results of our study of the indirect detection of dark matter via neutrino signal from dark matter annihilation in Sun [146]. Scattering of WIMPs off nuclei can lead to capture of the WIMPs by massive astrophysical bodies such as the Sun if, after scattering off a nucleus inside the body, the velocity of the WIMP falls below the escape velocity of the body. The WIMPs so captured over the lifetime of the capturing body would gradually settle down to the core of the body where they would annihilate and produce standard model particles, e.g., W^+W^- , Z^0Z^0 , $\tau^+\tau^-$, $t\bar{t}$, $b\bar{b}$, $c\bar{c}$, etc. Decays of these particles would then produce neutrinos, gamma rays, electrons-positrons, protons-antiprotons, etc. In Chapter V we have derived the capture rate within the context of a self-consistent model of the phase space distribution function of the DM halo of the Galaxy, namely the King model, which is the isotropic version of the Michie model discussed in Chapter IV. We have made the standard assumption that the capture and annihilation processes have reached an equilibrium over the long lifetime of the solar system (~ 4.2 billion yrs). Under this assumption, the

total annihilation rate of WIMPs in the Sun is simply half of the total capture rate. Therefore, the WIMP annihilation cross section disappears from the model and the only cross section we are concerned with is the WIMP nucleon elastic scattering cross section. This allows us to present our results in terms of exclusion plots in the WIMP parameter space, namely the WIMP mass and WIMP-nucleon elastic scattering cross section space, and hence compare with the findings of direct detection experimental on the the WIMP nucleon scattering cross section. We have considered in Chapter VI, low mass WIMPs ($2 \text{ GeV} \leq m_\chi \leq 20 \text{ GeV}$) therefore we are left with four annihilation channels namely $\tau^+\tau^-$, $b\bar{b}$, $c\bar{c}$, and prompt $\nu\bar{\nu}$. We have calculated the upward going muon event rates in the Super-Kamiokande (S-K) detector [85] due to neutrinos from WIMP annihilation in the Sun as a function of the WIMP mass for the four annihilation channels, assuming 100% branching ratios for each channel by itself, for spin-independent (SI) and spin-dependent (SD) WIMP-proton interactions. We have considered three best-fit King models of the DM halo with a reference value of the WIMP-proton elastic SI or SD cross section of 10^{-4} pb. We have calculated the 90% C.L. upper limits on the WIMP-proton SI and SD elastic cross sections as a function of the WIMP mass for four WIMP annihilation channels using the Super-Kamiokande upper limits [146], and examined the consistency of those limits with the 90% C.L. “DAMA-compatible” regions (the regions of the WIMP mass versus cross section parameter space within which the annual modulation signal observed by the DAMA/LIBRA experiment is compatible with the null results of other DD experiments).

We have found that the requirement of consistency of the Super Kamiokande implied upper limits on the WIMP-proton elastic cross section as a function of WIMP mass with that of the direct detection experiments [155] imposes stringent restrictions on the branching fractions of the various WIMP annihilation channels. In the case of spin-independent (SI) WIMP-proton interaction, the S-K upper limits do not place additional restrictions on the DAMA-compatible region of the WIMP parameter

space if the WIMPs annihilate dominantly to $\bar{b}b$ and $\bar{c}c$, and if direct annihilations to $\tau^+\tau^-$ and neutrinos are restricted to below $\sim (35 - 45)\%$ and $(0.4 - 0.8)\%$, respectively. In the case of spin-dependent (SD) interactions, on the other hand, the restrictions on the branching fractions of various annihilation channels are much more stringent, essentially ruling out the DAMA-compatible region of the WIMP parameter space if the relatively low-mass WIMPs under consideration annihilate predominantly to any mixture of $\bar{b}b$, $\bar{c}c$, $\tau^+\tau^-$, and $\nu\bar{\nu}$ final states. The very latest results from the S-K Collaboration with larger data set put the above conclusions on an even firmer footing by making the above constraints on the branching fractions of various WIMP annihilation channels more stringent by roughly a factor of 3–4 [146]. Similar conclusions were reached by earlier studies [149] in literature within the context of the SHM. The quantitative restrictions on the branching fractions for various WIMP annihilation channels obtained here with King model are, however, more stringent compared to those obtained in the earlier works within the context of standard halo model (SHM).

The search for Dark matter and the quest of probing its dynamics is a very intriguing area of modern science. We would like to mention that there are many scopes of works which we wish to study in near future. In this thesis we have mainly dealt with one aspect of indirect detection, namely the neutrino signal from Dark Matter annihilation in the Sun. The γ -ray search looking for DM annihilation or decay signals from various locations in the Galaxy such as Galactic centre substructure and also in the dark matter rich dwarf spheroidals etc. with the new era γ -ray telescopes such as Fermi-LAT is also a very promising scenario. In future we would like to study the implications of the phase space distribution functions that we have discussed in this thesis in case of γ -ray search and also the antimatter searches. We have studied the upper limits imposed by the observation of the Super Kamiokande neutrino detector here. Next as an extension of this work we would like to investigate the upper limits from IceCube detector with the phase space distribution

functions discussed here namely the Michie model PSDF and the PSDF obtained by reverting the NFW density model using the Eddington's formalism. In this work we have considered low mass WIMPs only. However, it will be interesting to consider WIMPs with higher mass as for those few more WIMP annihilation channels like W^+W^- , Z^0Z^0 , $t\bar{t}$ etc. will open up.

Now concentrating on the dark matter dynamics part we have seen that the rotation curve of the Galaxy plays a crucial role in determining the parameters of the dark matter and visible matter models chosen. Therefor the immediate future step in this direction would be the betterment of the RC data itself. Upcoming Galactic surveys like GAIA [286] will provide us with three dimensional data on the velocity of the tracers and we plan to construct the rotation curve data considering those proper motion data. Focusing on the phase space distribution of the DM, so far we have worked with spherically symmetric dark matter distributions only. It will be challenging yet interesting to work with different types of visible matter distributions and dark matter halos such as a bar structured visible matter distribution, triaxial halo, rotating halo etc. In conclusion it can be said that there are still a lot of unexplored features that need to be studied in this fast evolving area of Dark Matter dynamics and experimental search. We expect to gather a lot of data to infer about the dark matter dynamics, i.e, their density and velocity distributions, from upcoming Galactic surveys and hope to probe the particle nature of the dark matter from accelerator experiments and improved versions of various direct and indirect detection experiments of dark matter.

Bibliography

- [1] P.A.R. Ade, et al. (Planck Collaboration), (2013); arXiv:1303.5076, arXiv:1303.5062.
- [2] G. Jungman, M. Kamionkowski and K. Griest, Phys. Rept. 267 (1996) 195; arXiv:hep-ph/9506380.
- [3] L. Bergstrom, Rept. Prog. Phys. 63 (2000) 793; arXiv:hep-ph/0002126.
- [4] G. Bertone, D. Hooper and J. Silk, Phys. Rept. 405 (2005) 279; arXiv:hep-ph/0404175.
- [5] J. Feng, Ann. Rev. Astron. Astrophys. 48 (2010) 495; arXiv:1003.0904.
- [6] G. Bertone (Ed.), Particle Dark Matter: Observations, Models and Searches (Cambridge Univ. Press, U. K., 2010).
- [7] J. H. Oort, Bull. Astron. Inst. Netherlands, 6 (1932) 249.
- [8] F. Zwicky, Helv. Phys. Acta. 6 (1933) 124.
- [9] F. Zwicky, Astrophysical Journal, 86 (1937) 217.
- [10] H. Babcock, Lick Observatory bulletin, no. 498 (1939).
- [11] V. C. Rubin and W. K. Ford. Jr., The Astrophysical Journal 159 (1970) 379.
- [12] V. C. Rubin, W. K. Ford. Jr., N. Thonnard, Astrophysical Journal, 238 (1980) 471.

- [13] A. Einstein, *Science* 84 (1936) 506.
- [14] F. Zwicky, *Phys. Rev.* 51 (1937) 290.
- [15] R. D. Blandford and R. Narayan, *Ann. Rev. Astron. Astrophys.* 30 (1992) 311.
- [16] A.N. Taylor, S. Dye, T.J. Broadhurst, N. Benitez and E. van Kampen, *The Astrophysical Journal*, 501 (1998) 539.
- [17] M. Milgrom, *Astrophysical Journal* 270 (1983) 365; *Astrophysical Journal* 270 (1983) 371.
- [18] [EROS Collaboration]P. Tisserand, et al, *Astronomy and Astrophysics* 469 (2007) 387; arXiv:astro-ph/0607207.
- [19] D. S. Graff and K. Freese, *The Astrophysical Journal* 456L (1996) 49G; arXiv:astro-ph/9507097.
- [20] J. R. Najita, G. P. Tiede, J. S. Carr, *The Astrophysical Journal* 541 (2000) 977.
- [21] [OGLE Collaboration]L. Wyrzykowski, et al. , *MNRAS*, 416, (2011) 2949.
- [22] K. Freese, B. Fields and D. Graff, (2000); arXiv:astro-ph/0007444.
- [23] K. Freese, B. Fields and D. Graff, *ESO ASTROPHYSICS SYMPOSIA*. p. 18; arXiv:astro-ph/0002058.
- [24] K. Abazajian, et al., *Phys. Rev. D* 71 (2005) 043507.
- [25] R. de Putter, et al., *ApJ*, 761 (2012) 12; arXiv:1201.1909.
- [26] S. Dodelson and L. M. Widrow, *Phys. Rev. Lett.* 72 (1994) 17, arXiv:hep-ph/9303287.
- [27] A. Kusenko, *Phys. Rept.* 481 (2009) 1; arXiv:0906.2968.
- [28] K. Abazajian, M. Acero, S. Agarwalla, A. Aguilar-Arevalo, C. Albright, et al., arXiv:1204.5379.

- [29] T. Moroi and H. Murayama, *Phys. Lett. B*, 303 (1993) 289.
- [30] R. D. Peccei and H. R. Quinn, *Phys. Rev. Lett.* 38 (1977) 1440.
- [31] R. D. Peccei and H. R. Quinn, *Phys. Rev. D* 16 (1977) 1791.
- [32] S. Weinberg, *Phys. Rev. Lett.* 40 (1978) 223.
- [33] A. Ringwald, *Phys. Dark. Univ.* 1 (2012) 116.
- [34] Y. B. Zeldovich, *Adv. Astron. Astrophys.* 3 (1965) 241.
- [35] H. Y. Chiu, *Phys. Rev. Lett.* 17 (1966) 712.
- [36] G. Steigman, *Ann. Rev. Nucl. Part. Sci.* 29 (1979) 313.
- [37] R. J. Scherrer and M. S. Turner, *Phys. Rev. D* 33 (1986) 1585.
- [38] Y. B. Zel'dovich, *Zh. Eksp. Teor. Fiz.* 48 (1965) 986.
- [39] Y. B. Zel'dovich, L. B. Okun and S. B. Pikelner, *Usp. Fiz. Nauk.* 84 (1965) 113.
- [40] B. W. Lee and S. Weinberg, *Phys. Rev. Lett.* 39 (1977) 165.
- [41] E. Kolb and M. Turner , *The Early Universe*, (Westview Press. 1994)
- [42] [DAMA Collaboration] R. Bernabei, et al., *Eur. Phys. J. C*67 (2010) 39;
arXiv:1002.1028.
- [43] [CoGeNT Collaboration] C. E. Aalseth, et al., *Phys. Rev. Lett.* 107 (2011)
141301; arXiv:1106.0650.
- [44] [CRESST Collaboration] G. Angloher, et al., *Eur. Phys. J. C*72 (2012) 1971;
arXiv:1109.0702.
- [45] [CDMS-II Collaboration]R. Agnese, et al., arXiv:1304.4279.
- [46] [CDMS-II Collaboration]Z. Ahmed, et al., *Science* 327 (2010) 1619;
arXiv:0912.3592.

- [47] [CDMS-II Collaboration]Z. Ahmed, et al., Phys. Rev. Lett. 106 (2011) 131302; arXiv:1011.2482.
- [48] [XENON100 Collaboration]E. Aprile, et al., Phys. Rev. Lett. 109 (2012) 181301 ; arXiv:1207.5988.
- [49] [XENON10 Collaboration]J. Angle, et al., Phys. Rev. Lett. 107 (2011) 151301; arXiv:1104.3088.
- [50] G. J. Alner, et al., Astropart. Phys., 23 (2005) 444; G. J. Alner, et al., Astropart. Phys., 28 (2007) 287; arXiv:astro-ph/0701858.; V. N. Lebedenko, et al., (2008); arXiv:0812.1150.
- [51] Akimov, et al., Phys. Lett. B 709 (2007) 14; arXiv:1110.4769.
- [52] [KIMS Collaboration]S. C. Kim, et al., Phys. Rev. Lett. 108 (2012) 181301; arXiv:1204.2646.
- [53] [LUX Collaboration]D. S. Akerib, et al., arXiv:1310.8214.
- [54] [The LUX collaboration] D. S. Akerib, et al., arXiv:1310.8214.
- [55] [DAMA/Libra Collaboration] R. Bernabei, et al., Eur. Phys. J. C 56 (2008) 333.
- [56] A. K. Drukier, K. Freese, and D. N. Spergel, Phys. Rev. D 33 (1986) 3495.
- [57] K. Freese, J. A. Frieman and A. Gould, Phys. Rev. D 37 (1988) 3388.
- [58] C. Savage, et al., JCAP 0904 (2009) 010.
- [59] [CoGeNT Collaboration]C.E. Aalseth, et al., Phys. Rev. Lett. 106 (2012) 131301.
- [60] [CoGeNT Collaboration]C.E. Aalseth, et al., Phys. Rev. D. 88 (2013) 012002.

- [61] [CoGeNT Collaboration]C.E. Aalseth, et al., Phys. Rev. Lett. 107 (2011) 141301.
- [62] [CDMS-II Collaboration]Z. Ahmed, et al., arXiv:1203.1309.
- [63] [CRESST-II Collaboration]G. Angloher, et al., Eur. Phys. J. C 72 (2012) 1971.
- [64] [CDMS-II Collaboration]R. Agnese, et al., arXiv:1304.4279.
- [65] [SuperCDMS Collaboration]R. Agnese, et al., arXiv:1309.3259.
- [66] [XENON100 Collaboration]E. Aprile, et al., Phys. Rev. D 83 (2011) 082001.
- [67] [XENON100 Collaboration]E. Aprile, et al., Phys. Rev. Lett. 111 (2013) 021301
- [68] [XENON10 Collaboration]J. Angle, et al., Phys. Rev. Lett. 107 (2011) 051301.
erratum: Phys. Rev. Lett. 110 (2013) 249901(E).
- [69] [XENON100 Collaboration]E. Aprile et al. Phys. Rev. D 88 (2013) 012006.
- [70] [EDELWEISS Collaboration]E. Armengaud, et al., Phys. Lett. B 702 (2011) 329.
- [71] [EDELWEISS Collaboration]E. Armengaud, et al., Phys. Rev. D 86, (2012) 051701.
- [72] [XMASS Collaboration]K. Abe, et al., Phys. Lett. B 791 (2013) 78.
- [73] [TEXONO Collaboration]H. B. Li, et al., Phys. Rev. Lett. 110 (2013) 261301.
- [74] [CDEX Collaboration]W. Zhao, et al., Phys. Rev. D 88 (2013) 052004.
- [75] [DAMIC Collaboration]J. Barreto, et al., Phys. Lett. B 711 (2012) 264.
- [76] [PICASSO Collaboration]S. Archambault, et al., Phys. Lett. B 711 (2012) 153.
- [77] [SIMPLE Collaboration]M. Felizardo, et al., Phys. Rev. Lett. 108 (2012) 201302.

- [78] [COUPP Collaboration] E. Behnke, et al., Phys. Rev. D 86 (2012) 052001.
- [79] DarkSide : <http://darkside.lngs.infn.it/>
- [80] DEAP : <http://deap.phy.queensu.ca/>
- [81] CLEAN : <https://deapclean.org/>
- [82] PandaX : <http://pandax.physics.sjtu.edu.cn/>;
- [83] [XENON1T Collaboration] L. Baudis, et al., arXiv:1309.7024.
- [84] “Indirect Detection Experiments”. <http://www.snowmass2013.org/tiki-index.php?page=WIMP+Dark+Matter+Indirect+Detection.>]
- [85] [Super-Kamiokande Collaboration] S. Fukuda, et al., Nucl. Instruments & Methods, A 501 (2003) 418; S. Desai, et al., Phys. Rev. D 70 (2004) 083523; T. Tanaka, et al., Astrophys. J. 742 (2011) 78.
- [86] [IceCube Collaboration] M. G. Aartsen, et al., arXiv:1309.7007.
- [87] F. Halzen, D. Hooper, New J. Phys. 11 (2009) 105019; arXiv:0910.4513.
- [88] [ANTARES Collaboration] J. D. Zornoza, arXiv:1204.5066.
- [89] [H.E.S.S. Collaboration] F. Aharonian, et al., Phys. Rev. Lett. 97 (2006) 221102, Erratum-ibid. 97 (2006) 249901; astro-ph/0610509.
- [90] [MAGIC Collaboration] J. Aleksic, et al., JCAP 1106 (2011) 035; arXiv:1103.0477.
- [91] [VERITAS Collaboration] V. A. Acciari, et al., Astrophys. J. 720 (2010) 1174; arXiv:1006.5955.
- [92] Cherenkov Telescope Array Consortium, arXiv:1008.3703.
- [93] L. Bergstrom, Astroparticle Physics, 43, (2013) 44.

- [94] [Fermi-LAT Collaboration] M. Ackermann, et al., Phys. Rev. Lett. 107 (2011) 241302; arXiv:1108.3546.
- [95] A. Geringer-Sameth and S. M. Koushiappas, Phys. Rev. Lett. 107 (2011) 241303; arXiv:1108.2914.
- [96] S. D. Hunter, et al., Astrophys. J. 481 (1997) 205.
- [97] W. de Boer, C. Sander, V. Zhukov, A. V. Gladyshev, D. I. Kazakov, Astron. Astrophys. 444 (2005) 51; arXiv:astro-ph/0508617.
- [98] [Fermi-LAT Collaboration] A. A. Abdo, et al., Phys. Rev. Lett. 104 (2010) 101101; arXiv:1002.3603.
- [99] J. Knodlseder, et al., Astron. Astrophys. 441 (2005) 513; arXiv:astro-ph/0506026.
- [100] G. Weidenspointner, et al., Nature 451 (2008) 159.
- [101] [H.E.S.S. Collaboration] F. Aharonian, et al., Phys. Rev. Lett. 97 (2006) 221102, Erratum-ibid. 97 (2006) 249901; arXiv:astro-ph/0610509.
- [102] [PAMELA Collaboration] O. Adriani, et al., Nature 458 (2009) 607; arXiv:0810.4995.
- [103] J. Chang, et al., Nature, 456 (2008) 362.
- [104] A. Strumia, Proc. of Science, EPS-HEP2009, (2009) 012.
- [105] L. Bergstrom, New J. Phys. 11 (2009) 105006.; arXiv:0903.4849.
- [106] [Fermi-LAT Collaboration] A. A. Abdo et al., Phys. Rev. Lett. 102 (2009) 181101; arXiv:0905.0025.
- [107] [Fermi-LAT Collaboration] A. A. Abdo et al., JCAP 1004 (2010) 014; arXiv:1002.4415.

- [108] P. Meade, M. Papucci, A. Strumia and T. Volansky, Nucl. Phys. B 831 (2010) 178; arXiv:0905.0480.
- [109] L. Bergstrom, J. Edsjo and G. Zaharijas, Phys. Rev. Lett. 103 (2009) 031103; arXiv:0905.0333.
- [110] F. A. Aharonian, A. M. Atoyan and H. J. Volk, Astron. Astrophys. 294 (1995) L41.
- [111] [FERMI-LAT Collaboration]D. Grasso, et al., Astropart. Phys. 32 (2009) 140; arXiv:0905.0636.
- [112] [AMS-02 Collaboration]M. Aguilar, et al., Phys. Rev. Lett. 110 (2013) 141102.
- [113] D. Hooper and L. Goodenough, Phys. Lett. B 697 (2011) 412; arXiv:1010.2752.
- [114] D. Hooper and T. Linden, Phys. Rev. D 84 (2011) 123005; arXiv:1110.0006.
- [115] D. Hooper, arXiv:1201.1303.
- [116] M. Chernyakova, D. Malyshev, F. A. Aharonian, R. M. Crocker and D. I. Jones, Astrophys. J. 726 (2011) 60; arXiv:1009.2630.
- [117] A. Boyarsky, D. Malyshev and O. Ruchayskiy, Phys. Lett. B 705 (2011) 165; arXiv:1012.5839.
- [118] J. Han, C.S. Frenk, V.R. Eke, L. Gao and S.D.M. White, arXiv:1201.1003.
- [119] D. Hooper, D. P. Finkbeiner and G. Dobler, Phys. Rev. D 76 (2007) 083012; arXiv:0705.3655.
- [120] M. Su, T. R. Slatyer and D. P. Finkbeiner, Astrophys. J. 724 (2010) 1044; arXiv:1005.5480.
- [121] P. Mertsch and S. Sarkar, Phys. Rev. Lett. 107 (2011) 091101; arXiv:1104.3585.
- [122] G. Dobler, Astrophys. J. 750 (2012) 17; arXiv:1109.4418.

- [123] T. Bringmann, X. Huang, A. Ibarra, S. Vogl and C. Weniger, arXiv:1203.1312; C. Weniger, arXiv:1204.2797.
- [124] Fermi-LAT data server, <http://fermi.gsfc.nasa.gov/ssc/data/access/lat/>.
- [125] [LAT Collaboration] W. B. Atwood, et al., *Astrophys. J.* 697 (2009) 1071; arXiv:0902.1089.
- [126] A. M. Galper, et al., arXiv:1201.2490.
- [127] V.A. Mitsou, arXiv:1310.1072.
- [128] [ATLAS Collaboration] G. Aad, et al., *JINST* 3 (2008) S08003.
- [129] [CMS Collaboration] R. Adolphi, et al., *JINST* 3 (2008) S08004.
- [130] [ATLAS Collaboration] G. Aad, et al., *Phys. Lett. B* 716 (2012) 1.
- [131] [CMS Collaboration] S. Chatrchyan, et al., *Phys. Lett. B* 716 (2012) 30.
- [132] G. Raffelt, *Phys. Rept.* 333 (2000) 593.
- [133] J. Binney and S. Tremaine, *Galactic Dynamics* (Princeton University Press, Princeton, New Jersey, 2008), 2nd ed.
- [134] A. M. Green, *Modern Physics Letters A*, 27 (2012) 1230004.
- [135] P. Bhattacharjee, S. Chaudhury, S. Kundu and S. Majumdar, *Phys. Rev. D*, 87 (2013) 083525.
- [136] J. F. Navarro, C. S. Frenk and S. D. M. White, *ApJ*, 490 (1997) 493.
- [137] V. Trimble, *ARA&A*, 25 (1987) 425.
- [138] Y. Sofue and V. Rubin, *ARA&A*, 39 (2001) 137.
- [139] M. Weber and W. de Boer, *A&A*, 509 (2010) A25.

- [140] Y. Sofue, PASJ, 64 (2012) 75.
- [141] F. Nesti and P. Salucci, JCAP, 1307 (2013) 016.
- [142] J. I. Read, J. Phys. G: Nucl. Part. Phys., 41 (2014) 063101; arXiv:1404.1938.
- [143] P. Bhattacharjee, S. Chaudhury and S. Kundu, ApJ, 785 (2014) 63.
- [144] S. Kundu and P. Bhattacharjee, Draft under preparation.
- [145] D. Hooper and S. Profumo, Phys. Rep., 453 (2007) 29.
- [146] S. Kundu and P. Bhattacharjee, Phys. Rev. D, 85 (2012) 123533.
- [147] [Super-Kamiokande collaboration] S. Desai et al, Phys. Rev. D. , 70 (2004) 083523 .
- [148] R. Kappl and M.W. Winkler, Nucl. Phys. B., 850 (2011) 505; arXiv:1104.0679.
- [149] D. Hooper, F. Petriello, K.M. Zurek, and M. Kamionkowski, Phys. Rev. D., 79 (2009) 015010; arXiv:0808.2464.
- [150] J.H. Oort, Bull. Astr. Inst. Netherlands, 6 (1932) 249; *ibid.* 15 (1960) 45; J.N. Bahcall, ApJ, 276 (1984) 169; P. Salucci, F. Nesti, G. Gentile and C.F. Martins, A&A, 523 (2010) A83; R. Catena and P. Ullio, JCAP, 08 (2010) 004; J. Bovy and S. Tremaine, ApJ, 756 (2012) 89.
- [151] J. H. Oort, Bull. Astron. Inst. Neth. 6 (1932) 249 ; 15 (1960) 45.
- [152] N. Bahcall, Astrophys. J. 276 (1984) 169 .
- [153] P. Salucci, F. Nesti, G. Gentile and C. F. Martins, Astron. Astrophys., 523 (2010) A83.
- [154] F.S. Ling, E. Nezri, E. Athanassoula, and R. Teyssier, J. Cosmol. Astropart. Phys. 02 (2010), 012; arXiv:0909.2028.

- [155] S. Chaudhury, P. Bhattacharjee, and R. Cowsik, *J. Cosmol. Astropart. Phys.* 09 (2010), 020; arXiv:1006.5588.
- [156] Doctoral Thesis by Soumini Chaudhury.
- [157] A. S. Eddington, *MNRAS*, 76 (1916) 572.
- [158] J.F. Navarro, C.S. Frenk and S.D.M. White, *ApJ*, 462 (1996) 563.
- [159] J. Caldwell and J. Ostriker, *ApJ*, 251 (1981) 61; K. Kuijken and G. Gilmore, *MNRAS*, 239 (1989) 571.
- [160] A. Putze, et al., *A&A*, 497 (2009) 991; A. Heavens, arXiv:0906.0664; <http://cosmologist.info/cosmomc/>.
- [161] Y. Sofue, *PASJ*, 64 (2012) 75; arXiv:1110.4431.
- [162] M. Weber and W. de Boer, *A&A*, 509 (2010) A25.
- [163] F. Hammer, et al., *ApJ*, 662 (2007) 322.
- [164] H.T. Freudenreich, *ApJ*, 492 (1998) 495.
- [165] R. Catena and P. Ullio, *JCAP*, 1205 (2012) 005. *ibid.* 239 (1989) 605; *ibid.* 239 (1989) 651; *ApJ*, L9 (1991) 367.
- [166] P.J. McMillan, *MNRAS*, 414 (2011) 2446; M.I. Wilkinson and N.W. Evans, *MNRAS*, 310 (1999) 645; W. Dehnen and J. Binney, *MNRAS*, 294 (1998) 429.
- [167] P. Ullio and M. Kamionkowski, *JHEP*, 03 (2001) 049.
- [168] J. Stadel et al., *MNRAS*, 398 (2009) L21 (GHALO); J. Diemand et al., *Nature* **454** (2008) 735 (Via Lactea); V. Springel et al., *MNRAS*, 391 (2008) 1685 (Aquarius); F.S. Ling et al., *JCAP*, 1002 (2010) 012.
- [169] J.E. Taylor and J.F. Navarro, *ApJ*, 563 (2001) 483.

- [170] R. Cowsik, C. Ratnam, P. Bhattacharjee and S. Majumdar, *NewA*, 12 (2007) 507.
- [171] B. Burch, and R. Cowsik, *ApJ*, 779 (2013) 35.
- [172] J. Binney and M. Merrifield, 1998, *Galactic Astronomy* (Princeton, NJ: Princeton Univ. Press).
- [173] Y. Sofue, M. Honma and T. Omodaka, *PASJ*, 61 (2009) 227.
- [174] J. K. Adelman-McCarthy, et al., *ApJS*, 175 (2008) 297.
- [175] X. X. Xue, et al., *ApJ*, 684 (2008) 1143.
- [176] O. Y. Gnedin, W. R. Brown, M. J. Geller and S. J. Kenyon, *ApJ*, 720 (2010) L108.
- [177] A. J. Deason, V. Belokurov, N. W. Evans and J. An, *MNRAS*, 424 (2012) L44 [D12a].
- [178] P. R. Kafle, S. Sharma, G. F. Lewis and J. Bland-Hawthorn, *ApJ*, 761 (2012) 98.
- [179] G. Battaglia, et al., *MNRAS*, 364 (2005) 433; Erratum: *MNRAS*, 370 (2006) 1055.
- [180] W. R. Brown, M. J. Geller, S. J. Kenyon and A. Diaferio, *AJ*, 139 (2010) 59.
- [181] A. J. Deason, et al., *MNRAS*, 425 (2012) 2840 [D12b].
- [182] V. Rashkov, et al., *ApJL*, 773 (2013) 32.
- [183] X. X. Xue, et al., *ApJ*, 738 (2011) 79.
- [184] X. X. Xue, et al., *ApJ*, (2012) accepted; arXiv:1211.0549.
- [185] W. E. Harris, (2010) arXiv:1012.3224; *AJ*, 112 (1996) 1487.

- [186] B. W. Carney, D. W. Latham, R. P. Stefanik, J. B. Laird and J. A. Morse, *AJ*, 125 (2003) 293; B. W. Carney, D. W. Latham, R. P. Stefanik and J. B. Laird, *AJ*, 135 (2008) 196.
- [187] L. Clewley, S. J. Warren, P. C. Hewett, J. E. Norris and N. W. Evans, *MNRAS*, 352 (2004) 285.
- [188] T. D. Kinman, C. Cacciari, A. Bragaglia, R. Smart and A. Spagna, *MNRAS*, 422 (2012) 2116.
- [189] A. W. McConnachie, *AJ*, 144 (2012) 4.
- [190] E. L. Lehmann and G. Casella, 1998, *Theory of point estimation* (Springer-Verlag, New York)
- [191] M. Evans, N. Hastings and B. Peacock, 1993, *Statistical distributions* (Wiley, New York).
- [192] R. L. Graham, D. E. Knuth and O. Patashnik, 1994, *Concrete mathematics: A foundation for computer science* (Addison-Wesley, Reading).
- [193] W. Dehnen, D. E. McLaughlin and J. Sachania, *MNRAS*, 369(2006) 1688.
- [194] P. R. Bevington and D. K. Robinson, D.K. 2003, *Data reduction and error analysis for the physical sciences*, 3rd Ed. (New York, NY: McGraw-Hill).
- [195] P. J. McMillan, *MNRAS*, 414 (2011) 2446.
- [196] P. J. McMillan and J. Binney, *MNRAS*, 402 (2010) 934.
- [197] M. Honma, et al., *PASJ*, 59 (2007) 839.
- [198] M. I. Wilkinson and N. W. Evans, *MNRAS*, 310 (1999) 645.
- [199] S. Samurović and A. Lalović, *A&A*, 531 (2011) A82.
- [200] L. L. Watkins, N. W. Evans and J. H. An, *MNRAS*, 406 (2010) 264.

- [201] R. Catena and P. Ullio, *JCAP*, 08 (2010) 004.
- [202] W. Dehnen and J. Binney, *MNRAS*, 294 (1998) 429.
- [203] P. Colin, A. A. Klypin and A. V. Kravtsov *ApJ*, 539 (2000) 561.
- [204] T. Fukushige and J. Makino, *ApJ*, 557 (2001) 533.
- [205] R. Wojtak, E. L. Lokas, S. Gottlober and G. A. Mamon, *MNRAS*, 361 (2005) L1.
- [206] G. A. Mamon and E. L. Lokas, *MNRAS*, 363 (2005) 705.
- [207] A. J. Cuesta, F. Prada, A. Klypin and M. Moles, 2007, submitted to *MNRAS*; arXiv:0710.5520.
- [208] N. Bozorgnia, R. Catena and T. Schwetz, *JCAP*, 12 (2013) 050.
- [209] S. H. Hansen and B. Moore, *New Astron.* 11 (2006) 333; arXiv:astro-ph/0411473.
- [210] R. Wojtak, E. L. Lokas, G. A. Mamon, S. Gottloeber, A. Klypin and Y. Hoffman, *Mon. Not. Roy. Astron. Soc.* 388 (2008) 815; arXiv:0802.0429.
- [211] A. D. Ludlow, J. F. Navarro, M. Boylan-Kolchin, V. Springel, A. Jenkins, C. S. Frenk and S. D. M. White, *Mon. Not. Roy. Astron. Soc.* 415 (2011) 3895; arXiv:1102.0002.
- [212] D. Lemze, et al., *Astrophys. J.* 752 (2012) 141; arXiv:1106.6048.
- [213] M. Sparre and S. H. Hansen, *JCAP*, 1210 (2012) 049; arXiv:1210.2392.
- [214] R. Wojtak, S. Gottloeber and A. Klypin, arXiv:1303.2056.
- [215] D. R. Hunter, *JCAP*, 02 (2014) 023.
- [216] P. Cuddeford, *MNRAS*, 253 (1991) 414.

- [217] O. E. Gerhard, *MNRAS*, 250 (1991) 812.
- [218] M. Baes and H. Dejonghe, *Astron. Astrophys.* 393(2002) 485; arXiv: astro-ph/0207233.
- [219] E. Van Hese, M. Baes and H. Dejonghe, *Astrophys.J.* 726 (2011) 80; arXiv:1010.4301.
- [220] A. Zait, Y. Hoffman and I. Shlosman, arXiv:0711.3791.
- [221] M. Sparre and S. H. Hansen, *JCAP*, 1210 (2012) 049.
- [222] S. H. Hansen and R. Piffaretti, *Astronomy & Astrophysics*, 476 (2007) L37.
- [223] O. Host and S. H. Hansen, *JCAP*, 06 (2007) 016.
- [224] O. Host, et al., arXiv: 0808.2049.
- [225] O. Host, *Nuclear Physics B (Proc. Suppl.)* 194 (2009) 111.
- [226] L. P. Osipkov, *Soviet Astronomy Letters*, 5 (1979) 42.
- [227] D. Merritt, *AJ*, 90 (1985) 1027.
- [228] J. H. An and N. W. Evans, *AJ*, 131 (2006a) 782.
- [229] C. S. Kochanek, *ApJ*, 457 (1996) 228.
- [230] M. I. Wilkinson and N. W. Evans, *MNRAS*, 310 (1999) 645.
- [231] M. Baes and M. van Hese, *A&A*, 471 (2007) 419.
- [232] J. Caldwell and J. Ostriker, *Astrophys. J.* 251 (1981) 61.
- [233] K. Kuijken and G. Gilmore, *Astrophys. J.* L9 (1991) 367.
- [234] T. Naab and J. Ostriker, *MNRAS*, 366 (2006) 899
- [235] R. W. Michie, *Mon. Not. R. Astron. Soc.* 125 (1963) 127.

- [236] R. W. Michie and P. H. Bodenheimer, *MNRAS*, 126 (1963) 269.
- [237] K. Kuijken and G. Gilmore, *MNRAS* 239 (1989) 571; *ibid.* 239 (1989) 605; *ibid.* 239 (1989) 651;
- [238] S. H. Hansen, B. Moore, M. Zemp and J. Stadel, *JCAP*, 1 (2006) 14.
- [239] A. Faltenbacher and J. Diemand, *Mon. Not. Roy. Astron. Soc.* 369 (2006) 1698; arXiv:astro-ph/0602197.
- [240] M. Fairbairn and T. Schwetz, 2008, arXiv:0808.0704.
- [241] [Super-Kamiokande collaboration] T. Tanaka et al, *Astrophys. J.*, 742 (2011) 78; arXiv:1108.3384.
- [242] [IceCube Collaboration] M. G. Aartsen, et al., arXiv:1309.7007.
- [243] F. Halzen, D. Hooper, *New J. Phys.*11 (2009) 105019; arXiv:0910.4513.
- [244] [IceCube Collaboration] M. Aartsenet. al., *Phys. Rev. Lett.*, 110 (2013) 131302; arXiv:1212.4097.
- [245] [Baksan Collaboration] M. Boliev, S. Demidov, S. Mikheyev, and O. Suvorova, *JCAP*, 1309 (2013) 019; arXiv:1301.1138.
- [246] [ANTARES Collaboration] S. Adrian-Martinez et. al., *JCAP* 1311 (2013) 032; arXiv:1302.6516.
- [247] [Fermi-LAT Collaboration]A. A. Abdo et al., *Phys. Rev. Lett.* 102 (2009) 181101; arXiv:0905.0025.
- [248] [H.E.S.S. Collaboration] F. Aharonian, et al., *Phys. Rev. Lett.* 97 (2006) 221102, Erratum-*ibid.* 97 (2006) 249901; astro-ph/0610509.
- [249] [PAMELA Collaboration] O. Adriani, et al., *Nature* 458 (2009) 607; arXiv:0810.4995.

- [250] J. Chang, et al., *Nature*, 456 (2008) 362.
- [251] W. Press and D. Spergel, *Astrophys. J.*, 296 (1985) 679.
- [252] A. Gould., *Astrophys. J.*, 321 (1987) 560.
- [253] A. Gould. *Astrophys. J.*, 321 (1987) 571.
- [254] K. Choi, C. Rott and Y. Itow, *JCAP*, 05 (2014) 049; arXiv: 1312.0273.
- [255] A. Bottino, *Phys.Lett. B.*, 402 (1997) 113.
- [256] J. Gascon, Dans *Astroparticles and cosmology*, Frontier Group(Ed.) (2004)91; arXiv:astro-ph/0504241.
- [257] J.D. Lewin and R.F. Smith, *Astropart. Phys.*, 6 (1996) 87.
- [258] C. Savage, G. Gelmini, P. Gondolo and K. Freese, *JCAP*, 04 (2009) 010; arXiv:0808.3607.
- [259] K. Griest and D. Seckel, *Nuclear Physics B*, 283 (1987) 681.
- [260] K. Freese, J.A. Frieman and A. Gould, *Phys. Rev. D.*, 37 (1988) 3388.
- [261] S. M. Koushiappas and M. Kamionkowski, *Phys. Rev. Lett.*, 103 (2009) 121301; arXiv:0907.4778.
- [262] M. Honma and Y. Sofue, *PASJ*, 49 (1997) 453.
- [263] X.X. Xue et al., *Astrophys. J.*, 684 (2008) 1143.
- [264] J. Silk, K. Olive, and M. Srednicki, *Phys. Rev. Lett.* 55,257 (1985).
- [265] K. Freese, *Phys. Lett. B* 167 , 295 (1986).
- [266] L.M. Krauss, M. Srednicki, and F. Wilczek, *Phys. Rev. D*33, 2079 (1986)
- [267] T.K. Gaisser, G. Steigman and S. Tilav, *Phys. Rev. D.*, 34 (1986) 2206.

- [268] S. Ritz and D. Seckel, Nucl. Phys. B., 304 (1988) 877.
- [269] G. Jungman and M. kamionkaowski, Phys. Rev. D., 51 (1995) 328.
- [270] A. Bottino et al. , Astropart. Phys. 3 , 65 (1995).
- [271] V. Berezhinsky et al., Astropart. Phys. 5 , 333 (1996).
- [272] L. Bergstrom, J. Edsjo, and P. Gondolo, Phys. Rev. D 55, 1765 (1997).
- [273] L. Bergstrom, J. Edsjo, and P. Gondolo, Phys. Rev. D 58, 103519 (1998).
- [274] J.L. Feng, K.T. Matchev, and F. Wilczek, Phys. Rev. D 63, 045024 (2001).
- [275] V. Barger et al. , Phys. Rev. D 65 , 075022 (2002).
- [276] M. Cirelli, et al, Nucl. Phys. B.,727 (2005) 99; Erratum: ibid 790 (2008) 338.
- [277] J. Edsjö, WimpSim Neutrino Monte Carlo,
<http://www.physto.se/~edsjo/wimpsim/>.
- [278] K. Hikasa et al. (Particle Data Group), Phys. Rev. D 45 (1992) S1; 46 (1992) 5210(E).
- [279] Super-Kamiokande collaboration: Y. Ashie et al, Phys. Rev. D., 71 (2005) 112005.
- [280] [DAMA/LIBRA collaboration] R. Bernabei et al., Eur. Phys. J. C., 56 (2008) 333; arXiv:0804.2741; ibid, C 67 (2010) 39; arXiv:1002.1028.
- [281] G. Angloher et al., Astropart. Phys., 18 (2002) 43.
- [282] [CDMS collaboration] D.S. Akerib et al., Phys. Rev. Lett., 96 (2006) 011302; arXiv:astro-ph/0509259.
- [283] [CDMS collaboration] Z. Ahmed et al., Phys. Rev. Lett., 102 (2009) 011301; arXiv:0802.3530.

- [284] [XENON10 collaboration] J. Angle et al., Phys. Rev. D., 80 (2009) 115005; arXiv:0910.3698.
- [285] [Super-Kamiokande collaboration] T. Tanaka et al, Astrophys. J., 742 (2011) 78; arXiv:1108.3384.
- [286] GAIA : http://www.esa.int/Our_Activities/Space_Science/Gaia_overview